NOx Monitoring in Humid Exhaust Gas Using Non-Dispersive Infrared Spectroscopy

Stolberg-Rohr, Thomine Kirstine; Clausen, Sønnik; Glarborg, Peter; Skov Hansen, Rene

Publication date:
2015

Document Version
Publisher's PDF, also known as Version of record

NO_X Monitoring in Humid Exhaust Gas Using Non-Dispersive Infrared Spectroscopy

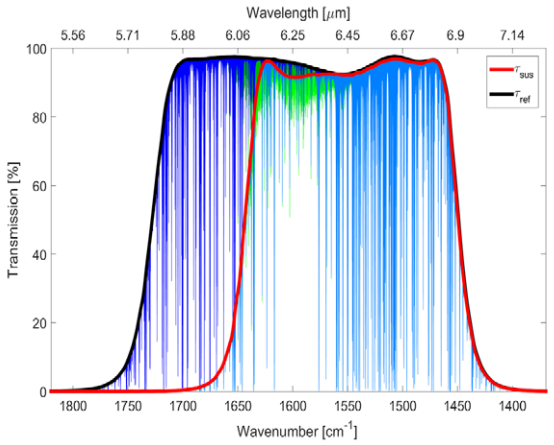

Thomine Stolberg-Rohr

PhD Thesis

August 2015

DTU Chemical Engineering
Department of Chemical and Biochemical Engineering

NO_X Monitoring in Humid Exhaust Gas Using Non-Dispersive Infrared Spectroscopy

PhD thesis

Thomine Stolberg-Rohr

Academic Supervisors:
Senior Scientist Sønnik Clausen, PhD
Professor, Peter Glarborg, PhD
DTU Chemical Engineering
Technical University of Denmark

Industrial Supervisor:
Senior Physicist René Skov Hansen, PhD
Danfoss IXA A/S

August, 2015

Abstract

This PhD thesis is concerned with the measurement of NO_X in moist exhaust gas onboard ships using non-dispersive infrared (NDIR) spectroscopy. In such a measurement one of the major challenges is spectral interference from water vapour which is present in high concentrations in the exhaust. The PhD study investigates a possible solution to this problem, which is to balance out the signal contribution from water vapour by means of carefully designed and manufactured optical bandpass filters. The thesis, presents a thorough theoretical description of the NDIR sensor concept together with simulations suggesting that it is possible but challenging to measure NO_X in moist exhaust gas using NDIR. The characteristics of optical filters tend to change with temperature, and since this compromises the water signal balancing, much of the work presented in the thesis is devoted to the design of optical bandpass filters in general, and temperature invariant filters in particular. This work has led to the derivation of the thermo-optical expansion coefficients of embedded PbTe and ZnSe thin films, frequently used in optical bandpass filters for the mid-infrared range. Knowledge of these coefficients allows accurate prediction of temperature invariant filters, previously realised based on experience and trial and error. Finally, the absorption spectrum of CO_2 at elevated temperatures and pressures has been experimentally investigated, and the absorption cross section of CO_2 at 1000 K and 100 bar is revealed for the first time. Information about CO_2 absorption and emission in combustion conditions is highly demanded for accurate modelling of heat transfer processes during combustion in large ship engines which in turn is crucial for understanding the formation of emission gasses, in particular NOx.

Resumé

Denne ph.d.-afhandling handler om at måle NO_X i fugtig udstødningsgas fra skibe ved brug af ikke-dispersiv infrarød (NDIR) spektroskopi. I en sådan type måling er en af de største udfordringer spektral interferens fra vanddamp som er til stede i høje koncentrationer i gassen. Ph.d.-studiet undersøger en mulig løsning på dette problem nemlig udbalancering af signalet fra vandamp ved hjælp af omhyggeligt designede og fremstillede optiske båndpasfiltre. I afhandlingen gives en grundig beskrivelse af teorien bag NDIR sensorkonceptet sammen med simuleringer der viser at NDIR spektroskopi er en mulig, men vanskelig teknik til måling af NO_X i fugtig udstødningsgas. En af vanskelighederne består i at de optiske filtres karakteristik ændres med temperaturen, og derfor er en stor del af arbejdet i denne afhandling viet til design af optiske filtre i almindelighed og temperaturinvariante filtre i særdeleshed. Dette arbejde har ført til udledningen af de termo-optiske udvidelseskoefficienter for indlejrede tyndfilm af PbTe og ZnSe i optiske filtre til brug i det midt-infrarøde område. Kendskab til disse koefficienter gør det muligt at forudsige og designe temperaturinvariante filtre hvilket tidligere var baseret på erfaring og trial and error. Endelig er absorptionsspektret af CO_2 blevet studeret ved høje tryk og temperaturer og absorptionstværsnittet af CO_2 ved 1000 K og 100 bar målt og præsenteret for første gang. Viden om absorption og emission fra CO_2 er stærkt efterspurgt i forbindelse med modellering af varmeoverførsel i forbrændingsprocesser i store skibsmotorer, hvilket er afgørende for forståelsen af dannelsen af emissionsgasser, i særdeleshed NOx.

Preface

This report finalises an industrial PhD project, carried out at Danfoss IXA and DTU Chemical Enngineering, which commenced on February 14th 2012. It was started up alongside a project supported by the Danish high technology foundation (HTF) aiming at developing an NDIR NO_X emission sensor for continuous on-board exhaust gas measurements on ships. One of several critical challenges in this development was the spectral discrimination between NO_X and water vapour and this is the topic of my PhD study.

However, in May 2013 Danfoss IXA decided for a major technology change and withdrew from the HTF project and stopped all development and activities on the NDIR sensor. This unfortunately implied that my results on in-optics humidity compensation were never experimentally verified, but the results from the original PhD project was summarised and published in the Proceedings of Advanced Photonics 2014.

At the time Danfoss IXA decided to withdraw from the HTF project, I was in England visiting the Infrared Multilayer Laboratory (IML) at the University of Reading who had agreed to manufacture the very precise optical filters that I was requiring in order to succeed in discriminating NO_X from water vapour. From my discussions with Head of IML Gary Hawkins, there turned out to be a huge gap in the published knowledge of the temperature dependence of thin film optical filters, and at the same time demands for temperature-stable infrared optical filters were emerging from progress in non-cooled infrared detector technologies. IML was in possession of a comprehensive repository of historical bandpass filters which had the potential of delivering the statistical grounds for extraction of thermo-optical properties of bandpass filters, and prediction of their temperature behaviour. This became the beginning of a very fruitful research collaboration which resulted in several discoveries reported in two major publications published in Optics Express.

Upon Danfoss IXA's exit from the HTF project, my PhD study was redirected toward CO_2 and H_2O measurements in exhaust gas recirculation applications at elevated pressures. At DTU Chemical Engineering, Optical Diagnostic Group, Postdoc Caspar Christiansen had designed and build a gas cell aimed at high temperature and high pressure CO_2 and H_2O measurements. He had just undertaken a validation process of the finalised gas cell as the project finished. I took over the experimental verification process in return for access to the cell, which added experimental work to the PhD project. The work with the cell resulted in a paper that has been submitted to Journal of Quantitative Spectroscopy and Radiative Transfer.

The PhD project has been supervised by the university supervisors Senior Researcher Sønnik Clausen and co-supervisor Professor Peter Glarborg. At the beginning of the PhD project the company supervisors were CTO Jens Møller Jensen and co-supervisor Product Development Manager Rainer Buchner. After they both left the company during the first half of the PhD study, Senior Physicist René Skov Hansen took over the supervising role.

Thomine Stolberg-Rohr
Vejle, August, 2015.

Acknowledgement

First of all, I would like to thank my former manager Rainer Buchner and the founder of Danfoss IXA Jens Møller Jensen; without the two of which, this PhD thesis would never have been written. Thanks also to my present manager Allan Skouboe for always being respectful about my PhD obligations, even in busy times, and to my company PhD supervisor René Skov Hansen, who seems to know everything and everybody, for always being on my side. To my colleagues at Danfoss IXA; thanks for your never failing helpfulness and interest in my project. I am looking forward become a full member of the sensor development team.

I would like to thank my university supervisors Sønnik Clausen and Peter Glarborg for guiding me through this PhD project, and I would further like to send my regards and thanks to Caspar Christiansen, with whom I spend some intense days and nights in the gas cell laboratory at DTU Risø, as well as to Alexander Fateev and Karsten Lindorff Nielsen, all members of the optical Diagnostic groups at DTU Chemical Engineering. I would like to acknowledge the company of my fellow PhD student in the Optical Diagnostics Group, Helge Grosch who was always three months ahead of me, and with whom I have spend many long and interesting days at Lund University studying optics and combustion diagnostics.

I would like to express my gratitude to Gary Hawkins, for an intense and productive period at Reading University, for letting me move into his office and for asking me to stay. Thanks also to Richard Sherwood and Karim Djotni for making me feel very welcome. I have come across a number of other inspiring people on my way, amongst them the chess-mathematician Guy Haworth.

Thanks to my friend and former chess-club magazine co-editor Martin Reib Petersen, for kindly answering questions about the English language, as well as to my long term friend Peter Bæk.

Finally, a very special thanks goes to my partner Anders for being available with support and technical discussions, and for making sure that I will have a pleasant memory of the last very busy days of this PhD project.

The PhD study was financially supported by Danfoss IXA A/S as well as The Danish Agency for Science, Technology and Innovation (DASTI).

Contents

Thesis Outline

The main topic of the present PhD study is the discrimination between emission gases and water vapour in non-dispersive infrared (NDIR) spectroscopic measurements in hot and moist exhaust gas on-board ships with particular focus on nitric oxides (NO_X). The PhD project resulted in one published conference paper, two published journal article, and one submitted journal paper. The content of each paper is summarised *Publication Summaries*. This thesis accounts for the background for the papers and their connection within the PhD project.

The purpose of the introduction given in Chapter 1 is to give the grounds for the global interest in exhaust gas emission monitoring from ships, introduce the main challenges involved in this, and discuss the present state of on-board NO_X sensing in hot and moist exhaust gas. Having established the rationale for continued research in improvements in exhaust gas emission monitoring, NDIR is introduced as a measurement principle for exhaust gas measurements as well as it main drawback; the interference with water vapour.

Chapter 2 presents the theoretical physical foundation for infrared gas spectroscopy; the interaction between light and molecules. It gives an insight into the comprehensive work that has been carried out over several decades to establish publicly accessible quantitative infrared databases, enabling quantitative spectroscopic calculations. The chapter concludes with the introduction of Beer-Lamberts law which together with the databases provide the basis of all simulations in the filter optimisations described in Chapter 3 aiming at overcoming the water interference hurdle.

Chapter 3 presents the concept of balancing out the water vapour signal by carefully designed optical filters to an extend where the remaining water vapour signal can be corrected by a simultaneous H_2O measurement. Results on filters designed for NO_2 measurements were presented orally at Advanced Photonics Congress 2014 and published in the conference proceedings (Appendix A). This chapter provides supporting details of the filter optimisation procedure and elaborates on results and conclusions.

Chapter 4 is devoted to optical filters seen from the perspective of a spectroscopist. The optical filters are an essential part of the in-optics humidity compensation. The chapter includes the results of a systematic study of temperature-invariant optical filters that I carried out in close coopperation with Gary Hawkins at Infrared Mulitilayer Laboratory at the University of Reading. This work resulted in two journal papers (Appendix B & C) while a third publication is in preparation.

Chapter 5 covers experimental measurements of CO_2 absorption at high pressures and temperatures. This work has been submitted to Journal of Quantitative Spectroscopy and Radiative Transfer and the paper in its submitted form is found in Appendix D.

Publication Summaries

Paper 1: In Optics Humidity Compensation in NDIR Exhaust Gas Measurements of NO_2

Status	Published [1]
Type	Conference Paper
Authors	Thomine Stolberg-Rohr, Rainer Buchner, Sønnik Clausen, Jens Møller Jensen, Allan Skouboe, Gary Hawkins & René Skov Hansen
Conference	Advanced Photonics OSA 2014

This paper presents the concept of balancing out the humidity signal in NDIR measurements of NO_2 in moist exhaust gas by using carefully designed and manufactured optical filters, the major challenge of which, lies in the wavelength tolerances in the filter production. The paper presents a set of fabricated filters for NO_2 measurement, together with the results of a theoretical evaluation of its performance. A cross sensitivity to water vapour of 3.2 ppm NO_2 for a change of 1000 ppm H_2O is predicted. The full conference paper is found in Appendix A.

Paper 2: Spectral design of temperature-invariant narrow bandpass filters for the mid-infrared

Status	Published [2]
Type	Journal Paper
Authors	Thomine Stolberg-Rohr & Gary Hawkins
Journal	Optics Express 2015

The advances in cooling-free detectors for mid-infrared sensing drives the development of optical filters that performs without the need for thermo-stabilisation. Temperature affects bandpass filters because the material properties of the thin film coatings constituting the filter, are subject to thermal expansion and temperature-induced changes in refractive index. For the vast majority of thin film materials both of these material properties changes positively with temperature, and hence the bandpass profiles are normally shifting towards longer wavelengths with increasing temperature. An exception from this rule is PbTe which

exhibits a negative change in refractive index with increasing temperature; an unusual behaviour which has been utilised to manufacture temperature invariant bandpass filters in the past. However no systematic study of the multilayer design dependence of the temperature-invariant property had previously been reported. The temperature dependence of a bandpass profile can easily be calculated, provided that the optical properties are known. However, when it comes to thin films, there is very little information available about temperature variations of the optical properties, and it becomes particularly scarce for the mid-infrared region above room temperature. The material properties of thin films are known to deviate from the properties of the material in bulk form, and the paper begins with presenting the results of a literature survey for published data on the thermal optical properties of thin film PbTe and ZnSe. The gathered thermo-optical material data for PbTe and ZnSe is shown to be insufficient to predict the temperature behaviour of real PbTe/ZnSe band pass filters. The paper present a systematic study based on a historic repositiory of bandpass filters made of PbTe and ZnSe, and primarily manufactured for space-flight missions. All filters were characterised in the range 0-200 °C and from this it was possible to relate temperature invariance to multilayer design and establish a formula to accurately predict the centre wavelength displacement of a bandpass profile with temperature for PbTe/ZnSe filters. This result was exploited to produce a number of temperature invariant bandpass filters with different centre wavelengths. The paper was well received and was selected for *Spotlight on Optics* [3]. The full paper is available in Appendix B.

Paper 3: Determination of the embedded thermo-optical expansion coefficients of PbTe and ZnSe thin film infrared multilayers

Status	Published [4]
Type	Journal Paper
Authors	Gary Hawkins & Thomine Stolberg-Rohr
Journal	Optics Express **23**(12), 2015

This paper presents the first reported thermo-optical expansion coefficients of thin film dielectric coatings of PbTe and ZnSe embedded in multilayer structures. The paper takes its offspring in the large set of measurement data presented in Paper 2 where bandpass transmission profiles were measured as function of filter temperature. Paper 2 also presented an equation relating the temperature-induced centre wavelength shift of narrow bandpass filters to the multilayer design and the thermo-optical material properties of the embedded thin film materials. The present paper uses these findings to extract the thermo-optical expansion coefficients for embedded thin films of PbTe and ZnSe. At three different mid-infrared wavelengths, the study in Paper 2 provides sufficient data for the coefficients to be determined by multivariate linear regression. The extracted thermo-optical expansion coefficient for embedded thin film ZnSe is close to the bulk ZnSe value, while embedded layers of thin film PbTe deviate significantly from bulk values. The coefficient for PbTe lies in-between

bulk values and previously reported values measured on free standing single thin film PbTe. This paper further reports the first manufactured narrow bandpass filter containing lead sulphide (PbS). PbS is an alternative lead salt material that possesses negative thermo-optical properties and the possibility of replacing PbTe with PbS extends the number of potential temperature invariant bandpass filters that may be realised. The full paper is available in Appendix C.

Follow-up paper in preparation: Design of temperature-invariant narrow bandpass filters containing PbS multilayers (3-5 μm)

A further paper is being prepared on the design of temperature invariant PbS/ZnSe narrow bandpass filters. This paper follows the same methodology as was applied for PbTe/ZnSe filters in Paper 2 and Paper 3, and uses it to extract the thermo-optical expansion coefficient for embedded thin film PbS and predict which bandwiths that may be realised with PbS and ZnSe, exhibiting temperature invariant properties. The amount of available data is less extensive than for the PbTe/ZnSe study since PbS was only recently used in narrow bandpass filters for the first time, as reported on in Paper 3. However, a number of filters have been manufactured subsequently, and preliminary results indicate that the thermo-optical expansion coefficient of embedded thin film PbS, deviates significantly from bulk values. As it was the case for embedded thin film PbTe, bulk values of PbS cannot be used to predict temperature invariance of PbS/ZnSe narrow bandpass filters. To improve the data foundation for the extracted thermo-optical coefficient of embedded PbS thin films, the manufacture of a number of PbS/ZnSe with distinct multilayer structures are in the pipeline. This follow-up paper will contribute with another important step in the direction towards control of temperature invariance.

Paper 4: High Temperature and High Pressure Gas Cell for Quantitative Spectroscopic Measurements

Status	Submitted
Type	Journal Paper
Authors	Caspar Christiansen, Thomine Stolberg-Rohr, Alexander Fateev & Sønnik Clausen
Journal	Journal of Quantitative Spectroscopy and Radiative Transfer

In the efforts of reducing emissions and fuel consumption in large ship engines, better understanding of thermal transfer processes during combustion is required. Particular for large diesel ship engines, the thermal radiation of CO_2 is a major contributor to heat transfer in the engine, and it is therefore necessary to be able to accurately calculate the radiative emission from CO_2. However, at combustion temperature and pressure, the emission spectrum of CO_2 has never been measured. Although databases exist, and empirical pressure broadening models have been used to obtain good agreement with existing high temperature

and high pressure experimental data, these models have never been verified experimentally at combustion conditions which may reach as high as 2400 K at 200 bar. This paper reports on the construction of a ceramic cell, designed for measurements at pressures up to 200 bar at temperatures up to 1300 K. This is not sufficiently high temperatures for the large ship engines, but it exceeds previously reported measurements which have been limited to ~627 K because the gas cells used have been build of metal. However, for this first publication on the ceramic high temperature and high pressure gas cell, it has only been used at combined temperature and pressure up to 1000 K and 100 bar under which conditions, the first measured absorption cross section spectrum of CO_2 is presented. It is shown that use of the simple Voigt formalism in the calculation of the CO_2 spectrum, under these conditions overestimates the total emission from the strong band at 2300 cm^{-1} with 20 % while the weaker band at 3700 cm^{-1} shows good agreement in band emission between measurement and the Voigt-based simulation. The full paper is available in Appendix D.

CHAPTER 1

Introduction

1.1 Continuous Emission Monitoring

On-board monitoring of air pollutants in exhaust gas from ships is a rapidly growing business and research area. It is mainly driven by strong political demands to reduce the emission of nitric oxides (NO_X) and sulphur dioxide (SO_2), both of which are toxic to humans as well as the environment, and are considered responsible for lethal respiratory deceases as well as acidification of lakes and streams [5]. According to [6], the social cost related to human health impacts resulting from emissions from international ship traffic amounted to 58 bn €/year in the year 2000 corresponding to 7% of the total health costs in Europe, and it is expected to increase to 64 bn €/year in 2020 where the number of premature deaths per year in Europe due to international ship traffic emissions are estimated to exceed 53000. With similar figures in the rest of the world, there exists a global socio-economic interest to enforce regulations on ship emissions.

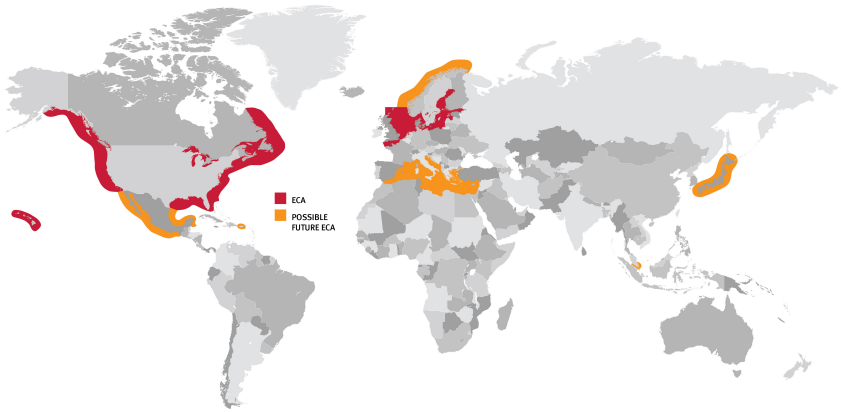

Figure 1.1: IMO Emission Control Areas [7].

In 1973 *The International Convention for the Prevention of Pollution from Ships* (MARPOL) was adopted by the International Maritime Organisation (IMO) and has been signed

by the worlds largest seafaring nations, representing 99 % of the worlds shipping tonnage [8]. It has been updated several times over the years and in 1997 it was extended to cover air pollution with the amendment of *Annex IV Prevention of Air Pollution from Ships* which heralded a number of regulations on the emissions of NO_X and SO_2, the first of which entered into force in 2005 [9]. The regulations are continuously tightened with the strictest requirements applying to the Emission Control Areas (ECA) indicated in Figure 1.1.

In 1997 there was no approved exhaust gas monitoring system but the gas emission systems for landbased powerplants were well established [10]. The adoption of Annex VI therefore intensified the development of emission sensors for marine exhaust gas as well as the development of after-treatment systems removing NO_X and SO_2 from the exhaust gas. In the endeavour to reduce NO_X and SO_2, the demand for Ammonia (NH_3) and carbon dioxide (CO_2) measurements has evolved. Since each compound is different in terms of abundance and sensitivity to fuel quality and engine parameters, they are treated independently in the following.

NO_X

NO_X is defined as the sum of all nitric oxides but in regulation contexts it usually refers to the sum of NO and NO_2 which are the major nitric oxide compounds in exhaust gas. NO_X is produced in diesel engines in concentrations that are highly depending on the combustion parameters. It is partly generated from the nitrogen content in the fuel, however, the major contribution to NO_X concentration in marine diesel exhaust is nitrogen in the intake air which is converted into NO_X at a rate depending on the combustion temperature. The NO_X concentration in the exhaust gas from petrol engines is small because the combustion temperature is low compared to diesel engines. There are two ways to reduce the NO_X production; the combustion temperature dependence of the NO_X production implies that NO_X production can be regulated by the the air/fuel ratio. This means that the reduction of NO_X requires a suboptimal air/fuel-ratio which implies that the engine efficiency is lowered and more CO_2 per kWh is let out. However, this is preferred over NO_X emission. Another option is to use after-treatment equipment to convert NO_X into N_2 and H_2O by selective catalytic reduction (SCR) [11].

As a rule of thumb NO_2 concentrations in exhaust gas are about ten times less than the NO concentration and therefore sometimes only NO is measured while NO_2 is estimated. However, this procedure is not sufficiently accurate to meet the requirements of MARPOL, and thus also NO_2 has to be measured independently.

SO_2

SO_2 is sometimes referred to as SO_X because as with NO_X it is the total emission of sulphur oxides that is of interest. However, SO_2 constitutes the vast majority of sulphur oxides emitted in diesel engine exhaust gas and is thus the compound subject to regulation, although 2-4% of the fuel sulphur content is emitted as SO_3 according to [12]. In contrast to NO_X, the SO_2 concentration is directly related to the sulphur content in the oil burned, implying that the SO_2 concentration in the exhaust gas can be calculated if the fuel composition is known. As for NO_X , SO_2 may be reduced in two ways; on the input side by using

low sulphur fuel, or by aftertreatment of the exhaust gas which can effectively be cleaned from SO_X by rinsing the exhaust gas with water which converts the SO_X into sulphuric acid.

NH_3

In order to reduce NO_X, catalytic after-treatment equipment is used to convert NO_X to nitrogen and water by supplying NH_3 usually in the form of a water solution of urea which is sprayed into the exhaust gas where it decomposes into NH_3. However, this entails the risk of emitting the corrosive and toxic NH_3 in the case of non-ideal catalytic reaction or excess supply of NH_3 in transient stages. This is highly undesired and has led to a request for ammonia exhaust gas sensors, although IMO has not yet set any limits for ammonia leakage from ships [13].

CO_2

CO_2 is a major compound when burning fossil fuels and probably the best known environmental concern. CO_2 measurements are also strongly demanded in exhaust gas measurements, although not for their environmental influence but as a continuous input for engine control as well as a tracker of the dilution of exhaust gas in SO_2 measurements where the ratio SO_2/CO_2 is required by authorities to prove that the sulphur content of the oil is below legal limits. Another application that demands fast CO_2 sensors is exhaust gas recirculation (EGR) which utilises that the production of NO_X can be reduced by decreasing the oxygen level in the intake air. In EGR this is achieved by mixing fresh air which has a constant oxygen content with exhaust gas which have a very low oxygen concentration and use this mixture as intake air [14]. Since CO_2 is more easily measured in marine exhaust gas compared to oxygen, fast CO_2 measurements are used to provide continuous feedback on the EGR ratio, i.e., relative amount of recirculated exhaust gas in the intake air [15]. For EGR applications the CO_2 sensor must operate at pressures up to 6 bar. CO_2 absorption at high pressures is the topic of Chapter 5.

Challenges in Marine Diesel Exhaust Gas Measurements

Exhaust gas from ship engines is hot, humid and chemically aggressive. The exhaust gas temperature may reach 500 °C for low and medium speed engines which are standard in shipping industry. In return the pressure requirements are relaxed as the pressure in the exhaust pipe is close to ambient, although for EGR applications, CO_2 measurements at pressures up to 6 bar are required. On-board marine exhaust gas measurements differ significantly from landbased power plant measurements in several aspects, including vibrations, fuel type, fuel supply homogeneity, load dynamics, available space, as well as shifting personnel. While a power plant usually acquire fuel from a single source, the fuel supply on a ship may vary significantly in composition as the fuel is provided by several different sources across continents. A power plant is run under very stationary conditions while a ship has many starts and stops and the acceleration phase is connected with increased production of harsh components which challenges the durability of an exhaust gas sensor. In addition the high sulphur fuel makes the exhaust gas more sticky and corrosive compared

to automotive exhaust gas [16, 17] inferring that the sensor must be significantly more resistant to the chemical environment or must be replaced rapidly. Space availability in the engine room of a ship is of tremendous concern for both after-treatment systems as well as emission monitoring equipment, particularly for the existing ships which are not designed to accommodate this sort of auxiliary apparatus. Landbased emission gas sensors are not subject to similar dimensional issues and are often very large. A further difference is that the environment on the ship is strongly vibrating; a sensor that is mounted on the exhaust pipe must be tested to withstand up to 4 g of vibration [18]. This is a serious problem for many optical systems that rely on optical alignment across the exhaust pipe.

Exhaust Gas Composition

When the fuel content varies, the exhaust gas composition varies accordingly. With the fuel mainly consisting of long hydrocarbon (HC) chains, the exhaust gas will contain approximately equal levels of the two major emission gases H_2O and CO_2 with their actual concentrations depending on the air-fuel ratio. The sulphur content in the fuel is converted into SO_X while the emission of NO_X, CO, and HC depends on engine parameters. Figure 1.2 shows typical marine diesel exhaust gas compositions from MAN two-stroke engines as of 2004 [19].

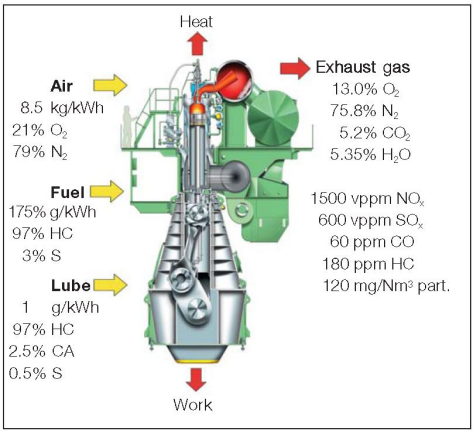

Figure 1.2: Typical exhaust gas composition from marine diesel engines based on typical fuel content, air-fuel ratio, and lubricant [19]. Note that minor constituents are not included.

Newer engines, however, have reduced NO_X emissions in order to comply with IMO regulations. In a project guide from 2013, MAN gives an H_2O exhaust gas concentration range of 5.9 to 8.6 % volume mixing ratio (VMR) while the NO_X concentration is stated to be in the range 700 to 1000 ppm [20].

For the purpose of the NO_X sensor development behind this PhD work, the NO_X concentration range was set to 0-1200 ppm and the upper water vapour content used to evaluate

cross sensitivity to humidity was considered to be 8 %VMR. To comply with the Marpol regulations, drift in the measurements must be below 2% of full scale [21], which for the chosen range equals 24 ppm. In this work the NO and NO_2 are measured independently which means that each of the measurements should be stable within 12 ppm. The cross sensitivity to water vapour should thus be well below this value.

State-of-The-Art in On-Board NO_X Emission Monitoring

Methods for NO_X detection in exhaust gas include chemiluminescence, electrochemical cells, Fourier transform infrared (FTIR) spectroscopy, and non-dispersive infrared (NDIR) spectroscopy [22], while ultraviolet (UV) spectroscopy has recently been added [23]. However, for marine exhaust gas applications all of these have serious drawbacks. The chemiluminescent and electrochemical cell methods are troubled by the requirement of physical contact between the sensing element and the harsh exhaust gas. For this reason existing marine exhaust gas sensors extract and condition the gas and this includes drying and cooling before measurement. This is not desirable since it adds uncertainties to the measurement as the exhaust gas undergoes chemical transitions in the conditioning process. Further, it implies additional equipment and maintainance. Nonetheless, extractive dry-based chemiluminescence is currently the preferred technique for NO_X measurements in marine exhaust gas in compliance with the Marpol convention [21]. In automotive exhaust gas sensing, inexpensive in-situ electrochemical Zirconium sensors have become standard equipment but the adaptation to marine exhaust gas is troubled by premature ageing of the sensor in the harsh exhaust gas [24, 25].

Optical methods have a great advantage in harsh environments since the sensing element does not require physical contact with the target gas. However, optical methods are usually extremely sensitive to alignment and FTIR spectroscopy further relies on moving mirrors which suffer under strong vibrations. NDIR spectroscopy is robust toward vibrations compared to other optical sensors owing to its very simple construction. In return, NDIR has poor spectral resolution which makes water interference a major problem in moist exhaust gas measurements of NO_X, SO_2 and NH_3. UV spectroscopy is an interesting alternative but faces strong absorption and scattering by soot and particles, as well as short lifetimes of UV sources [26].

1.2 NDIR Exhaust Gas Measurements

This PhD study aims at solving the water interference impediment for the use of NDIR spectroscopy in on-board exhaust gas measurements of NO_X, SO_2, and NH_3. NDIR is a simple optical measurement technique that has been used extensively for gas sensing over many years [27]. In contrast to chemical sensors, NDIR shares the important advantage with other optical methods of being non-intrusive, i.e., the sensing element does not require physical contact with the chemically aggressive, hot and humid exhaust gas.

The name non-dispersive refers to the omission of a dispersive element in the sensor such as a grating or a prism used in other spectroscopic devices. Instead, the wavelength selection is provided by one or more optical filters. A simple NDIR setup is sketched in

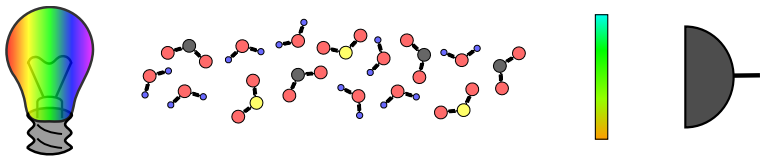

Figure 1.3: Basic NDIR setup. The basic components of an NDIR sensor are a broadband IR source, an optical bandpass filter, and an IR detector.

Figure 1.3. The basic elements of an NDIR sensor are a broadband IR source, an optical filter, and an IR detector. The IR source emits infrared radiation which travels trough the measurement gas in which the molecules absorb radiation of specific wavelengths. Before reaching the detector where the infrared light is converted to an electric signal, the radiation passes through an optical filter selecting a wavelength range covering absorption lines of the gas that is to be measured. The electrical signal then reflects the concentration of the target gas species.

NDIR sensors come in a number of variations. Usually, a reference measurement is required to compensate for drifts, e.g. in source intensity, which might be achieved by a reference measurement chamber filled with an infrared neutral gas or by an optical filter which selects a wavelength region without gas absorption. The main reason for using optical filters for the wavelength selection is that the mid-infrared region suffers from noisy detectors and low-efficiency emitters [28] which imply that the signal to noise ratio does not allow the intensity to be divided over an array of detectors as is common in the visible range were silicon CCDs offer highly sensitive and inexpensive detector arrays. In return, the strong absorption lines in the mid-IR region allow short active pathlengths. In contrast, in the working range of the silicon CCDs, the gas absorption strengths are orders of magnitudes lower which means that gas sensors in this range usually rely on multiple reflections to reach pathlengths of several meters, which is hardly compatible with measurements in harsh exhaust. In the highly vibrating environment NDIR distinguishes itself from other optical methods because alignment sensitivity is mitigated by the omission of lasers, multiple reflections, and moving parts. The simple design of NDIR further makes it an inexpensive alternative to other optical gas sensing systems. The drawbacks, on the other hand, are the weak signal to noise ratio and poor discrimination between gases with closely separated or overlapping absorption lines. In hot exhaust gas measurement, NDIR further faces substantial amounts of background radiation emitted from all hot surfaces as well as from the gas itself.

Water Vapour Interference

While NDIR is commonly applied in exhaust gas emission sensing of CO_2 and CO, the NDIR measurement of NO, NO_2 , SO_2 and NH_3 are all troubled by water interference. In particular, for NDIR NO_X measurements in moist exhaust gas, the difficulty in separating

the desired emission gases from water vapour because of overlapping absorption lines means that NDIR is presently limited to dry gas measurements of NO_X [29].

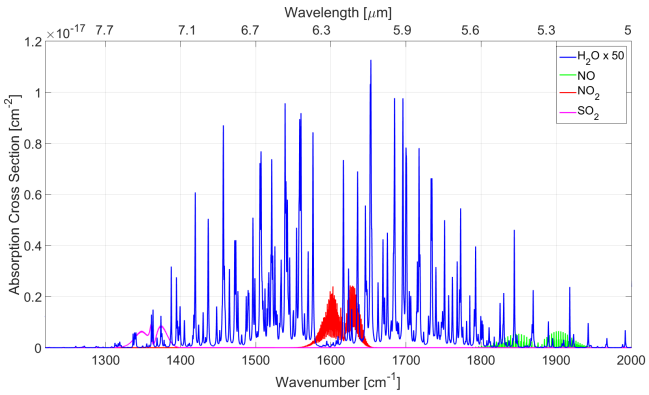

Figure 1.4: Absorption cross sections of NO, NO_2 and H_2O. The cross section of water vapour has been scaled by a factor of 50 to account for the higher water concentration in the exhaust gas.

Figure 1.4 shows the absorption cross sections of NO, NO_2 and SO_2 together with H_2O which for visualisation purposes has been multiplied by a factor of 50 to indicate the large presence of water vapour, which typically constitutes 5% VMR of the exhaust gas (= 50000 ppm). In comparison, the NO, NO_2, and SO_2 concentrations are usually below 1000 ppm.

State-of-the-art of Water Discrimination in NDIR Spectroscopy

The approach of distinguishing NO from water vapour by careful optical filter design has been undertaken previously in [30] where two NO lines with minimum H_2O interference were selected using a very narrow optical filter. The obvious drawback of this approach which is also stated in the paper, is that two NO lines gives a very low signal compared to the typical broadband filters used in NDIR, considering that the NO band (around 1900 cm^{-1}) contains several hundreds of major absorption lines. Another interesting approach to compensate for interferences is the concept of negative gas filtering [31] where a gas tight cell containing the target gas is inserted in front of a reference channel, which is a way to effectively select the wavelengths at which the target gas absorbs. While this is theoretically elegant, it is not a simple mechanical task to construct a small gas tight and transparent cell and positioning it in front of a reference channel. Furthermore, the concept does not apply well to measurements in hot gas because for the absorption spectra of the gas filter cell and exhaust gas to match, equal pressure and temperature is required, and this can be very difficult to obtain under all possible circumstances. If the absorption spectra do not match it will lead to a complex dependence on the interfering H_2O with varying temperature and pressure. Thus, both from a mechanical and signal processing perspective, it would be preferable to avoid a gas filter cell.

In a predominantly theoretical study from 2011 [32] the authors claims to have eliminated the interfering effect of water vapour in an NDIR multigas measurement of CO, NO, NO_2 CO_2, SO_2, and H_2O, using a filter wheel with seven bandpass filters together with linear regression. The paper leaves some open questions about the amount of water vapour that has been used in their verifications measurements. Half a year later, the same authors report experimental results with simultaneous NDIR measurements of CO_2 CO and NO in a similar setup but in this paper only cross-sensitivities between the three target gases are corrected while H_2O is not mentioned [33].

CHAPTER 2

Quantitative Infrared Absorption Spectroscopy

The work in this PhD study stands on the shoulders of decades of computational and experimental efforts to construct spectral databases containing fundamental infrared absorption lines for various common gas molecules. Without the quantitative spectroscopic knowledge available through the databases, the ambitious optical filter setup optimisation in Section 3.3 would not be meaningful. With these databases at hand, spectroscopic simulations can be undertaken without particular knowledge about molecular absorption principles. However, some appreciation of the underlying physical phenomena is appropriate, as well as an understanding of the extensive work required to improve and expand the databases. This chapter provides a short description of the physical principle behind the infrared absorption spectrum, as well as a brief outline of the complex quantitative quantum mechanical calculations involved in the database development.

2.1 Physical Principle of Molecular Absorption

Molecules are able to absorb electromagnetic radiation and convert it into molecular rotation, molecular vibrations, electronic transitions or a superposition hereof. Only radiation with photon energy that matches possible energy transitions of the molecules are absorbed. The energy states of a molecule are unique to that molecule and therefore the transition spectrum can be used to determine which molecules are present in a volume of gas. The atoms in a molecule are being held together by attractive forces. However, if the atoms come too close to each other they become subject to strong repulsive forces. These counteracting forces constitute a potential energy distribution in the molecule wich reaches a minimum value at a certain inter-atomic separation. Figure 2.1 shows an energy diagram for a diatomic molecule where the potential energy is shown as a function of the distance between the two atoms constituting the molecule, the lower curve representing the electronic ground state and the upper curve the first excited electronic state. In each electronic state there is a certain inter nuclei distance which minimises the potential energy and the molecule is vibrating around this optimum. Heisenberg's uncertainty principle prevents the molecule from resting at the optimum. There exist a number of different ways for a molecule to vibrate, which are referred to as vibrational states, each of which requires a certain vibrational or kinetic

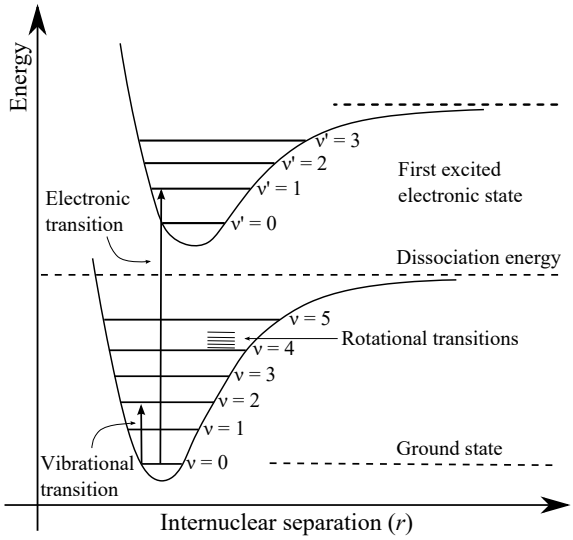

Figure 2.1: Energy diagram showing potential energy curves versus internuclear separation for a diatomic molecule.

energy. The vibrational energy states are indicated in Figure 2.1 along with arows indicating that the molecule can make transitions between different vibrational energy states by absorption of a photon with a photon energy corresponding to the energy difference. Absorption of infrared radiation is associated with transitions between vibrational energy states. However, these transitions normally involve simultaneous transitions between rotational states, which leads to fine-structured absorption spectra.

2.2 Spectral Databases

Calculation of the energy states in a molecule is computationally heavy. First the potential energy function must be calculated which is already complicated for a diatomic molecule with drastic increase in complexity for larger molecules [34]. When the potential function is established, it is used as input to the time independent Schrödinger equation;

$$E\Psi(\mathbf{r}) = \left[\frac{-\hbar^2}{2\mu}\nabla^2 + V(r)\right]\Psi(\mathbf{r}) \tag{2.1}$$

where $V(r)$ is the potential energy as a function of the inter-nuclei separation, and the operator $\frac{-\hbar^2}{2\mu}\nabla^2$ represents the kinetic energy of the molecule. For more complex molecules than the diatomic case, the potential energy curve is three dimensional. The solution to the Schrödinger equation gives the energy levels (E) of the molecule as well as the three dimensional wavefunctions ($\Psi(\mathbf{r})$), which describe the probability of finding the atoms of the molecule in a given distance from each other. The transition probability between the energy

states is proportional to the overlap of the corresponding wavefunctions which determine how likely the molecule is to absorb a photon with a matching photon energy. This parameter is called the integrated line intensity and is stored in the spectroscopic databases together with line broadening information. The absorption lines are broadened by three mechanisms; natural broadening which is a consequence of Heisenbergs uncertainty preventing the energy level of a molecule to be precisely determined, Doppler broadening which is caused by thermal motion of the atoms, and pressure broadening induced by colliding molecules. However, the calculation of line intensities requires empirical input, which is used to adjust the potential energy curves of the molecule to obtain correspondence between the calculated transition spectrum and experimental data.

2.3 The Measured Absorption Spectrum

Getting from the databases to the absorption spectrum requires the calculation of the absorption cross section (σ_λ) which determines the probability of light absorption as a function of wavelength (λ) for a given concentration, temperature, and pressure. Calculation of σ_λ from the line intensities and broadening information provided by the databases is relatively straightforward but computationally very heavy and often forces certain simplifications to be made which may lead to inaccuracies in the resulting calculated absorption spectrum. There exist commercial and non-commercial software that offers the calculations of absorption cross sections. In this PhD-study I have relied on SpectralCalc.com [35] to provide me with absorption cross sections for the spectral simulations presented in Chapter 3.

When the absorption cross section is determined the transmission (τ) through a gas can easily be calculated by Beer-Lambert's law;

$$\tau(\lambda) = \exp(-\sigma_\lambda N L) \tag{2.2}$$

where L is the optical pathlength, i.e. the length of the path that the light travels through the gas, and N is the number concentration of the gas.

CHAPTER 3

In-Optics Humidity Compensation

Spectral interference between emission gases and water vapour in NDIR exhaust gas measurements is the general focus of the present PhD study and the topic of this chapter. The spectral separation in NDIR relies on optical filters. However, these have certain fabrication tolerances which challenge the desired discriminating abilities. This chapter presents the attempt to find an optical filter setup which enables NDIR NO_X measurements in moist exhaust gas.

The chapter begins by introducing the NDIR measurement setup, and discusses each part of the optical system with emphasis on spectral dependencies (Section 3.1). The concept of in-optics humidity compensation is then described mathematically in Section 3.2. The procedure undertaken for determining the best filter setup is explained in Section 3.3. A set of manufactured filters for NO_2 measurements is presented and evaluated in Section 3.4, while the learnings from the development process are summarised and the next generation filter optimisation procedure laid out by the end of the chapter.

3.1 Sensor System

Choosing the best optical filter setup is dependent on the total optical system since each component have spectral characteristics that affect the relative response to the absorbing gases. Every part of the optical system should therefore be spectrally characterised an incorporated in the filter optimisation procedure. However, since the development of the overall sensor system took place concurrently with the filter optimisation, this could not be fully accomplished, and the simulations had to be based on expectations.

The simultaneous development of two interdependent parts of the sensor entailed the risk that the filter optimisation would need to be repeated at a later stage, but in return, it provided the possibility to deliver feedback to the system development along with the growing appreciation of the critical and less critical factors within optical bandpass filters. As an example, one open question in the beginning of the project was whether the tight precision requirements to the optical filters would counter-demand a narrow incident angle.

The NDIR sensor system that forms the basis for the spectroscopic simulations in this chapter, is sketched in Figure 3.1, and in the following the basic components of the system are discussed with focus on their influence on and interaction with the optical filter optimisation.

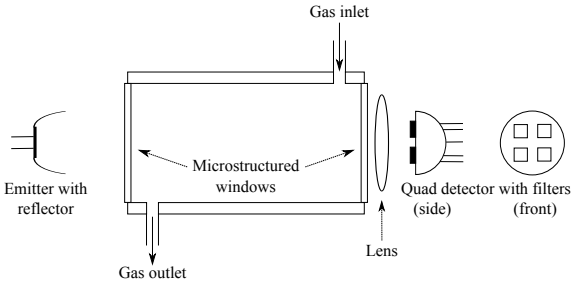

Figure 3.1: NDIR sensor setup comprising an infrared source, a measurement chamber, and an infrared detector. The source and detector are seperated from the harsh exhaust gas by microstructured optical windows, and a lens is collecting the radiation from the emitter. The detector is a quad channel thermopile detector with an individual optical filter attached upon each channel.

Measurement Chamber

The measurement chamber contains the hot exhaust gas which is continuously flowing through. Prior to entering the measurement chamber, the exhaust gas has been mechanically filtered to remove large particles. However, no additional gas conditioning takes place. The exhaust gas is between 200 °C and 500 °C and contains 4 % to 8 % volume mixing ratio (VMR) of water vapour, while the pressure is close to atmospheric pressure. The length of the measurement chamber is important as it influences the filter optimum because a long pathlength infers that strong absorption lines are saturated, increasing the impact of weaker absorption lines. A long pathlength is prefered to increase the absorption signal and thereby reduce various cross sensitivities to other optical variations, e.g. changes in the source temperature. However, within the framework of the HTF project, the longest dimension of the sensor was not to exceed 40 cm. Since this included room for emitter and detector as well as thermal decoupling between these and the measurement chamber, the spectroscopic simulations in this chapter are based on a pathlength of 25 cm. Although the gas is mechanically filtered sub-micron particles are still present and soot is expected to build up on surfaces including the windows that are providing optical access to the exhaust gas.

Soot

Soot is a mass of fine carbon particles that are produced in incomplete combustion of hydrocarbons. A thin soot layer is opaque to visible light but mid-infrared radiation is able to penetrate, which is one of the great advantages in infrared exhaust gas measurements. Figure 3.2 shows the result of a transmission measurement that I made on two ZnSe windows that had been placed inside a burner in relation to an otherwise unrelated project. One of the windows were completely black as shown in the inset and the soot layer would have killed any spectroscopic measurement in the visible region. However, in the range of interest for

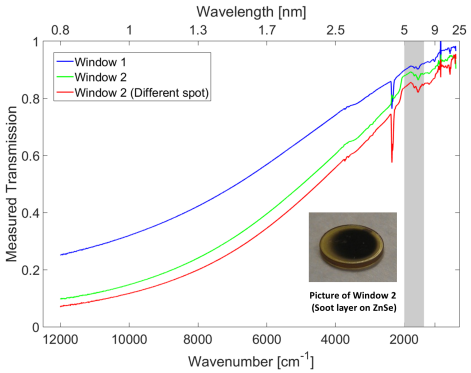

Figure 3.2: Measured transmission of soot layers on ZnSe substrates originating from a burner test in an otherwise unrelated project. The measurements were done in an ambient environment and therefore CO_2 and H_2O signatures are seen in the spectrum at long wavelengths. The transmission increases drastically with increasing wavelength. The windows were kindly made available by Sønnik Clausen, DTU Chemical Engineering, Optical Diagnostics group.

the mid-infrared NO_X measurements, which is indicated by a grey rectangle, the soot layer transmits about 85 % of the light. The noise at long wavelengths are caused by ambient H_2O and CO_2 present during the measurement, and thus the measurements do not provide information about possible narrow spectral features.

In [37], a study of pure carbon soot reported no features between 3.4 μm and 7.9 μm. However, soot is not just soot and in [38], the combustion of heavy fuel oil were found to result in soot aggregates containing alkali earth metals (V, Ni, Ca, Fe), and another study on diesel exhaust soot reported characteristic peaks in the 5-7 μm range [36] (Figure 3.3).

The indication of narrow spectral features in the soot aggregate means that soot might be a serious issue for the NDIR NO_X sensor and that soot on the optical windows should be minimized.

Self-Cleaning Windows

Acknowledging that soot formation on the optical windows is a critical concern in the development of the NDIR exhaust gas NO_X sensor, this subject was an independent and major part of the HTF project. DTU Nanotech was given the task to develop micro-structured optical windows with self-cleaning properties in exhaust gas from ships at temperatures up to 500 °C. Since this work was still in an early phase when the spectral simulations in this chapter were conducted, and the final transmission of the windows were completely unknown, they were not included. However, later in the project DTU Nanotech was able to present a breakthrough [39] and provide me with spectral measurements of promising window candidates, which were included in numerical evaluation of the manufactured NO_2 filters presented in Section 3.4.

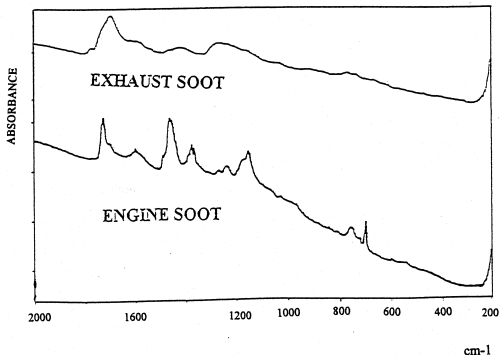

Figure 3.3: Soot spectrum in diesel exhaust and in a diesel engine showing narrow spectral features. Reprinted from [36].

Infrared Source

Modulation of the source intensity is crucial in NDIR spectroscopy at elevated temperatures in order to eliminate background radiation from hot surfaces as well as from the gas itself as explained mathematically in Section 3.2.

Since any moving parts are strongly undesired in the vibrating environment, electronically modulatable infrared emitters are required. A variety of fast electronically controlled emitters are commercially available. All of them provides significantly less intensity compared to a high temperature solid emitter, which cannot be electronically modulated at a sufficient rate. The lower intensity is to some extent compensated by the ability to produce near sinusoidal intensity curves, which makes noise reduction in the signal processing more efficient.

However, it is not straightforward to choose which commercial emitter to employ, even though the emitted power is easily calculated from the surface temperature, area, and emissivity. Mostly, the accompanying datasheets specify all of these important values but omit information about the wavelength dependence of the emissivity. For this reason I carried out a series of experimental spectral characterisations of six different commercial electronically modulatable emitters, the result of which is given in Figure 3.4 where the apparent emissivity is shown as a function of wavenumber for each of the six emitters. It was not possible to determine the precise emissivity value since the temperature of the tiny, fragile emitting surfaces could not be accurately measured and assumptions of a maximum emissivity of 0.95 were used to obtain the apparent emissivities for four of the emitters, while for two emitters that had low emissivities, partwise gray-body assumptions were used. Note that a low emissivity does not necessarily mean that the intensity is low since this depends on surface temperature and area as well. However, the apparent emissivities in Figure 3.4 demonstrate significant spectral dependencies and differences between the various emitters. Over the range of interest for the NDIR NO_X sensor only one emitter exhibits a flat high emissiv-

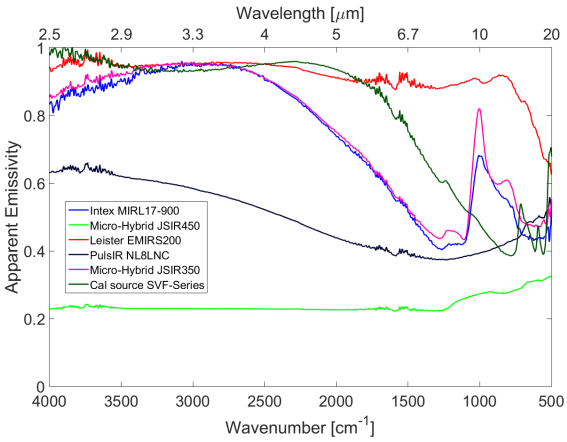

Figure 3.4: Apparent emissivity measured for a number of commercially available emitter samples.

ity. This emitter, the Leister EMIRS200, was therefore selected for the first prototype and assumed in the filter setup simulations.

Infrared Detector

Infrared detectors for the wavelength range 4-7 μm operating at room temperature and above are very limited in numbers compared to shorter wavelength detectors. However, there has been rapid progress in the field within the later years [40] also for non-cooled operation, and a recently reported non-cooled InSb detector, sensitive in the range 2-7 μm [41] is likely to be employed in future NDIR sensors. For the present sensor development a thermopile detector was selected because of its robustness, reliability, and good cost/performance ratio, and not least because of its flat sensitivity over the wavelength range, in contrast to the highly wavelength sensitive photodetectors. The thermopile can further be used in a non-temperature-controlled environment up to about 70 °C. The thermopile chosen for the first prototype is a quad-thermopile detector with four absorbers placed on a common reference plate ensuring high uniformity between the detector channels. An optical filter is placed in front of each detector, two of which are to be used for the target gas measurement and the two others are needed for measuring the H_2O concentration required for compensation of the residual water vapour signal.

The small optical filters are glued on top of the detector channels by the detector manufacturer. For the chosen detector each filter must be 0.5 mm thin and 2 mm x 2 mm wide. Customised filters are expensive and the small sizes helps keeping the cost down of a single filter. In return, it puts high demands on the filter dicing quality.

Thermal Decoupling and Waveguiding

The detector and emitter need to be thermally decoupled from the up to 500 °C hot exhaust gas. Thus, they are placed in some distance from the measurement chamber. The further away they need to be placed, the more intensity is lost. However, on the detector side this is partly compensated by a decrease in the thermal noise. The atmosphere between the optical windows and the detector and emitter must be infrared inactive in the wavelength range of interest. This might be ensured by nitrogen-filled gas-tight compartments while it is also possible to flush the optically inactive part with dry pressurised air. The thermal decoupling arrangement takes up space and increases intensity losses, but it has the one benefit that the extra space can be utilised to insert collimating optics in order to maximise the intensity throughput. The choice of optics is important for the optical filter setup for two reasons; the bandpass profiles of optical filters depend on the angle of incident, and the optical material inserted in the path may provide long wavelength blocking which relaxes the requirements to the optical filter. Magnesium flouride, MgF_2, is a good choice of lens material since it provides high transmission above 1800 cm^{-1} and blocks all light below 900 cm^{-1}. It is further insensitive to temperature changes. Thus, in the filter optimisation it is assumed that one 5 mm thick MgF_2 lens is inserted somewhere between the emitter and the detector.

Electronics and Signal Processing

The limitations in the detector sensitivity and emitter performance in the mid-infrared region, imply that high performance electronics and advanced signal processing algorithms are essential. Work on this side also took place within the HTF project concurrently with the optical filter optimisation.

3.2 Measurement Principle

This section describes the measurement principle behind the NDIR NO_X sensor including the concept of in-optics humidity compensation. The starting point is Beer-Lambert's law which relates the transmission of light through a volume of gas to the number density (N) of molecules in the gas;

$$\tau_\nu = \frac{I_\nu}{I_\nu^0} = \exp(-\sigma_\nu L N) \tag{3.1}$$

I_ν^0 and I_ν are the intensities of the ingoing light and the transmitted light, respectively. L is the length of the path of radiation through the gas, and σ_ν is the absorption cross section of the gas. The subscript $\nu = \frac{1}{\lambda}$ is the wavenumber which indicates that the variables with this subscript are wavelength dependent.

If more than one species of gas molecules are present in the gas volume, the transmission is given by;

$$\tau_\nu = \frac{I_\nu}{I_\nu^0} = \exp\left(-\sum_{\text{gas}} \sigma_\nu^{\text{gas}} L N^{\text{gas}}\right) = \prod_{\text{gas}} \exp(-\sigma_\nu^{\text{gas}} L N^{\text{gas}}) \tag{3.2}$$

where $\sum_{\text{gas}}$ and $\prod_{\text{gas}}$ covers all constituents of the gas.

The detector used in the sensor, is a so called thermopile detector which in essence works by measuring the difference in temperature between an absorber and a reference chip. The temperature difference is converted into a voltage through a series of thermocouplers and this is proportional to the difference in incident and outgoing radiation intensity on the detector channel, $u = s(I^{\text{in}} - I^{\text{out}})$, where s is the detector sensitivity and the outgoing radiation is the thermal radiation from the detector itself and thus depending on its own temperature. The detector acts as an integrator over the spectral distribution of intensity;

$$u = \int_0^\infty \mathrm{d}\nu \; s_\nu \; (I_\nu^{\text{in}} - I_\nu^{\text{out}}) \tag{3.3}$$

The intensity incident on the detector I_ν^{in} originates either from the controlled IR source (I_ν^0), from radiation from all other surfaces in the optical path (Background radiation), hot particles in the exhaust gas, or from the gas molecules themselves. Gathering all other contributions than the one from the IR source in a common background term (I_ν^{BG}), the incident radiation can be expressed as;

$$I_\nu^{\text{in}} = \tau_\nu^{\text{optics}} \; \tau_\nu^{\text{filter}} \; I_\nu^{\text{source}} \prod_{\text{gas}} \exp(-\sigma_\nu^{\text{gas}} L N^{\text{gas}}) + I_\nu^{\text{BG}} \tag{3.4}$$

where I_ν^0 has been replaced by the product $\tau_\nu^{\text{optics}} \; \tau_\nu^{\text{filter}} \; I_\nu^{\text{source}}$ to account for the transmission through the optical filters $\left(\tau_\nu^{\text{filter}}\right)$ as well as the additional optics $\left(\tau_\nu^{\text{optics}}\right)$.

Inserting equation (3.4) into (3.3) gives;

$$u = \int_0^\infty \mathrm{d}\nu \; s_\nu \tau_\nu^{\text{optics}} \; \tau_\nu^{\text{filter}} \; I_\nu^{\text{source}} \; \prod_{\text{gas}} \exp(-\sigma_\nu^{\text{gas}} L \; N^{\text{gas}}) + U_{\text{IR-Filter}}^{\text{BG}} \tag{3.5}$$

where I_ν^{BG} and I_ν^{out} have been combined in a common background term;

$$U_{\text{IR-Filter}}^{\text{BG}} = \int_0^\infty \mathrm{d}\nu \; s_\nu (I_\nu^{\text{BG}} - I_\nu^{\text{out}})$$

Assuming the optical filter to be a perfect bandpass filter that allows all frequencies within a range $\nu_1 - \nu_2$ to pass, while all other frequencies are blocked, and considering I_ν^{source}, τ_ν^{optics}, and s_ν to be constant within in this range, equation (3.5) can be rewritten into:

$$u = s_{\text{IR-filter}} \; I_{\text{IR-filter}}^{\text{source}} \; T_{\text{IR-filter}}^{\text{optics}} \int_{\nu_1}^{\nu_2} \mathrm{d}\nu \prod_{\text{gas}} \exp(-\sigma_\nu^{\text{gas}} L \; N^{\text{gas}}) + U_{\text{IR-Filter}}^{\text{BG}}$$

which is the voltage measured by one channel on the detector, equipped with a specific bandpass filter. In order to derive the desired gas concentration from the measured voltage, all the other unknowns in the equation has to be handled. The complex background term can be conveniently eliminated by the well-established method of modulating the source intensity, and the optical factors can be determined by calibration. Drifts in source intensity and transmission properties through the optical system over time can be compensated to a great extent by measuring a reference voltage with a reference channel that is equipped with a properly chosen reference bandpass filter. Finally, a proper choice of optical filters are used to reduce sensitivities to other present gas species than the target gas.

Source Modulation

Modulation of the source intensity can be expressed mathematically as

$$I^{\text{source}}_{\text{IR-filter}}(t) = I^{0}_{\text{IR-filter}}\left[m_{\text{S}}\sin(\omega_{\text{S}}\,t+\phi_{\text{S}})+\mu_{\text{S}}\right] \tag{3.6}$$

where m_{S} is the modulation depth, μ_{S} is the DC-offset or the mean value of the intensity, ω_{S} is the angular frequency, and ϕ_{S} is the phase.

The measured voltage is now time dependent:

$$u(t) = s_{\text{IR-filter}} I^{0}_{\text{IR-filter}}\left[m_{\text{S}}\sin(\omega_{\text{S}}t+\phi_{\text{s}})+\mu_{\text{S}}\right]\; T^{\text{optics}}_{\text{IR-filter}} \int_{\nu_1}^{\nu_2} \mathrm{d}\nu \prod_{\text{gas}} \exp(-\sigma^{\text{gas}}_{\nu} L\, N^{\text{gas}}) + U^{\text{BG}}_{\text{IR-filter}} \tag{3.7}$$

Fourier transforming this time signal results in a peak at the ω_{S} frequency with amplitude $A^{\omega_s}_{\text{IR-filter}}$;

$$A^{\omega_s}_{\text{IR-filter}} = s_{\text{IR-filter}} I^{0}_{\text{IR-filter}}\, m_s\; I^{\text{source}}_{\text{IR-filter}}\; T^{\text{optics}}_{\text{IR-filter}} \int_{\nu_1}^{\nu_2} \mathrm{d}\nu \prod_{\text{gas}} \exp(-\sigma^{\text{gas}}_{\nu} L\, N^{\text{gas}}) \tag{3.8}$$

which is independent of the background contribution. In practice a pure sinusoidal source intensity is difficult to realise and some overtones will also be present, and the amplitude of the peak at ω_{S} is reduced accordingly.

Reference Channel

To compensate for changes in the measured voltage, not related to gas absorption, an additional detector channel, equipped with a proper optical filter may be used to acquire a reference voltage with similar optical dependencies as the suspect channel. Taking the ratio between the ω_{S} frequency component of both suspect and reference channel results in;

$$R = \frac{A^{\omega_s}_{\text{sus}}}{A^{\omega_s}_{\text{ref}}} = \underbrace{\frac{s_{\text{sus}} I^{0}_{\text{sus}}\; T^{\text{optics}}_{\text{sus}}}{s_{\text{ref}} I^{0}_{\text{ref}}\; T^{\text{optics}}_{\text{ref}}}}_{\text{Calibration parameter},\beta} \underbrace{\frac{\int_{\nu_1^{\text{sus}}}^{\nu_2^{\text{sus}}} \mathrm{d}\nu \prod_{\text{gas}} \exp(-\sigma^{\text{gas}}_{\nu} L\, N^{\text{gas}})}{\int_{\nu_1^{\text{ref}}}^{\nu_2^{\text{ref}}} \mathrm{d}\nu \prod_{\text{gas}} \exp(-\sigma^{\text{gas}}_{\nu} L\, N^{\text{gas}})}}_{\text{Function of gas concentrations, } f(N_1,N_2,..)} \tag{3.9}$$

which shows that the ratio of the voltage amplitudes (R) can be described as the product of a term (β) that contains all setup-related variables, and a function (f) of the gas composition. Thus, R has the advantage of being immune to any changes that are equally affecting both the suspect and the reference channel, e.g. a uniform intensity change.

Interfering Gases

It is up to the optical filters to assure that f is sensitive to the gas of interest, in this case NO_X , and insensitive to other gas components. For water vapour which overlaps spectrally with both NO and NO_2 and therefore cannot be cut out by the optical filters, the sensitivity

may instead be minimised by ensuring that the response to water vapour is similar in the suspect and reference measurement.

To illustrate the concept, the wavelength dependent absorption cross section is approximated by an average value over the optical filter range ($\bar{\sigma}^{\text{gas}}_{\text{filter}}$). This approximation, which is only valid for weak absorptions, makes the integral in equation (3.9) disappear since $\int d\nu \exp(-\bar{\sigma}^{\text{gas}}_{\text{filter}}) = \Delta\nu_{\text{filter}} \exp(-\bar{\sigma}^{\text{gas}}_{\text{filter}})$, and allows f to be written in a simplified form;

$$f = \frac{\Delta\nu_{\text{sus}}}{\Delta\nu_{\text{ref}}} \frac{\exp(-\bar{\sigma}^{\text{NO}_2}_{\text{sus}} L\, N^{\text{NO}_2}) \exp(-\bar{\sigma}^{\text{H}_2\text{O}}_{\text{sus}} L\, N^{\text{H}_2\text{O}})}{\exp(-\bar{\sigma}^{\text{NO}_2}_{\text{ref}} L\, N^{\text{NO}_2}) \exp(-\bar{\sigma}^{\text{H}_2\text{O}}_{\text{ref}} L\, N^{\text{H}_2\text{O}})} \tag{3.10}$$

for the case where NO_2 and H_2O are the only abundant gases, absorbing in the selected spectral range. Equation (3.10) provides the logical result that the water vapour signal cancels out if a filter setup is chosen such that the average H_2O absorption in the two filter ranges are equal, i.e., $\bar{\sigma}^{\text{H}_2\text{O}}_{\text{sus}} = \bar{\sigma}^{\text{H}_2\text{O}}_{\text{ref}}$, while the sensitivity to NO_2 is improved by maximising $\bar{\sigma}^{\text{NO}_2}_{\text{sus}} - \bar{\sigma}^{\text{NO}_2}_{\text{ref}}$.

3.3 Filter Optimisation Routine

The overall purpose of the filter optimisation is to find the bandpass transmission profiles that maximises the sensitivity of the target emission gas while minimizing all other influences, in particular that of water vapour absorption.

Equation (3.9) is a nice illustration of the purpose of calculating the ratio of the voltage amplitudes (R). However, to reach it, a number of assumptions were necessary. In contrast, numerical calculations posses no need to assume rectangular filters or spectrally uniform source intensity, window transmission, or detector sensitivity. Any known spectral dependence may be properly calculated inside the integral before the ratio is found;

$$R = \frac{\int_0^\infty \mathrm{d}\nu\; s_\nu\, \Delta I^0_\nu\, \tau^{\text{optics}}(\nu)\, \tau^{\text{filter}}_{\text{sus}}(\nu) \prod_{\text{gas}} \exp(-\sigma^{\text{gas}}_\nu L\, N^{\text{gas}})}{\int_0^\infty \mathrm{d}\nu\; s_\nu\, \Delta I^0_\nu\, \tau^{\text{optics}}(\nu)\, \tau^{\text{filter}}_{\text{ref}}(\nu) \prod_{\text{gas}} \exp(-\sigma^{\text{gas}}_\nu L\, N^{\text{gas}})} \tag{3.11}$$

where $m_s I^0_\nu$ has been replaced by $\Delta I^0_\nu = I^0(T^{\text{S}}_{\text{hot}}, \nu) - I^0(T^{\text{S}}_{\text{cold}}, \nu)$ to account for the wavelength dependence of the source modulation as the spectral radiation changes with temperature.

The only limiting factor in the numerical calculation of R is how well the total system is known. Accurate simulations require knowledge of the spectral distribution of the IR-source intensity and detector absorptivity, as well as spectral transmission through the waveguiding optics, the microstructured optical windows, soot, particles, and other absorbing gas constituents present in the exhaust gas. Moreover, the dependencies of the spectral distributions as a function of temperature, ageing, or other conditions, are important in order to determine the stability of the measurement. Of these, the spectral radiation of the emitter was measured by my self, and the spectral absorptivity was measured by the supplier. However, a completely accurate spectral characterisation is difficult to realise and some uncertainties has to be accepted in the filter optimisation.

Having established the numerical expression for R and inserted all available spectral information, the figure to optimise is the sensitivity to the target gas over the sensitivity to

H_2O;

$$\chi = \left| \frac{\frac{\partial R}{\partial N^{\text{gas}}}}{\frac{\partial R}{\partial N^{\text{H}_2\text{O}}}} \right| \tag{3.12}$$

The are several other sensitivities to minimise, including the sensitivity to changes in the gas temperature, source drift, temperature induced transmission changes in the optical windows, and cross sensitivities to other interfering gases in the exhaust gas, such as formaldehyde (H_2CO). Further, the absolute absorption of the target gas should be maximised to increase the signal to noise ratio. However, because water vapour interference is the most critical parameter, χ is the prime figure to optimise. If there exist more filter setups that yields satisfactory χ values, these may subsequently be evaluated with respect to the other concerns.

Modelling the Optical Filters

Essential in the filter setup optimisation is the description of the optical filter and its tolerances. A fully identifying description of a bandpass profile is relatively comprehensive and requires a number of parameters to be specified. A bandpass filter may be characterised by the position of the two edges, e.g., the wavenumber position at which the transmission equals 50 % of the maximum bandpass transmission, the slopes of the edges, the flatness of the passband transmission which is often subject to ripples, and the rejection level outside the bandpass (out-of-band blocking), as well as the blocking range. The first two parameters, i.e. the edge positions, are simple to implement and vary in a filter optimisation routine. In practise the edge position can be varied continuously and independently of the other bandpass characteristics. However, they are subject to position tolerances.

Typical specified tolerances on edge positions for customised optical filters are 0.5-1 % of the specified wavenumber, corresponding to 8-16 cm^{-1} at 1600 cm^{-1}, a spectral interval which is likely to contain several absorption lines. The impact of the edge position tolerances is visualised in Figure 3.5 where two manufactured optical filters are shown with 0.5 % edge displacements indicated. The filters are shown together with calculated absorption spectra for NO, NO_2, and H_2O for a 350 °C hot gas at 1 atm and for a pathlength of 25 cm. Figure 3.5 also shows absorption spectra for two other interfering gases; SO_2 and H_2CO, which are present in exhaust gas. Thus, manufacturing tolerances are of critical importance when designing optical filters aiming to spectrally discriminate between closely spaced or overlapping absorption lines.

The slopes of the edges may be varied independently for wide bandpass filters, or as a common parameter for narrow bandpass filters, the distinction between which is covered in Chapter 4. However, the slopes cannot be varied without consequences for the passband transmission. Steep edges requires more thin film layers which causes more ripples in the passband. Figure 3.5 shows that a filter for NO_2 measurement which is required not to overlap with SO_2 will benefit from a steep long wave edge in that the 50 % edge position may be placed closer to the SO_2 band compared to if the edge was less steep. However, when it comes to humidity balancing and the position tolerances are taken into account, steep edges are more sensitive to wavenumber displacements compared to more gentle edges. Thus, it makes sense to include the slopes as parameters in the optimisation and not just aiming for the steepest. Flatness criteria are commonly specified by a certain percentage of the average

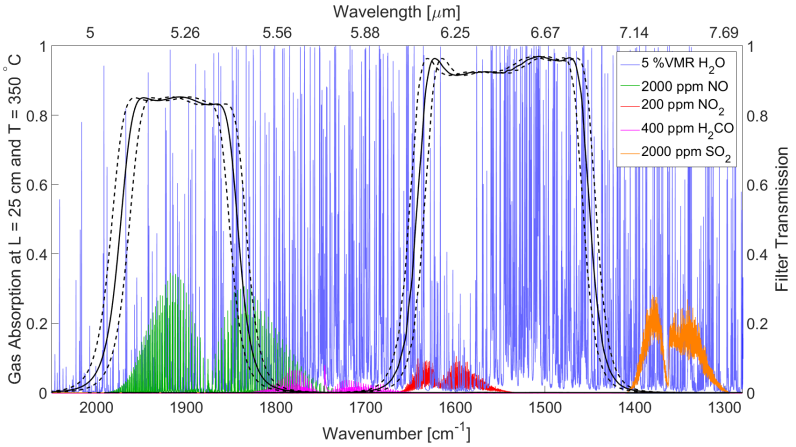

Figure 3.5: Measured transmission profiles of manufactured optical filters (solid black curves) with edge-position tolerances of 0.5 % of wavenumber indicated (stipulated black curves) shown together with calculated absorption of NO, NO_2, SO_2, H_2CO, and water vapour for possible concentrations in 350 °C hot exhaust gas at 1 atm and a pathlength of 25 cm. The simulations were performed using SpectralCalc [35] and HITRAN2008 [42].

passband transmission that the transmission over the passband must not deviate from. Thus, it is generally treated as a tolerance and is not included as a parameter in the search for the optimum filter setup. However, well defined ripples are not in themselves critical; if they are known they may be included in the filter profile description. This could potentially be a way to relax the flatness requirements if causing problems for the filter manufacturer. Out-of-band blocking is typically a requirement that the transmission must not exceed a certain value outside the bandpass, typically between 10^{-3} and 10^{-4}, and within a certain blocking range defined by the sensor sensitivity and the presence of blocking components in the optical setup. The blocking level and blocking ranges are not a part of the filter optimisation but needs to be assessed independently.

To sum up, for the purpose of the following filter optimisation, each filter is described by two parameters representing the edge positions as well as one or two parameters for the slope of the edges.

Simulation

The aim of the simulation is to determine the best possible two-filter setup, with respect to minimised water vapour sensitivity, determined by calculating χ for every possible filter setup combination. With three to four parameters per filter, a two-filter setup is described by six or eight parameters. For each of these, a range and a stepsize must be defined, and this quickly adds up to a substantial number of possible filter setups. For instance, if in the search for a filter setup for NO measurements, the short wave edge frequency (ν_{SW}) of the

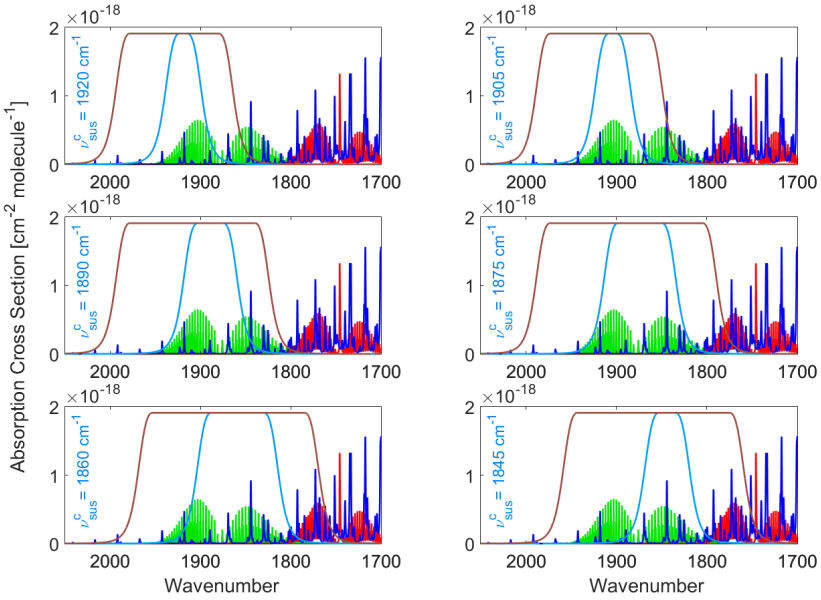

Figure 3.6: Illustration of optimised filter setups for different centre wavenumbers of the suspect filter. The colours of the absorption cross sections refer to NO (green), H_2O (blue), and H_2CO (red). Each subfigure shows the optimum filter setup found for a fixed ν^c_{sus} with the three other edge parameters parameters varied. The solution with the highest χ value is shown. Note that the suspect filter to a large extend avoids the present formaldehyde and that the reference filter stretches over both sides of the suspect filter even though no contraints of this kind were imposed.

suspect filter is varied between 1820 cm^{-1} and 1960 and the other edge is varied between ν_{SW} + 40 cm^{-1} and 2000 cm^{-1} in steps of 10 cm^{-1}, roughly corresponding to one position tolerance (ϵ), and the reference filter is varied in the same way independently from the first filter but with the restriction that the second filter must be broader than the first to avoid calculating the same filter setup twice, this exceeds 12000 combinations. If each filter is further allowed three different slopes, this increases to over 50000 filter setup combinations. Additionally, for each of the filter combinations, the tolerances has to be considered. In principle, it is the worst χ value within the tolerances of a given filter setup that is of relevance because a large χ value is only interesting if it is realisable within the manufacturing tolerances. It is hardly possible to evaluate every possible tolerance permutation but assuming that the most critical case is a full ϵ shift for one or more of the filter edges, then the tolerances may be included by letting each edge move between -ϵ, 0, and +ϵ giving a total of $3^4 = 81$ permutations within each of the already numerous combinations. The passband flatness tolerances might be included by a number of randomly rippled passband transmissions. However, it is

probably better to deal with the flatness tolerances during the manufacturing process as it was done for the NO_2 filters presented in Section 3.4.

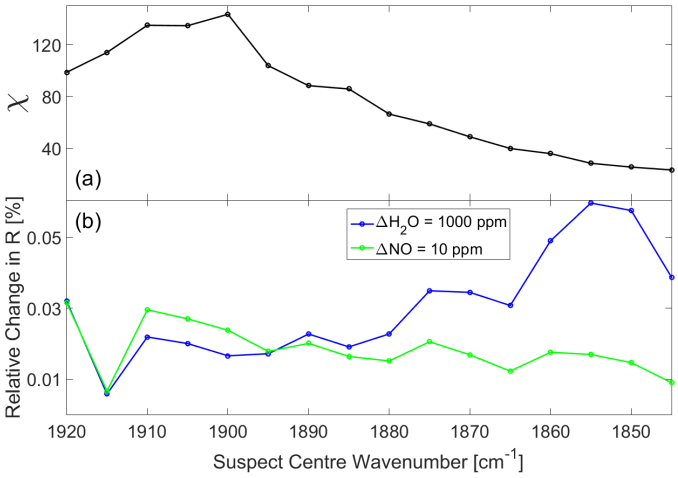

Figure 3.7: (a) Maximum χ values for fixed values of ν^c_{sus}. (b) Corresponding change in R for a change of 10 ppm NO (green) and for a change of 1000 ppm H_2O (blue). The calculated χ values are based on absorption cross sections at 300 K calculated using SpectralCalc [35] and HITRAN2008 [42].

Figure 3.6 shows six examples of the results of an optimisation process for a set of NO filters where the centre wavenumber of the suspect has been fixed to a certain value. The calculations in this example are based on absorption cross sections at 300 K. However, the example serves as a nice illustration of the optimisation procedure. The two edge positions have been replaced by a centre wavenumber (ν^c_{sus}) and the FWHM of the bandpass filter which are the two parameter used to specify the edge positions for narrow bandpass filters as will be discussed in chapter 4. However, the parameter range and stepsizes are effectively equal to the ones suggested above, with the exception that ν^c_{sus} is varied in steps of 5 cm$^-1$. In each subfigure, the centre wavenumber of the suspect filter is shown while the remaining parameters have been varied and the filter setup that maximises χ at the given ν^c_{sus} is shown. In this example the slopes were not varied, instead the edge shapes were fixed and taken from a previously manufactured bandpass filter.

No restrictions were set about filtering out H_2CO and nor any requirement that the reference filter should be distributed over both sides of the suspect band, although this is desirable in order to improve stability toward optical variations such as a drift in source intensity or the presence of particles. The setups are a direct consequence of the maximisation of χ and the fact that the water vapour absorption increases effectively monotonously from one side of the NO band to the other, implying that to achieve a similar average H_2O absorption in the two optical filters, it is necessary to include wavelengths outside both sides of the suspect

filter in the reference filter.

Figure 3.7 shows the resulting maximum χ values for various fixed values of ν^c_{sus}. The overall maximum is found at ν^c_{sus} = 1900 cm^{-1}, ν^c_{sus} = 1910 cm^{-1}, FWHM$_{\text{sus}}$ = 40 cm^{-1}, and FWHM$_{\text{ref}}$ = 170 cm^{-1}. It should be noted that the maximum is found at the smallest allowed width and thus, it is very possible that an even more narrow filter would increase the χ value further. Ultimately, deciding the width of the suspect filter might be a trade between absolute absorption signal, determining the signal-to-noise ratio, and the relative absorption signal, determining the stability to various sensitivity factors. However, Figure 3.7 also shows that the optimum for a fixed ν^c_{sus} of 1910 cm^{-1} has a 24 % larger relative response to NO $\left(\frac{\delta R}{\delta N^{NO}}\right)$, while χ is only 6 % weaker corresponding to an NO response to 1000 ppm H_2O of 7.4 ppm instead of 7.0 ppm. The relative response to NO is important because it reduces all other known and unknown sensitivity factors of the systems. Thus, the optimum at ν^c_{sus} = 1910 cm^{-1} could be a better alternative. However, the solution space might conceal better compromises than the one revealed in this one-parameter representation. The optimisation presented includes four parameters and while it is simple to find global maxima of a specific performance factor it is a challenge in its own to find the best compromises between more performance factors. Figure 3.7(b) shows a sudden dip at ν^c_{sus} = 1915 cm^{-1} although the χ value in Figure 3.7(a) appears to follow a smooth curve over the same value of ν^c_{sus}. This is a result of a competing maxima in the 5D χ contour, that sacrifices NO sensitivity in return for a very good H_2O balance, further illustrating that it is dangerous to rely on χ as a sole parameter.

3.4 NO_2 Results

Very early in the PhD project an opportunity occurred to have an optical filter for NO_2 measurement manufactured by IML and embedded in the first NO_X prototype in the related HTF project. This prototype was build with the focus of testing the signal-to-noise ratio in dry gas and had no formal requirements to the humidity cross sensitivity. However, it provided an important platform for experimental testing and verification of the theoretical calculations, as well as kick-starting the communication with the filter manufacturer and generally gaining experience with the complete filter optimisation and fabrication process. There were several reasons that the first filter result would be of preliminary quality; one of them being that the optical setup of the sensor was being developed concurrently, implying that the complete spectral characteristics of the optical path could not be properly included in the spectral calculations. Thus it was accepted that there would be another round of filter development, and this allowed me to cut a few corners in the hastened optimisation procedure. I decided to focus on developing a filter set for NO_2 measurements. The interference with water vapour is slightly worse for NO_2 compared to NO. However, the absolute absorption signal is much stronger than for NO. This increased the chances for obtaining results on the discriminating performance even if the signal-to-noise level requirements were not met with the first prototype.

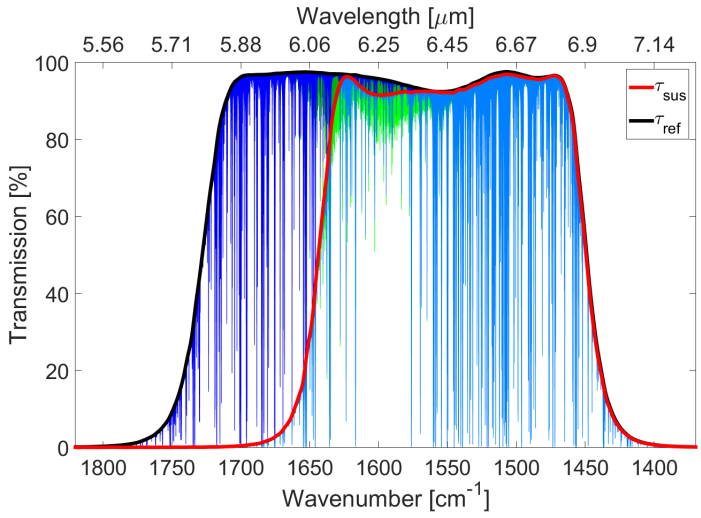

Figure 3.8: Measured transmission profiles of manufactured NO_2 filters (solid red and black curves), and the simulated spectral transmission seen by the two detector channels in the presence of 5 %VMR (blue) and 300 ppm NO_2 (green) at a pathlength of 25 cm.

The optimisation that was carried out was based on absorption cross sections calculated for gas temperatures of 500 °C and using the HITRAN2008 database [42]. The calculation of the absorption cross sections were done using the commercial software SpectralCalc.com

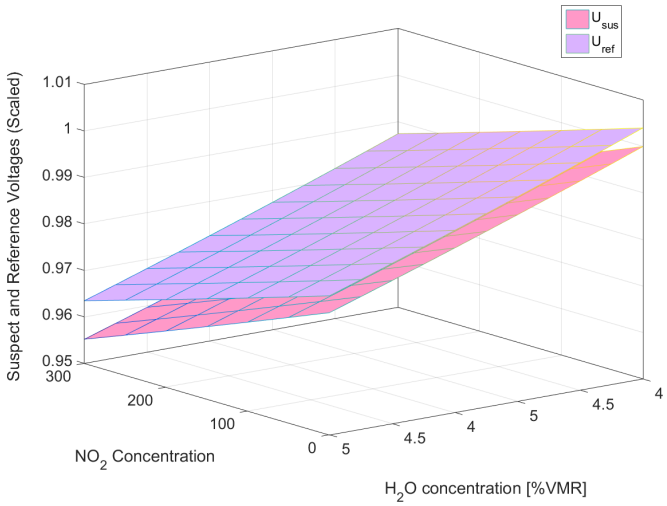

Figure 3.9: Simulated voltages of the two detector channels equipped with suspect and reference filters. The voltages are scaled independently for visualisation purposes. Each voltage is very sensitive to H_2O compared to NO_2. However the response to H_2O is very similar on the two detector channels, implying that it cancels out when calculating the ratio between them.

[35]. HITRAN2008 was chosen mainly because of availability since at the time the simulations were made, HITRAN2012 and HITEMP2010 were not yet available for cross section calculations with SpectralCalc.com. The ideal databases to use would be HITEMP2010 for H_2O and HITRAN2012 for NO and NO_2 however, the database updates are not expected to change the qualitative conclusions made in this chapter, even though the water absorption spectrum has been considerably extended with numerous weak absorptions lines which might slightly affect the optimum filter setup.

The optimisation neglected cross sensitivities to all other gases than H_2O and SO_2, even though formaldehyde (H_2CO) is absorbing in the same wavelength range, and is a trace gas in combustion of diesel oil. However, the level of its presence in exhaust gas is unclear. H_2CO is measured as a tracer for OH in combustion diagnostics [43] but the very toxic gas was only present in concentrations of few ppm in an old study of the composition of diesel exhaust gas [44]. Thus, cross sensitivity to H_2CO may not be a severe issue in exhaust gas measurements, however it should be given more attention in the second optimisation round.

The optimisation assumed a 5 mm thick MgF_2 lens in the optical setup while the transmission of the microstructured windows where not included as they were unknown at the time.

The optimisation followed the same procedure as described in Section 3.3. However, it was carried out in a number of steps. First, the simulation was done with fixed filter

slopes which originated from a real filter. Then after the first manufacturing, the edges were updated according to that outcome. Since the filters were broad bandpass filters, each edge of a filter was made in independent deposition runs, as discussed in Chapter 4. This provided the opportunity to include and fix each edge at a time upon its manufacture and rerun the simulations to determine an adjusted optimum for the remaining edge position parameters and deliver those back to the filter manufacturer. In this way IML was able to produce a set of filters with a better χ value than in the original simulation.

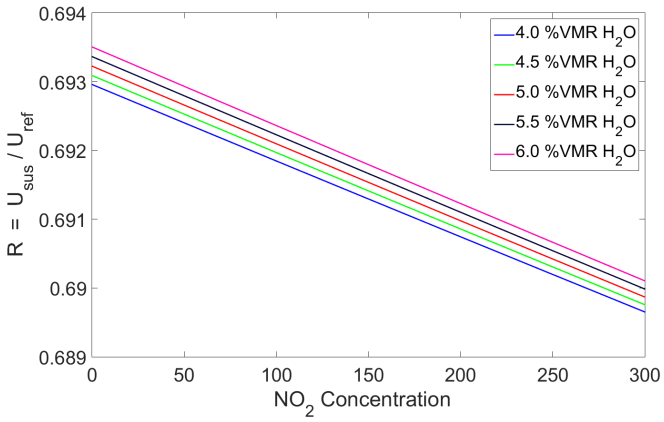

Figure 3.10: Simulated ratio of voltage amplitudes for various NO_2 and H_2O concentrations. The ratio shows significantly reduced H_2O sensitivity compared to NO_2. A change in 1000 ppm H_2O corresponds to a change of 2.3 ppm NO_2.

The realised manufactured filter setup for NO_2 is shown in Figure 3.8 together with the transmission spectrum seen by the two detector channels behind the filters in the presence of 5 %VMR H_2O and 300 ppm NO_2 for an exhaust gas temperature of 350 °C at 1 bar and over a pathlength of 25 cm. This result was published in a conference paper (Appendix A) and presented orally at Advanced Photonics Meeting Congress 2014.

The simulated voltage amplitudes on each of the two detector channels are shown in Figure 3.9 as a function of the water vapour concentration and the NO_2 concentration. The two voltages are each very sensitive to H_2O but their H_2O dependence is very similar as a result of the filter optimisation that balances the H_2O signal in the two channels. When the ratio of the two channels are taken, the result is that most of the water vapour dependence cancel out as shown in Figure 3.10. The χ value calculated based on the manufactured filter set is 313, which corresponds to a change of 3.2 ppm NO_2 when the H_2O changes by 1000 ppm (= 0.1 %VMR). If the water vapour is measured with an accuracy of $\pm$ 1600 ppm corresponding to $\pm$2 % of 8 %VMR which is the upper range for the H_2O content, this transfers to an uncertainty in the NO_2 measurement of $\pm$ 5.1 ppm. This satisfies the requirement stated in 1.1 that the cross sensitivity to water vapour must be well below 12 ppm, although at the same time, it maintains the postcompensation of the water vapour

signal as a critical issue.

Opening Angle

The filter supplier provided transmission measurements at various incident angle distributions which are shown in the inset in Figure 3.11. For each set of transmission profiles corresponding to a certain cone angle of the incident light, χ was calculated and shown as a function of the cone angle in Figure 3.11. The χ value is almost insensitive to the cone angle which means that no special consideration must be shown to the cone angle when designing the optical filter, since the detector itself has an acceptance angle of 30°.

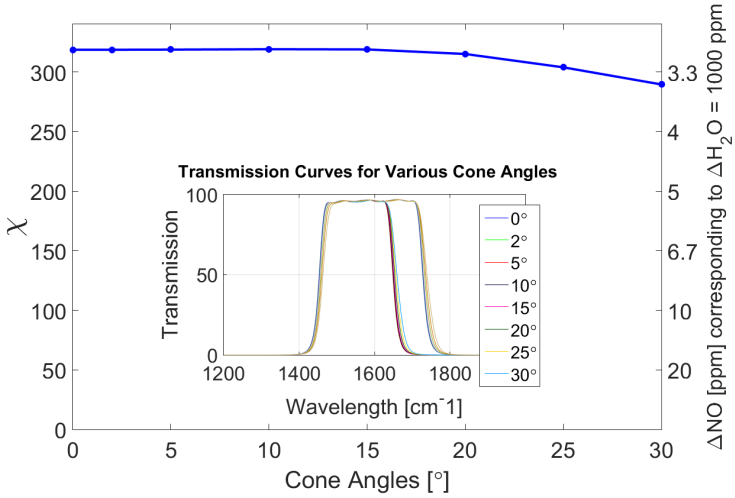

Figure 3.11: χ value as a function of the cone angle of the incident light, calculated based on measured filter transmission profiles, which are shown in the inset.

Temperature Dependence

At the time when the NO_2 filters were manufactured, IML did not have equipment for elevated temperature characterisation of the bandpass profiles which had not previously been requested. Therefore the temperature dependence of the NO_2 filters were only determined a year after delivery, during my research visit at IML, prior to which heating equipment had been established. The measurements revealed a large temperature dependence of the NO_2 filters. This, I learned, was a consequence of the high stability toward incident angle, since there exist a general trade-off between the sensitivity to temperature and incident angle. The measured transmission profiles at different temperatures are shown in Figure 3.12. Note that the bandpass profiles are not identical to those in Figure 3.8 because the measurements

were done on a prototype filter which had a pronounced ripple. However, the measured temperature dependence is representative also for the final NO_2 filter set, since we showed in [2] that ripples do not affect the wavelength shift with temperature.

The consequence of the temperature behaviour is that a filter temperature change of 1 °C corresponds to a change in NO_2 of 23 ppm. This relatively high sensitivity to filter temperature may be dealt with by thermostabilisation of the detector or compensated for in the signal processing, but it would be highly preferable if it could be considerably reduced at the filter level.

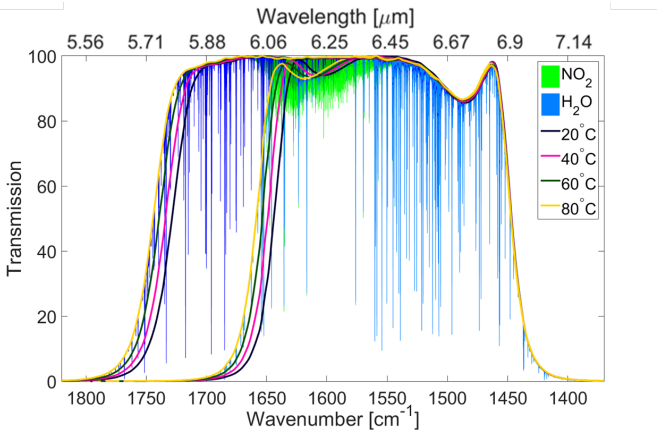

Figure 3.12: Normalised transmission profiles of the manufactured optical NO_2 filters measured at different filter temperatures. A change in filter temperature of 1 °C corresponds to a change in the NO_2 of 23 ppm.

While trading off the temperature stability for a high incident angle stability was unintentional from my side, the measured temperature dependence of the bandpass profile discloses an extremely interesting asymmetry in the wavelength shift with temperature. The overall temperature shift is high, but this covers a very high shift of the short wave edge while the long wave edge is practically invariant to temperature changes. With this knowledge, it should be be possible to produce a set of filters with a high temperature stability by incorporating the temperature variations of the short and long wave edges into the simulations. In this way the temperature invariant edge would be placed where the position stability is most critical, while the edge that shifts with temperature could be the common edge of the two filters.

3.5 Next Generation Filter Setup Optimisation

In may 2012, 14 month into my PhD project, Danfoss IXA decided on a change of technology away from NDIR and officially withdrew from the HTF project. This meant that my theoretical work was never experimentally verified because this was depending on

electronic and software development within the project. It further inferred that there were to be no second round of filter development, despite promising results from the first round. This section summarises the learnings from the first optimisation and filter development process and sketches how these might be adopted in a second generation filter setup optimisation.

For bandpass filters there tend to be a trade-off between stability to incident angles and stability to temperature. Thus a request for a low opening angle sensitivity should be made in consideration of the consequence for the temperature dependence. However, this might not be trivial; the sensitivity to incident angle is a geometrical problem and can be calculated for a certain multilayer structure before manufacturing, but this is not the case for the temperature dependence, which depends on the thermo-optical properties of the thin film materials. These properties turn out to be generally unavailable, as will be discussed in Chapter 4. Therefore it was a significant result that Gary Hawkins and I managed to extract thermo-optical thin film properties of PbTe and ZnSe from a large repository of historic bandpass filters and apply these properties to accurately predict the temperature behaviour of bandpass filters (Appendix B and C). The negative thermo-optical coefficient of PbTe enables temperature invariant edges in bandpass filters as it was the case for the long wave edge for the fabricated NO_2 filters. This should be exploited by determining a set of promising filter edges, in the case of the broad bandpass filters required for NO_2, and let these be input to the filter optimisation together with their dependencies.

For narrow bandpass filters the number of possible bandpass profiles are quantized. The centre wavenumber is continuously variable, since this scales linearly with the layer thicknesses. However, the possible widths and bandpass shapes depend on the available materials, and for the mid-infrared region there are only a limited number of suitable materials. With additional requirements regarding temperature stability only a limited narrow bandpass profiles are available. Thus, in a next generation of filter optimisation for NO, which requires narrow bandpass filters, rather than working with continuous parameter for both the centre frequency and the width, the two characteristic parameters of each filter should be a continuous centre wavenumber and a set of good bandpass profiles.

Since the NO_2 measurement requires a simultaneous humidity measurement for compensation of the residual cross sensitivity, a next optimisation might include two additional filters for H_2O measurement. Four different optical filters provide four independent equations and can provide simultaneous information about a maximum of four variables. At least one variable is reserved to the intensity factor that varies with e.g., source temperature and soot level, leaving three variables for gas concentrations, two for NO_2 and H_2O, while the fourth equation might be used to solve the potential cross sensitivity to formaldehyde.

3.6 Discussion

In this PhD study the concept of in-optics humidity compensation has been theoretically investigated and actual filters have been manufactured with promising results. However, without experimental verification, the attempt of balancing the H_2O signal with carefully designed optical filters remains an idea. This thesis has not discussed the absolute signal level, although the main reason for Danfoss IXA to abandon NDIR for NO_X measurements in exhaust gas was the low signal-to-noise ratio of the NO measurement which was eventu-

ally considered incompatible with the requirements to accuracy, response time, and budget. However, signal-to-noise ratio depends on many other factors, including optical setup and detector sensitivity, which may be increased by use of detectors that requires cooling. Further, there is some elasticity in relaxing the response time or accuracy requirements of the sensor. Most of these factors affecting the signal-to-noise ratio do not interfere with the study of cross sensitivities which has been the focus of this work. The presented results and conclusions remains valid if the future offers improved technologies in the mid-infrared region. It should be noted that the NDIR NO_X sensor was given up because of the absolute signal level of NO and not NO_2 which offers an order of magnitude stronger absorption compared to NO. By other methods such as chemiluminescense and UV spectroscopy, NO_2 is more difficult to measure compared to NO. Thus, an NDIR exhaust gas sensor measuring NO_2 without NO might find its application some day.

3.7 Conclusion

Based on precise optical filtering, NO_2 measurements in moist exhaust gas has been analysed through theoretical simulations, and two optical filters were successfully manufactured within the tight tolerances required. The work presented in this chapter predicts that NO_2 can be measured in the mid-infrared region by a simple two-channel NDIR sensor, although very good control of temperature is required for the realised set of NO_2 filters. The estimated cross sensitivity to H_2O is that a change of 1000 ppm H_2O corresponds to a change of 3.2 ppm NO_2 at a gas temperature of 350 °C. The presented discoveries further suggests that there are significant improvements to be made in regard to temperature stability of the filter setup.

CHAPTER 4

Temperature-Invariant Optical Filters

My interest in optical filter design was originally driven by the need to mathematically describe and incorporate the transmission profile of an optical bandpass filter as well as its dependences and tolerances into the filter optimisation routine. It soon became clear that this was not a straightforward task, and therefore a research visit was planned at Infrared Multilayer Laboratory (IML) at the University of Reading with the purpose of gaining knowledge about fabrication uncertainties, interdependencies, and trade-offs involved in optical filter design and manufacturing. Prior to the visit, I commenced building my numerical filter optimisation routine, and the first set of filters for NO_2 measurements were manufactured at IML, a process which involved numerous correspondences, including a visit to IML. While the delivered filters were in many ways successful, they exhibited a large and asymmetric temperature dependence, which compromised their performance as discussed in Section 3.4. In the correspondences with IML, focus was given to the unfinished optical design for which reason the filter was designed to be insensitive to incident angle. I did not realise at the time that this came at the expense of a larger temperature dependence. I believed that temperature shift toward longer wavelengths with increasing temperature was a fundamental property of optical filters, caused by expansion of the optical thickness. However, the NO_2 filters did not just exhibit a large wavelength shift with temperature, the two edges of the filters shifted in a very asymmetric manner, and the bandpass profiles were moving in the wrong direction; toward shorter wavelengths with increasing temperature. This peculiar behaviour is caused by one of the embedded thin film materials, PbTe, which possesses the unusual property that its refractive index changes negatively with increasing temperature. Used together with a thin film material exhibiting positive thermo-optical properties, this can lead to a variety of different temperature behaviours, depending on the multilayer design used to construct the filter. This includes filters that do not shift with temperature. However, at the time of my visit at IML it was not possible to predict how a certain multilayer bandpass filter would behave with temperature because the available thermo-optical properties of PbTe and ZnSe, which constituted the second thin film material in the NO_2 filters, were not representative for the thin film filters and resulted in highly unreliable temperature predictions. Since, Head of IML Gary Hawkins was very eager to understand how the multilayer design affected the temperature behaviour of a filter and ultimately to be able to design temperature invariant filters, and he further had the idea that his extensive production of PbTe/ZnSe optical bandbass filters over the years could provide some of the answers, this opened up for a

common research study within design of temperature invariant optical filters and extraction of thermo-optical properties of embedded thin films in multilayer structures. I shall return to and elaborate on this work and associated results in Section 4.3, but first a brief introduction to thin film optical filters is given from the perspective of a spectroscopist.

4.1 Principles of Thin Film Optical Filters

Thin film optical filters are also called interference filters because the working principle is interference between electromagnetic waves. When an electromagnetic wave is incident to a boundary between two transparent materials with refractive indices n_0 and n_1 then the wave is partly transmitted and partly reflected. In the following the simplified case of non-absorbing materials is considered. Figure 4.1 sketches an electromagnetic wave incident on a thin film of thickness d_1, and refractive index n_1 on top of a substrate of refractive index n_2.

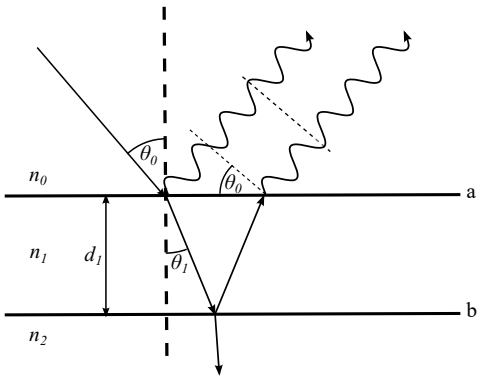

Figure 4.1: Sketch of the working principle of thin film optical filters. In this example the reflected beams are interfering destructively with each other which results in a high transmission.

At the first interface, the reflected beam is subject to a phase shift of π if $n_1 > n_0$ while no phase shift occurs if $n_1 < n_0$. When the transmitted beam reaches the second interface, the beam is again split into a reflected and a transmitted part. If the reflected beams from the first and the second interfaces are out of phase by π, they interfere destructively, and if they are further similar in magnitude, the reflections cancel each other out, causing a very high effective transmission; a phenomenon which is widely exploited in antireflective coatings. For the thin film in Figure 4.1 the magnitude constraint is satisfied when $n_1 = \sqrt{n_0 n_2}$, which can be shown from the Fresnel equations [45], and this implies identical phase shifts of the two reflected waves. Hence, they interfere destructively when the distance travelled in the thin film of index n_1 provides a phase shift of π. This happens when the optical thickness of the film ($dn_1 \cos\theta_2$) equals one quarter of the wavelength in vacuum. Thus, a single thin

film of one quarter wavelength thickness may be used as antireflective coating, although only within a narrow wavelength range.

In fact, a stack of thin films of quarter wavelength thicknesses, a so called quarter-wave stack, constitutes a building block within thin film optics. In the quarter-wave stack, however, the refractive indices of the thin films are alternately high and low, which causes phase shift of π only at every second boundary, resulting in high reflective properties. However, over a range of wavelengths, this structure generates a series of high-reflection zones separated by high-rejection zones, and the quarter wave stack may therefore be utilised to construct both antireflective coatings, high-reflection coatings, bandpass filters, as well as edge filters, i.e. long pass or low pass filters.

For any given stack of thin films, also referred to as a multilayer, the transmission properties can be straightforwardly calculated. Even before computers were available, this was possible since every layer can be represented by a (2x2) matrix, relating the incident and the transmitted electromagnetic field [46]. For the layer sketched in Figure 4.1 the matrix is;

$$\begin{bmatrix} E_{\mathrm{a}} \\ H_{\mathrm{a}} \end{bmatrix} = \begin{bmatrix} \cos\delta_1 & i\sin\delta_1/\eta_1 \\ i\eta_1\sin\delta_1 & \cos\delta_1 \end{bmatrix} \begin{bmatrix} E_{\mathrm{b}} \\ H_{\mathrm{b}} \end{bmatrix} \tag{4.1}$$

where $\delta_1 = d_1 n_1 \cos\theta_1 2\pi/\lambda$ is the optical distance through the layer, with d_1 and n_1 being the physical thickness and the refractive index of the layer, respectively, while $2\pi/\lambda$ is inserted to express the optical thickness in unit of the wavelength. η_1 is the optical admittance which is a material property of the thin film layer. E and H represent the electric and magnetic fields at the thin film boundaries a and b, indicated in Figure 4.1.

For an assembly of thin films this can be written in a normalised version as;

$$\begin{bmatrix} B \\ C \end{bmatrix} = \left\{ \prod_{\mathrm{m}=1}^{\mathrm{q}} \begin{bmatrix} \cos\delta_{\mathrm{m}} & i\sin\delta_{\mathrm{m}}/\eta_{\mathrm{m}} \\ i\eta_{\mathrm{m}}\sin\delta_{\mathrm{m}} & \cos\delta_{\mathrm{m}} \end{bmatrix} \right\} \begin{bmatrix} 1 \\ \eta_s \end{bmatrix} \tag{4.2}$$

where $C = \frac{E_a}{E_{q+1}}$, $B = \frac{H_a}{E_{q+1}}$, and η_s is the optical admittance of the substrate while q is the number of thin films in the assembly.

From C and B reflectance (R), transmittance (T), and absorptance (A), of the filter assembly may be calculated by the following relations according to [46] in which a thorough derivation can be found.

$$R = \left(\frac{\eta_0 B - C}{\eta_0 B + C}\right)\left(\frac{\eta_0 B - C}{\eta_0 B + C}\right)^* \tag{4.3}$$

$$T = \frac{4\eta_0 \mathrm{Re}(\eta_s)}{(\eta_0 B + C)(\eta_0 B + C)^*} \tag{4.4}$$

$$A = \frac{4\eta_0 \mathrm{Re}(BC^* - \eta_s)}{(\eta_0 B + C)(\eta_0 B + C)^*} \tag{4.5}$$

With these relatively simple equations at hand, and with todays computer power available, the calculation of the resulting transmission profile of any given multilayer is easy, provided the material properties are known. However, typically it is the reverse problem that

is of interest, i.e. to find the multilayer design that generates a desired transmission profile. This task is significantly more complicated, and is undertaken by a combination of design rules and brute force simulations where small changes are applied to the multilayer one at a time, while the resulting changes in transmission profile is evaluated. This together with a great deal of experience into thin film material properties and manufacturability enables the filter manufacturer to design and produce optical filters according to specified requirements.

4.2 Wide Bandpass Filters and Narrow Bandpass Filters

One thing a spectroscopist is likely to encounter when ordering bandpass filters is that the filter manufacturer distinguishes between wide bandpass (WBP) filters and narrow bandpass (NBP) filters. I personally found this awkward and a bit disturbing in the beginning, particular since there is no clear boundary between the two types of filters and apparently no significant differences to the characteristics of the transmission profile which are subject to similar tolerances. A WBP filter is identified by its cut-on and cut-off edges, while a NBP filter is identified by the centre wavenumber and the filter width (FWHM). However, it is very easy to translate between the two ways of specifying a bandpass profile, so why should the spectroscopist bother with this distinction?

However, although they might look similar to the costumer, the two types of bandpass filters are completely different seen from the design and manufacturing perspective, and it also turns out that the two types of filters do have some different properties that are worthwhile noticing for the spectroscopist.

The broad bandpass filters are also referred to as edge filters because they consist of two independent high-pass and low-pass edge filters placed in series to add up to a bandpass filter. The two edge filters are often deposited on either side of the substrate which imply that they are deposited in separate runs. This means that two different filters may have a common edge that is manufactured in the same deposition run, and this common edge will be close to identical for the two filters both in terms of wavenumber position as well as temperature sensitivity.

For narrow bandpass filters, the combination of low-pass and high-pass filters is not very successful because it is difficult to produce steep edges at high position accuracy. Instead other multilayer structures are used where the rejection band and the passband are produced in a single assembly. The simplest multilayer structures that provide this are denoted Fabry Pérot narrow band pass filters because they work as Fabry-Pérot interferometers utilising constructive interference between two reflective surfaces to obtain a narrow peak of high transmission. The filter is constructed by a half wave thick film embedded in a quarter-wave stack, resulting in a narrow peak of high transmission inside a region of high reflectivity. The half-wave thick layer has the same effect as a cavity and is therefore referred to as spacer or cavity. The resulting narrow bandpass filters become more rectangular if the quarter-wave stack is repeated one or two times as shown in Figure 4.2. More than three filters are normally avoided [47].

Figure 4.3 shows an enlarged photo of a cross section of a narrow bandpass filter with three spacer layers embedded in quarter-wave stacks. Upon these, two other quarter-wave stacks with reference to other wavelengths are providing long wave blocking. Short wave

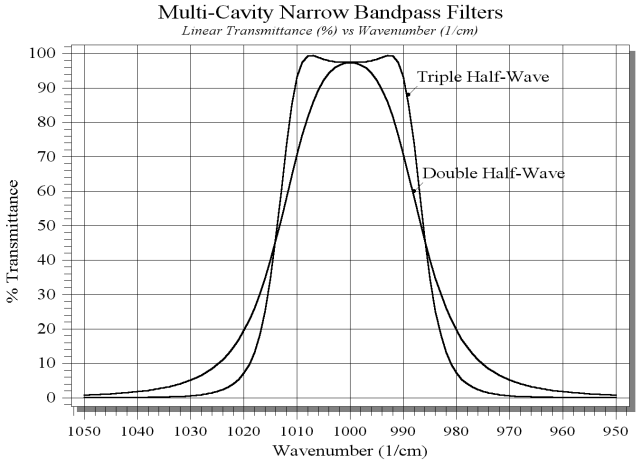

Figure 4.2: Narrow bandpass filters embedding two and three spacer layers. The bandpass profile becomes more rectangular with increasing number of spacers. The figure is provided by Gary Hawkins.

blocking, in contrast, is provided by the semiconductor absorption edge in the Germanium substrate material. It should be noted that Germanium is not a good substrate material for filters used at elevated temperatures since it looses transmission with increasing temperature above 50 °C. Instead, ZnSe is a good substrate.

The thickness of the spacer layers may be increased to higher integer multiples of half waves which results in narrower bandpass profiles, and each spacer may be of different multiple half-wave thickness to reach other desired bandwidths. Further, more than two different thin film materials may be combined to extend the number of possible bandpass shapes. However generally, the number of realisable narrow bandpass profiles are quantized.

4.3 Temperature Dependence of Thin Film Optical Filters

The bandpass profile of a thin film optical filter shifts with temperature because the optical thickness of the thin film layers change with temperature. If all layers are expanded by a certain percentage, the entire bandpass profile shifts in wavelength by the same proportion. Two material properties are responsible for the change in optical thickness with temperature; the thermal expansion and the refractive index temperature coefficient. The former refers to the change in physical thickness of the thin film layer, and the latter determines the change in refractive index with temperature. For most thin film materials both of these changes are positive with increasing temperature.

From a theoretical point of view, the temperature dependence of an optical filter is straightforwardly calculated, provided the thermo-optical properties of the filter materials are known. However, thermo-optical properties of thin films are scarcely found in the lit-

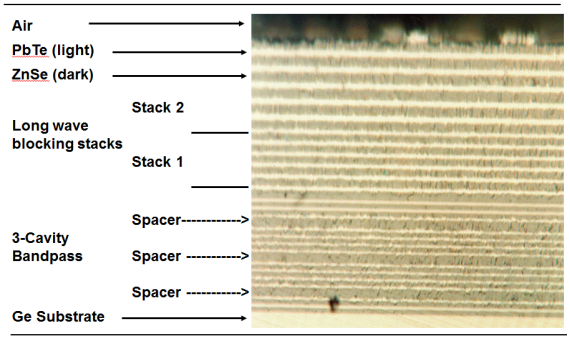

Figure 4.3: Enlarged photo of a 3-cavity PbTe/ZnSe optical bandpass filter deposited on Germanium. The picture was produced by IML, University of Reading.

erature, especially for mid-infrared thin film materials at elevated temperatures (> 25 °C). Moreover, thermo-optical data of embedded thin films in multilayer structures appears to be completely absent, although they are recognised to exhibit different thermo-optical properties compared to the same materials in bulk form [48].

The particular shortage of thermo-optical data for mid-infrared materials above room temperature are presumably related to the fact that infrared optical filters are historically used at cryogenic temperatures which have been required because infrared detectors were troubled by thermal noise [49]. However, the field of mid-infrared sensing is changing [50] and optical filters are increasingly employed in non-cooled optical systems [51], and from this, the demand for temperature-invariant mid-infrared optical filters is arising.

At IML they have specialised in handling a rather unique thin film material; Lead Telluride (PbTe). It is a material with several interesting qualities from a filter designers point of view. Amongst these is the high refractive index value of 5.5 at 300 K which is one of the highest known for infrared thin film materials, and means that high index contrast between the layers can be achieved which is helpful as it reduces the number of layers needed in an optical filter [47]. Another celebrated feature is the high wavelength position of the short wave semiconductor absorption edge at 3.5 μm at 300 K which assures effective blocking of radiation below this wavelength, hence removes the obligation for this to be provided by interference effects. Although it does, at the same time, restrict the wavelength range to > 3.5 μm for use above 300 K, the absorption edge of PbTe delivers a welcome simplification for optical bandpass filters for mid-infrared NO_X measurements.

However, PbTe possesses yet another unique feature, in that it has a negative change in refractive index with increasing temperature. As this temperature coefficient exceeds the positive thermal expansion of the material, the optical thickness of the PbTe films actually contracts with increasing temperature. The negative thermo-optical expansion may be utilised to compensate for the positive thermo-optical expansion of the alternate material in the multilayer, and this enables the construction of temperature-invariant optical bandpass filters. This was first reported a long time ago by IML in 1976 [52] and picked up by others [53]. Over the last couple of decades IML has made frequent use of this material for

mid-infrared bandpass filters, and is therefore in possession of a large historic repository of PbTe-containing bandpass filters, with ZnSe as a preferred alternate thin film material.

However, by the time of my visit, no one had performed a systematic study to unveil the design-dependence of the desired temperature-invariant property. Altogether, the arising demand for temperature invariant optical filters, the lack of systematic studies in the literature, as well as the available amount of manufactured bandpass filters of various filter designs, impelled us to undertake a systematic study of the temperature dependence of mid-infrared optical bandpass filters containing PbTe and ZnSe. This evolved into a fruitful cooperation between myself and Gary Hawkins and resulted in two journal papers (Paper 2 and Paper 3) while a third paper is in preparation. The papers have been summarised in the beginning of the thesis and are attached in full lengths in Appendix B and C. In Paper 2, we managed to relate the temperature behaviour of the bandpass filters to their multilayer design and obtained good agreement between a developed empirical model and the measured centre wavelength shifts with temperature, which ultimately enabled us to produce a set of temperature invariant bandpass filters across a wide wavelength range (4-10 μm). Paper 3 used the model and the data from Paper 2 to extract the thermo-optical expansion coefficients of embedded thin film PbTe and ZnSe for three different wavelengths in the temperature range 20-160 °C. These two papers are considered to contribute with a major step toward the control of temperature invariance. The two papers are to be followed up by an extension of the

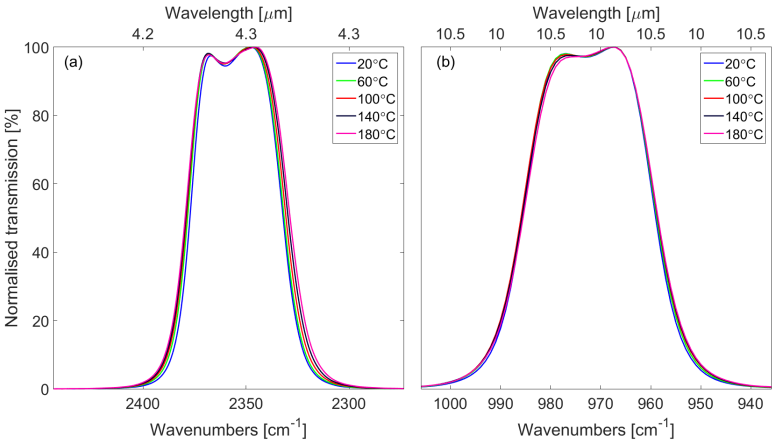

Figure 4.4: Example of two bandpass filters with good centre wavelength stability. The widths of the filters increase with increasing temperature because the ratio of refractive indices increases, an issue which is most pronounced at short wavelengths (a) compared to longer wavelengths (b). The limits of the wavenumber ranges of the two plots are chosen such that they extend over the same relative frequency range (ν/ν_c) with ν_c being the centre wavenumber.

study to include the thin film material PbS which, as PbTe, has a negative thermo-optical expansion coefficient. Establishing the thermo-optical properties of PbS opens up for de-

signing and realising temperature invariant bandpass filters with other bandpass widths than those obtainable with PbTe/ZnSe.

In the published papers, temperature invariance has been almost exclusively used to refer to the centre wavelength of the filter. However for a spectroscopist trying to separate closely separated absorption lines, it is really the filter edges that are of importance. Since the width of a filter is determined by the ratio of the refractive indices of the thin film materials then with one refractive index increasing and the other decreasing, the width of the filter is bound to change. For this reason, a centre wavelength that is invariant to temperature does not necessarily imply that the filter profile is completely stable. For the realised filters with stable centre frequencies over a broad infrared wavelength range, this was mainly an issue for the shortest centre wavelengths. The issue is illustrated in Figure 4.4 showing two narrow bandpass filters claimed in Paper 2 to exhibit good centre wavelength stability. However, with the derived thermo-optical material coefficients at hand, it is equally possible to tailor one of the filter edges to be invariant to temperature, rather than the centre wavenumber. The papers are further restricted to the study of narrow bandpass filters but the determined thermo-optical properties are expected to be valid for edge filters as well, although this has yet to be demonstrated. In fact, edge filters might be used to construct bandpass profiles which are truly invariant also at short wavelengths, since the width of such filters are not determined by the ratio of the refractive indices.

4.4 Discussion

This chapter has discussed optical interference filters. However, thin film optics is a vast research field and many important subjects have been omitted here such as fabrication methods. I have made an attempt to gather from what I have learned about thin film filters over the course of this PhD project, the information that would have been good to know when I began building the filter optimisation routine.

4.5 Conclusion

This chapter has presented an introduction to thin film interference filters from the perspective of a spectroscopist. It has given a brief introduction to the underlying physical principle and explained why bandpass filters are divided into broad and narrow bandpass filters. The properties specific to each of the two types of filters have been discussed which is useful knowledge when searching for an optimum filter setup through spectral simulations. Finally, the critical issue of wavelength shift with temperature of bandpass filters has been thoroughly investigated and this has led to the derivation of the thermo-optical expansion coefficient of embedded thin films of PbTe and ZnSe.

CHAPTER 5

High Pressure and High Temperature CO_2 Measurements

Following Danfoss IXA's withdrawal from the HTF project and change of measurement technique for exhaust gas measurement of NO_X away from NDIR, my PhD project was redirected to focus on CO_2 and H_2O measurements in high pressure applications. Danfoss IXA was undertaking the development of a CO_2 and H_2O sensor for exhaust gas measurements on-board ships, with exhaust gas recirculation (EGR) as a particular application. In EGR which was introduced in Chapter 1, NO_X is reduced by mixing exhaust gas into the intake air with the purpose of reducing the oxygen level. This effectively lowers the combustion temperature which determines the rate in which NO_X is produced. However, the combustion temperature further depends on the humidity level in the intake air and thus both CO_2 and H_2O are requested for EGR measurements in pressures up to 6 bar. In return the temperatures are low (25-80°C). CO_2 and H_2O distinguish themselves from other emission gases by their high abundance and their strong absorption of infrared radiation. The two gases represent the best investigated molecules within infrared spectroscopy, particularly at atmospheric conditions while they have also been subject to intensive studies at higher temperatures to which a specific database [54] is devoted. However, elevated pressure studies are less numerous. In connection with this development, I carried out a concept study into potential technologies for simultaneous measurement of CO_2 and H_2O at elevated pressures within some contraints set by Danfoss IXA regarding physical design as well as budget. However, since the investigations are of sensitive character to Danfoss IXA, the details are not included in this thesis.

Around the same time at Risø, Postdoc Caspar Christiansen was constructing a gas cell for high temperature and high pressure investigations targeted for spectroscopic CO_2 measurements. This formed part of a larger research project named Radiade [55] concerned with the modelling of radiative transfer in combustion processes in diesel engines on ships. The infrared emission from CO_2 is an important contributor to radiative transfer in combustion because of its strong absorption lines and high abundance. Its contribution grows with temperature and becomes increasingly important for larger diesel engines, in particular large ship engines. However the combustion takes place at very high pressures under conditions where the emission spectrum of CO_2 has never been measured.

Caspar Christiansen was just starting the validation process of the high temperature and

high pressure gas cell as the project finished. As I had given up the originally planned experimental verification of the NDIR NO_2 measurements, the gas cell provided an opportunity for me to gain experimental spectroscopic experience within the PhD-project, as well as gaining access to measure absorption spectra for CO_2 at EGR pressures. I therefore took over the work with the cell. This was a work that entailed many surprises and several adjustments to the measurement setup as well as measurement procedure. One thing that we encountered was that when the pressure in the cell was increased, this caused the temperature in the cell to drop. The three temperature set points along the length of the cell therefore had to be adjusted, and this by very different amounts. The increase from 1 to 100 bar with nitrogen in the cell, resulted in a need for adjusting the set points with +20 K on average at 1000 K. The effect on temperature meant that temperature stability and uniformity over the cell had to be reestablished at the target temperature, and this made every measurement at high pressure very time consuming, particularly since there appeared to be no clear pattern in the way the set points had to be adjusted at various temperatures and pressures. In contrast, it did not seem to affect the set points whether the cell was filled with nitrogen or a 5 % CO_2 calibration gas. Eventually, we were able to validate the cell against previously reported high temperature and high pressure measurements, and to report the first measured absorption cross section of CO_2 at 1000 K and 100 bar. The results of the gas cell work was presented in a paper which has been submitted to Journal of Quantitative Spectroscopy and Radiative Transfer. The paper is summarised in the beginning of the thesis and the full paper is available in Appendix D.

Thesis Conclusion

This PhD study originated in the attempt of measuring NO_X with NDIR spectroscopy in moist exhaust gas. This is scientifically interesting but perhaps to ambitious to be suited for an industrial PhD project which ultimately has to obey commercial interests of the company. However, despite some turbulence created in connection with Danfoss IXA's justified decision to abandon NDIR as a technology for their NO_X exhaust gas sensor about 14 months into the PhD project, I managed to achieve a good partial result within NDIR exhaust gas measurements of NO_2. A set of optical bandpass filters were realised within narrow tolerances, predicting good humidity compensating properties.

The project had a change of direction toward research in the temperature behaviour of optical bandpass filters. A major result of this work was the extraction of the thermo-optical expansion coefficients of embedded PbTe and ZnSe thin films, an accomplishment which is considered an important step in future production of temperature invariant optical filters for the mid-infrared region. This work was presented in two journal papers which I consider to be the main scientific outcome of this PhD project.

The very theoretical focus of this PhD study, was supplemented by experimental work on high pressure and high temperature gas cell measurements of CO_2 absorption. This work concluded in a paper presenting the first measured CO_2 absorption cross section spectrum at 1000 K and 100 bar, and the results will hopefully contribute to an enhanced understanding of combustion processes in large ship engines, including the formation of NO_X .

APPENDIX $\mathfrak{A}$

Paper 1: In Optics Humidity Compensation in NDIR Exhaust Gas Measurements of NO_2

In Optics Humidity Compensation in NDIR Exhaust Gas Measurements of NO_2

Thomine Stolberg-Rohr[1,2], Rainer Buchner[3], Sønnik Clausen[2], Jens Møller Jensen[4], Allan Skouboe[1], Gary Hawkins[5], René Skov Hansen[1]

[1] *Danfoss IXA A/S, Vejle, Denmark.*
[2] *DTU Chemical Engineering, Technical University of Denmark, Kgs. Lyngby, Denmark.*
[3] *Independent consultant, Lübeck, Germany.*
[4] *AAMS Aarhus School of Marine and Technical Engineering, Denmark*
[5] *Infrared Multilayer Laboratory, School of System Engineering, The University of Reading, Reading, United Kingdom*

thomine@danfoss.com

Abstract: NDIR is proposed for monitoring of air pollutants emitted by ship engines. Careful optical filtering overcomes the challenge of optical detection of NO_2 in humid exhaust gas, despite spectroscopic overlap with the water vapour band.

OCIS codes: 300.0300 , 300.6340.

1. Motivation

Exhaust gas emission from ships is a major contributor to global air pollution and subject to increasing international attention [1]. There is a demand for continuous monitoring of the contents of the pollutants NO, NO_2, and SO_2 directly in the exhaust pipe from the ship engine. All of these gases are infrared active but suffer from spectral overlap with water vapour. Exhaust gas contains a vast amount of water vapour from the burning of hydrocarbons, in addition to being hot and chemically aggressive. This makes optical sensing advantageous as it allows decoupling of the detector element from the harsh exhaust gas. Non dispersive infrared (NDIR) spectroscopy is attractive for exhaust gas sensing because it is an optical method without moving parts and further an affordable alternative to more complex spectroscopic devices. Yet, NDIR, in general, does not posses the ability to discriminate NO and NO_2 from water vapour [2]. The present paper presents an analysis of a special filter arrangement that targets this issue for NO_2 by balancing out the water vapour signal in two simultaneous measurements with two accurately designed and manufactured optical filters.

2. Measurement Principle

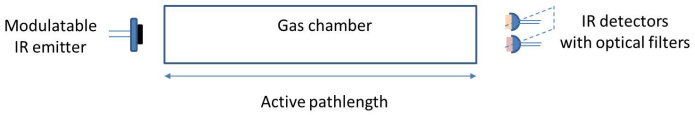

Fig. 1. Sketch of typical NDIR set-up. Spectral selection takes place through optical filters. Collimating optics not shown.

Fig. 1 shows a basic set-up of a typical NDIR measurement, comprising a modulatable IR emitter, a number of detectors with optical filters for spectral selection. Light travels from the emitter to the detector through a gas chamber where the gas molecules absorb light at different wavelengths, which reveals the concentrations of the abundant gases, if properly detected. The transmission through the gas ensemble is described by Beer-Lambert's law,

$$T = \prod_{\text{gas}} \exp(-\sigma_{\tilde{\nu}}^{\text{gas}} L\, N^{\text{gas}}) \,, \tag{1}$$

where L is the pathlength, $\sigma_{\tilde{\nu}}^{\text{gas}}$ is the absorption cross section and N^{gas} is the number concentration. The superscript, "'gas"', indicates that the transmission through the gas ensemble is the product of the transmission through all individual gas species. The following analysis is based on thermopile detectors, which measure the total incident light

integrated over all wavelengths and return a voltage given by

$$u = \int_0^\infty \mathrm{d}\nu \;\; s_\nu \; T_\nu^{\mathrm{Optics}} \; T_\nu^{\mathrm{Filter}} \; I_\nu^{\mathrm{Source}} \prod_{\mathrm{gas}} \exp(-\sigma_\nu^{\mathrm{gas}} L \, N^{\mathrm{gas}}) + U^{\mathrm{BG}}, \tag{2}$$

where ν is the wavenumber ($\frac{1}{\lambda}$), s_ν is the wavelength dependent detector sensitivity. T_ν^{optics} is the transmission through the collimating optics, T_ν^{Filter} is the transmission through the optical filter in front of the particular detector. The background therm U^{BG} covers both the self-radiation of the thermopile detector and the background radiation from the hot gas, particles and surfaces in the optical path. The background contributions can be effectively eliminated by modulating the source intensity, I_ν^{Source}, with modulation amplitude, m, at frequency ω. The voltage amplitude measured on the thermopile, $A_{\mathrm{Filter}}^{\omega}$ becomes

$$A_{\mathrm{Filter}}^{\omega} = m \; s \; I^{\mathrm{Source}} \;\; T^{\mathrm{Optics}} \int_{\nu_1}^{\nu_2} \mathrm{d}\nu \prod_{\mathrm{gas}} \exp(-\sigma_\nu^{\mathrm{gas}} L \, N^{\mathrm{gas}}) \; , \tag{3}$$

where, in order to obtain analytical results, the approximation has been made that s, I^{Source}, and T^{optics} can be considered constant over the wavelength range defined by the filter. The filter is included as having a rectangular bandpass shape with cut-on frequency ν_1 and cut off ν_2. The ratio between the voltage amplitudes of two detector channels equipped with two different optical filters which we shall denote suspect (sus) and reference (ref),

$$R = \frac{A_{\mathrm{sus}}^{\omega}}{A_{\mathrm{ref}}^{\omega}} = \underbrace{\frac{s_{\mathrm{sus}} I_{\mathrm{sus}}^{\mathrm{Source}} \;\; T_{\mathrm{sus}}^{\mathrm{Optics}}}{s_{\mathrm{ref}} I_{\mathrm{ref}}^{\mathrm{Source}} \;\; T_{\mathrm{ref}}^{\mathrm{Optics}}}}_{\text{Calibration parameter},\beta} \underbrace{\frac{\int_{\nu_1^{\mathrm{sus}}}^{\nu_2^{\mathrm{sus}}} \mathrm{d}\nu \prod_{\mathrm{gas}} \exp(-\sigma_\nu^{\mathrm{gas}} L \, N^{\mathrm{gas}})}{\int_{\nu_1^{\mathrm{ref}}}^{\nu_2^{\mathrm{ref}}} \mathrm{d}\nu \prod_{\mathrm{gas}} \exp(-\sigma_\nu^{\mathrm{gas}} L \, N^{\mathrm{gas}})}}_{\text{Function of gas concentrations, } f(N_1,N_2,..)} , \tag{4}$$

can be divided into a product of a calibration constant, β, and a function of the gas concentrations which we wish to measure. The ratio of voltage amplitudes, R, has the advantage of being immune to any changes that are equally affecting both the suspect and the reference channel, e.g. a uniform intensity change. For weak absorptions the integration over the absorption cross section can further be approximated to an average absorption cross section in the range defined by the filter, $\bar{\sigma}_{\mathrm{filter}}^{\mathrm{gas}}$,

$$R = \beta \frac{\exp(-\bar{\sigma}_{\mathrm{sus}}^{\mathrm{NO_2}} L \, N^{\mathrm{NO_2}}) \exp(-\bar{\sigma}_{\mathrm{sus}}^{\mathrm{H_2O}} L \, N^{\mathrm{H_2O}})}{\exp(-\bar{\sigma}_{\mathrm{ref}}^{\mathrm{NO_2}} L \, N^{\mathrm{NO_2}}) \exp(-\bar{\sigma}_{\mathrm{ref}}^{\mathrm{H_2O}} L \, N^{\mathrm{H_2O}})} = \beta \exp\left(-(\bar{\sigma}_{\mathrm{sus}}^{\mathrm{NO_2}} - \bar{\sigma}_{\mathrm{ref}}^{\mathrm{NO_2}}) L \, N^{\mathrm{NO_2}} \;\; -(\bar{\sigma}_{\mathrm{sus}}^{\mathrm{H_2O}} - \bar{\sigma}_{\mathrm{ref}}^{\mathrm{H_2O}}) L \, N^{\mathrm{H_2O}} \right) \tag{5}$$

for the case where NO_2 and H_2O are the only abundant gases absorbing in the selected spectral range. From (5) we get the logical result that the humidity contribution cancels out if a filter setup is chosen such that the average humidity absorption in the two ranges are equal, i.e., $\bar{\sigma}_{\mathrm{sus}}^{\mathrm{H_2O}} = \bar{\sigma}_{\mathrm{ref}}^{\mathrm{H_2O}}$, while $\bar{\sigma}_{\mathrm{sus}}^{\mathrm{NO_2}} - \bar{\sigma}_{\mathrm{ref}}^{\mathrm{NO_2}}$ should be maximized.

3. Results

The approximations performed to arrive at (5) are useful for the analytical analysis. Using a full numerical analysis and a high resolution spectral database [3], we can deal with detailed spectral features, saturation, and non-rectangular bandpass filters and search for a filter pair that maximizes the relation

$$\chi = \frac{\frac{\partial R}{\partial N^{\mathrm{NO_2}}}}{\frac{\partial R}{\partial N^{\mathrm{H_2O}}}} \; . \tag{6}$$

However, the main challenge lies not in finding the solution that maximizes χ, but to find one that is stable within the manufacturing tolerances of the optical filters. More precisely, to define and incorporate tolerances of the filters into the optimization of χ. In fact, filter-manufacturing capabilities become the decisive factor in the realisation of an NDIR NO_2 sensor. Optical filter manufacturers are reluctant to promise edge position tolerances below 0.5 % and also the bandpass shape is difficult to predict exactly. Bandpass filters are often optimized with focus on a rectangular appearance but in the given context a predictable bandpass shape supersedes rectangularity in importance, and the development of the optical filters and the numerical optimization of χ are greatly interdependent. Optical filters were designed and manufactured at Reading University, Infrared Multilayer Laboratory, and the transmission curves are shown in Fig. 2 together with transmission spectrum of 10 %VMR H_2O and 300 ppm NO_2. The common long wave

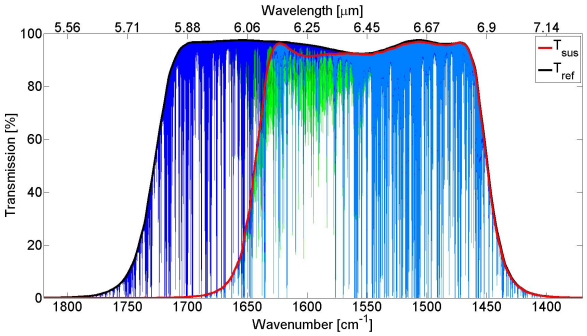

Fig. 2. Transmission curves of manufactured suspect and reference filters together with gas transmission spectra showing 300 ppm of NO_2 (green) hidden in 10 %VMR H_2O (blue) at 350 °C, 1 bar and $L = 40$ cm.

cut-off has clear manufacturing advantages, enabling filters with identical edges and thereby reducing the number of uncertainties that affect the water outbalancing performance. The resulting thermopile voltage amplitudes are shown in Figure 3 for a fixed optical setup (MEMS emitter with max temperature 750 °C, thermopile detector, $L = 40$ cm and two MgF_2 lenses constituting the collimating optics). The filter setup has greatly reduced the cross sensitivity to H_2O

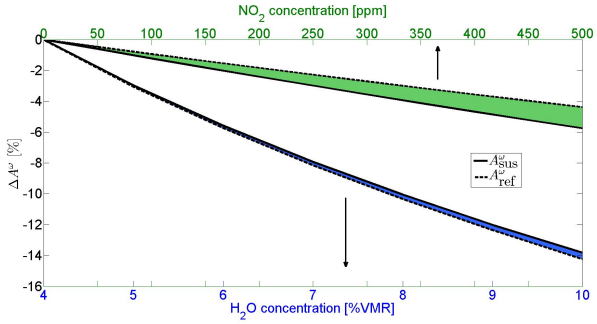

Fig. 3. Resulting voltage amplitudes of the two filters shown in Fig. 2 for varying H_2O and NO_2 concentrations. The split between suspect and reference voltage indicate the effective NO_2 (green shaded area $\propto \bar{\sigma}_{\mathrm{sus}}^{\mathrm{NO_2}} - \bar{\sigma}_{\mathrm{ref}}^{\mathrm{NO_2}}$) and H_2O (blue shaded area $\propto \bar{\sigma}_{\mathrm{sus}}^{\mathrm{H_2O}} - \bar{\sigma}_{\mathrm{ref}}^{\mathrm{H_2O}}$) signal.

to a degree where it can be compensated through a simultaneous H_2O measurement. A change of 0.1%VMR H_2O corresponds to a change of up to 3.2 ppm NO_2. Other cross sensitivities exist, amongst these are source temperature drift, which is a general concern in NDIR [4]. For the given setup we have a cross sensitivity to NO_2 of 1.5 ppm / °C. The filter setup has been limited to the short wavelength side to avoid cross sensitivity to formaldehyde which might be present in exhaust gas from ships. In conclusion, an optical filter pair has been successfully manufactured to a precision that allows optical balancing of the water vapour signal in an NO_2 measurement in wet exhaust gas.

References

1. International Maritime Organization. *NOx Technical Code* (2008), RESOLUTION MEPC.177(58).
2. A. J. de Castro, J. Meneses, S. Briz, F. Lpez *Nondispersive infrared monitoring of NO emissions in exhaust gases of vehicles*, Rev. Sci. Instrum. 70, 3156 (1999).
3. L. S. Rothman, et. al. *The HITRAN 2008 molecular spectroscopic database* , "J. Quant. Spectrosc. Radiat. Transfer" 110 (2009) 533-572.
4. J. Y. Wong, R. L. Anderson, *Non-Dispersive Infrared Gas Measurement* (Ifsa Publishing, 2012).

APPENDIX 𝔅

Paper 2: Spectral design of temperature-invariant narrow bandpass filters for the mid-infrared

Spectral design of temperature-invariant narrow bandpass filters for the mid-infrared

Thomine Stolberg-Rohr[2] Gary J. Hawkins[1,*]

[1]*The University of Reading, Infrared Multilayer Laboratory, School of Systems Engineering,Whiteknights, Reading, Berkshire, RG6 6AY, England, UK*
[2]*Technical University of Denmark (DTU), DTU Chemical Engineering, Søltofts Plads 229, 2800 Kgs. Lyngby, Denmark*
[*]*g.j.hawkins@reading.ac.uk*

Abstract: The ability of narrow bandpass filters to discriminate wavelengths between closely-separated gas absorption lines is crucial in many areas of infrared spectroscopy. As improvements to the sensitivity of infrared detectors enables operation in uncontrolled high-temperature environments, this imposes demands on the explicit bandpass design to provide temperature-invariant behavior. The unique negative temperature coefficient ($dn/dT<0$) of Lead-based (Pb) salts, in combination with dielectric materials enable bandpass filters with exclusive immunity to shifts in wavelength with temperature. This paper presents the results of an investigation into the interdependence between multilayer bandpass design and optical materials together with a review on invariance at elevated temperatures.

OCIS codes: (350.2460) Filters, interference; (300.6340) Spectroscopy, infrared; (310.0310) Thin films; (310.4165) Multilayer design; (310.6188) Spectral properties; (310.6860) Thin films, optical properties.

References and links

1. G. J. Hawkins, R. Hunneman, R. Sherwood, and B. M. Barrett, "Infrared filters and coatings for the High Resolution Dynamics Limb Sounder (6-18 microm)," Appl. Opt. **39**(28), 5221–5230 (2000).
2. T. Katsumata, R. Nishimura, K. Yamaoka, E. G. Camargo, T. Morishita, K. Ueno, S. Tokuo, H. Goto, and N. Kuze, "Uncooled InGaSb photovoltaic infrared detectors for gas sensing," J. Cryst. Growth **378**, 611–613 (2013).
3. A. G. U. Perera, P. V. V. Jayaweera, G. Ariyawansa, S. G. Matsik, K. Tennakone, M. Buchanan, H. C. Liu, X. H. Su, and P. Bhattacharya, "Room temperature nano- and microstructured photon detectors," Microelectron. J. **40**(3), 507–511 (2009).
4. P. V. V. Jayaweera, S. G. Matsik, A. G. U. Perera, H. C. Liu, M. Buchanan, and Z. R. Wasilewski, "Uncooled infrared detectors for 3-5 um and beyond," Appl. Phys. Lett. **93**(2), 021105 (2008).
5. T. Stolberg-Rohr, R. Buchner, S. Clausen, J. M. Jensen, A. Skouboe, G. Hawkins, and R. S. Hansen, "In optics humidity compensation in NDIR exhaust gas measurements of NO2," in *Advanced Photonics Conference*, OSA Technical Digest (online) (Optical Society of America, 2014), paper SeTh1C.3.
6. R. Mark, D. Morand, and S. Waldstein, "Temperature control of the bandpass of an interference filter," Appl. Opt. **9**(10), 2305–2310 (1970).
7. C. S. Evans, R. Hunneman, and J. S. Seeley, "Optical thickness changes in freshly deposited layers of lead telluride," J. Phys. D. **9**(2), 321–328 (1976).
8. J. S. Seeley, R. Hunneman, and A. Whatley, "Temperature-invariant and other narrow band IR filters containing PbTe, 4-20 um," Proc. SPIE **246**, 83–96 (1980).
9. C. R. Pidgeon and S. D. Smith, "Resolving power of multilayer filters in nonparallel light," J. Opt. Soc. Am. **54**(12), 1459–1466 (1964).
10. J. S. Seeley, G. J. Hawkins, and R. Hunneman, "Performance model for cooled IR filters," J. Phys. D **21**(10S), S71–S74 (1988).
11. B. Li, S. Y. Zhang, J. C. Jiang, D. Q. Liu, and F. S. Zhang, "Recent progress in improving low-temperature stability of infrared thin-film interference filters," Opt. Express **13**(17), 6376–6380 (2005).
12. J. P. Borgogno, F. Flory, P. Roche, B. Schmitt, G. Albrand, E. Pelletier, and H. A. Macleod, "Refractive index and inhomogeneity of thin films," Appl. Opt. **23**(20), 3567–3570 (1984).
13. H. Rafla-Yuan, B. P. Hichwa, and T. H. Allen, "Noncontact method for measuring coefficient of linear thermal expansion of thin films," J. Vac. Sci. Technol. A **16**(5), 3119–3122 (1998).

#226657 - $15.00 USD Received 10 Nov 2014; revised 19 Dec 2014; accepted 22 Dec 2014; published 9 Jan 2015

14. K. Zhang, J. Seeley, R. Hunneman, and G. Hawkins, "Optical and semiconductor properties of lead telluride coatings," Proc. SPIE **1125**, 45–52 (1989).
15. C. Jacobs, "Dielectric square bandpass design," Appl. Opt. **20**(6), 1039–1042 (1981).
16. H. A. Macleod, *Thin-Film Optical Filters, Fourth Edition* (CRC Press, 2010).
17. H. Takashashi, "Temperature stability of thin-film narrow-bandpass filters produced by ion-assisted deposition," Appl. Opt. **34**(4), 667–675 (1995).
18. P. Baumeister, "Methods of altering the characteristics of a multilayer stack," J. Opt. Soc. Am. **52**(10), 1149–1152 (1962).
19. P. Klocek, *Handbook of Infrared Materials* (Marcel Dekker, Inc., 1991).
20. C.-H. Su, S. Feth, and S. L. Lehoczky, "Thermal expansion coefficient of ZnSe crystal between 17 and 1080°C by interferometry," Mater. Lett. **63**(17), 1475–1477 (2009).
21. Yu. I. Ravich, B. A. Efimova, and I. A. Smirnov, *Semiconducting Lead Chalcogenides* (Plenum Press, 1970).
22. Y.-H. Yen, L.-X. Zhu, W.-D. Zhang, F.-S. Zhang, and S.-Y. Wang, "Study of PbTe optical coatings," Appl. Opt. **23**(20), 3597–3601 (1984).
23. R. Dalven, "A review of the semiconductor properties of PbTe, PbSe, PbS and PbO," Infrared Phys. **9**(4), 141–184 (1969).
24. E. Palik, *Handbook of Optical Constants of Solids* (Acedemic Press, 1985).
25. R. A. Feldman, D. Horowitz, and R. M. Waxler, "Refractive properties of infrared window materials" *in Proceedings of Laser induced damage in optical materials*, (SPIE, 1977).
26. R. J. Harris, G. T. Johnston, G. A. Kepple, P. C. Krok, and H. Mukai, "Infrared thermooptic coefficient measurement of polycrystalline ZnSe, ZnS, CdTe, CaF(2), and BaF(2), single crystal KCI, and TI-20 glass," Appl. Opt. **16**(2), 436–438 (1977).
27. H. W. Icenogle, B. C. Platt, and W. L. Wolfe, "Refractive indexes and temperature coefficients of germanium and silicon," Appl. Opt. **15**(10), 2348–2351 (1976).
28. B. J. Frey, D. B. Leviton, and T. J. Madison, "Temperature-dependent refractive index of silicon and germanium," Proc. SPIE **6273**, 62732J (2006).
29. J. Thornton, "Absorption characteristics of low-resistivity germanium," Proc. SPIE **1112**, 94–98 (1989).
30. S.-H. Kim and C. K. Hwangbo, "Derivation of the center-wavelength shift of narrow-bandpass filters under temperature change," Opt. Express **12**(23), 5634–5639 (2004).
31. H. Takashashi, "Temperature stability of thin-film narrow-bandpass filters produced by ion-assisted deposition," Appl. Opt. **34**(4), 667–675 (1995).
32. G. J. Hawkins, R. E. Sherwood, B. M. Barrett, M. Wallace, H. J. B. Orr, K. Matthews, and S. Bisht, "High-performance infrared narrow-bandpass filters for the Indian National Satellite System meteorological instrument (INSAT-3D)," Appl. Opt. **47**(13), 2346–2356 (2008).
33. J. E. Murphy-Morris and S. W. Hinkal, "GOES Sounder Overview," Proc. SPIE **2812**, 174–181 (1996).
34. G. J. Hawkins, R. E. Sherwood, K. Djotni, P. M. Coppo, H. Höhnemann, and F. Belli, "Cooled infrared filters and dichroics for the Sea and Land Surface Temperature Radiometer," Appl. Opt. **52**(10), 2125–2135 (2013).
35. E. Ritter, "Properties of optical film materials," Appl. Opt. **20**(1), 21–25 (1981).
36. H. A. Macleod, "Microstructure of optical thin films," Proc. SPIE **325**, 21–28 (1982).

1. Introduction

It is a fundamental behavior of thin film narrow bandpass filters to exhibit large displacements of center wavelength with temperature. This attribute can be utilized for selective wavelength tuning of optical filters by controlling the temperature. However, it is generally a cause of concern to spectroscopists employing bandpass filters to discriminate between different molecular species with spectrally overlapping absorption signatures. Historically, infrared optical filters have been integrated in cooled and temperature stabilized detecting systems with working temperatures far-below the filter manufacturing conditions [1]. Therefore the filter designer has always needed to take wavelength shifts with temperature into consideration. However, current infrared technology is advancing toward the use of uncooled detectors [2–4] in which optical filters are increasingly embedded in infrared devices required to operate at room temperature and above in uncontrolled temperature environments [5]. In the absence of active temperature control, temperature-invariant optical bandpass filters are of increasing demand.

The inherent temperature shift in center wavelength of the narrow bandpass filter is governed by the temperature-dependency between paired optical properties of the multilayers, viz. the refractive index, index contrast and the physical thicknesses. These properties determine the integrated optical thickness of the bandpass coating, which defines the center wavelength. For most materials, the temperature coefficients of these paired materials are

#226657 - $15.00 USD Received 10 Nov 2014; revised 19 Dec 2014; accepted 22 Dec 2014; published 9 Jan 2015

positive, leading to optically thicker coating layers with increasing temperature, and subsequent displacement of center wavelength toward longer wavelength [6].

Lead Telluride (PbTe) is an exceptional semiconductor material that has been investigated extensively for mid-infrared optical filters for many years [7]. It is an extraordinary material for the following reasons [8]; the high refractive index when used with an appropriate low-index dielectric results in one of the highest practical known index contrasts (n_H/n_L) to achieve a prescribed spectral filtering function with the minimum number of layers and maximize throughput. The refractive index is one of the highest known of usable infrared layer materials with values of n ~5.5 at 300K rising to ~6.0 at 80K, (i.e. refractive index decreasing with increasing temperature), this contrast provides a high effective index (n*), broadening the multilayer stop-band width and reducing spectral shift caused by inclined illumination [9]. Additionally for mid-infrared wavelengths PbTe provides continuous short-wavelength blocking by photo-absorption to ~3.2μm, further than all other commonly used evaporation materials due to the long-wave position of its semiconductor edge. Upon cooling the semiconductor absorption edge shifts to longer wavelengths (and hence shorter-wavelengths on heating) as a function of the anomalous increase in bandgap (PbTe ≅ + 4.2×10^{-4} eV K-1), common with all Pb-salts (PbTe, PbSe, PbS). For intrinsic PbTe at temperatures between 100K and 450K, the bandgap increases from ≅ 0.25 eV to ≅ 0.4 eV. This change produces a short-wavelength shift proportional to the inverse of the temperature moving from ~5.0 to 3.2 μm [10]. The optical dispersion properties of PbTe layer material are further strongly defined by the electronic carrier concentration, and departure from stoichiometry.

In this paper we pay specific attention to the negative dn/dT of PbTe as it presents unique possibilities to achieve temperature-invariant bandpass filter behavior. Figure 1 illustrates the principle of minimizing the net wavelength displacement with temperature using paired materials of PbTe and ZnSe. The blue and green curves show simulated bandpass displacements with wavelength due to the changes in thermal coefficient with increasing temperature applied singularly to each material. The red curves show the resultant net bandpass wavelength displacement across the 20-160 °C temperature range.

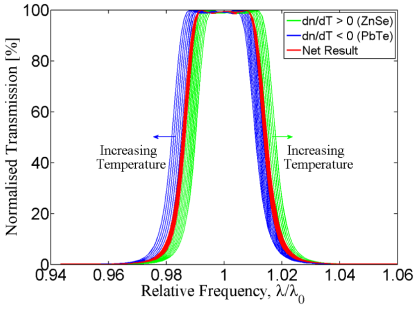

Fig. 1. Opposing optical layer properties resulting in wavelength immunity of PbTe/ZnSe narrow bandpass filter with temperature.

The application of temperature-invariant properties to infrared narrow bandpass filter design has been known for a number of decades, particularly with PbTe and ZnS paired materials discussed and demonstrated formerly for Fabry-Perot (FP) single-cavity and two-cavity Double Half-Wave (DHW) designs [8,11]. However, a systematic investigation of the design dependence of contemporary temperature-invariant three-cavity Triple Half-Wave (THW) filters has never been presented, and the rationale of temperature-invariant properties has remained undisclosed.

#226657 - $15.00 USD Received 10 Nov 2014; revised 19 Dec 2014; accepted 22 Dec 2014; published 9 Jan 2015

From a theoretical perspective, predicting the temperature and spectral response for a given thin film multilayer is straightforward, providing the material temperature coefficients of expansion and dispersion are well-known. However, this is generally not the case for thin films embedded in a multilayer operating in an environment above room temperature. Thin films generally possess different optical, thermal and mechanical properties compared to the isotropic bulk form [12,13]. Often bulk properties are insufficient to accurately predict the resulting thermal behavior of the thin film multilayer. Despite efforts in establishing these thin film opto-mechanical properties over many years [13,14], the knowledge of particular thermal expansion coefficients with temperature for any embedded thin film is still exceedingly sparse, if not unattainable. In Section 5 we review the available data for thermal expansion coefficients as well as the thermal dispersion coefficients of the two important layer materials for mid-infrared wavelengths, PbTe and ZnSe. Focusing solely on the optical and mechanical properties of these two materials reduces the complexity of this study as it limits the number of available design permutations, simplifying the characterization of the interdependence between multilayer design and temperature invariance. We are further directing this work towards elevated temperatures across the range 20-160 °C. Within this temperature range we expect temperature invariance to become of particular importance in future infrared detection. However, the design methods described in this paper are not constrained by these two materials or wavelength ranges, but applicable to other Pb salts (PbSe, PbS) in combination with other II-VI dielectric materials and temperatures.

2. Modelling procedure

The work reported here was divided into the following procedure; firstly to establish a knowledge database by conducting a literature survey to gather published knowledge of the refractive index temperature coefficient $\left(\frac{1}{n}\frac{dn}{dT}\right)$ (referred to as temperature dispersion coefficient, β_n), and the linear thermal expansion coefficient (α_L) for PbTe and ZnSe, in both thin film and bulk form. Secondly, to calculate the center wavelength temperature dependence $\left(\frac{1}{\lambda}\frac{d\lambda}{dT}\right)$ for various multilayer design arrangements of narrow bandpass filters based on published material properties. This is followed by predictions of temperature-dependence tested against measurements of thermal behavior from a repository of manufactured optical filters. This approach discloses whether the reported material properties can correctly predict the temperature response of manufactured filters, particularly, where some properties are in disagreement. Finally, to categorize multilayer designs with temperature-invariant behavior based on design bandwidth, cavity thickness order, and number of inter-cavity reflector layers. Here we present a simple model that successfully predicts the temperature response of manufactured bandpass filters.

3. Bandpass filter design

The narrow bandpass filters designed and manufactured for this investigation have comprised well-established triple half-wave (3-cavity) resonant multilayer designs using the high index contrast from the IV-VI lead telluride (PbTe, $n \approx 5.5$) semiconductor alternately paired with II-VI zinc selenide (ZnSe, $n \approx 2.4$) dielectric. This generic bandpass design approach has been fully described historically by Jacobs [15] with the advantage of deploying integral quarter-wave (λ/4) inter-cavity reflector stacks, use of multiple half-wave (λ/2, λ, 3λ/2 etc.) cavity thicknesses, and inclusion of antireflection matching periods between the equivalent bandpass core index and surrounding media. The nomenclature described in this paper assigns cavity thickness to either integral full-wave (λ) designation, comprising 2:2:2 to represent the half-wave order of the three cavities (i.e. 4:4:4 represents 3 cavities, each of λ thickness).

#226657 - $15.00 USD Received 10 Nov 2014; revised 19 Dec 2014; accepted 22 Dec 2014; published 9 Jan 2015

These generic bandpass filter designs have been deployed extensively throughout many former spaceflight filter missions, as described in Section 8, with advantages and compromise between spectral discrimination and manufacturability. As the energy grasp due to squareness of the bandpass shape improves with the number of cavities, the total number of index-matched paired layers and thickness of the multilayer also increases. In addition to this, the narrower the filter bandwidth is required to be, higher order thickness cavities are needed and larger number of inter-cavity layers necessary to match internal reflectivity from the cavities. As the bandwidth further reduces with increasing thickness, transmission losses due to absorption and multiple beaming rise sharply, which together with an increased sensitivity of bandpass shape to layer thickness errors, the perceived spectral advantage of improved bandpass shape diminishes with increased number of cavities. For mid-infrared wavelengths all of these factors mitigate against increasing designs beyond 3-cavities, often the result of limiting accuracy from *in situ* optical thickness monitoring during deposition.

4. Temperature-dependence theory

The center wavelength (λ_0) positioning of a bandpass filter is determined by the optical thicknesses of the coating layers. The optical thickness (δ) of a thin film layer is proportional to the product of the material properties; refractive index n, and physical thickness l, $(2\pi nl\cos\theta)/\lambda$. Since both of these properties change with temperature, λ_0 becomes temperature-dependent. However, the thin film materials comprising the multilayer stack will not change optical thickness equally or in the same direction, i.e. alternate layers become optically thinner with temperature, whilst the remaining layers optically thicken. Based on performance simulations through the multilayer characteristic matrix algorithm [10,16] (programmed through FTG FilmStar® proprietary thin film design software), we have determined that the contribution to the wavelength shift can be evaluated incrementally as discrete layers throughout the multilayer, with a design specific weighting factor assigning a sensitivity to individual layers opposing each other The center wavelength shift can thus be described by the following equation.

$$\frac{\mathrm{d}}{\mathrm{d}T}\frac{\lambda_0}{\lambda}=\sum_{m=1}^{q}s_m\frac{1}{\delta_m}\frac{\mathrm{d}\delta_m}{\mathrm{d}T}$$

where m is the layer number, q is the total number of layers, and s_m is a design specific layer sensitivity factor For a dual material filter this simplifies to;

$$\frac{\mathrm{d}}{\mathrm{d}T}\frac{\lambda_0}{\lambda}=s_L\frac{1}{\delta_L}\frac{\mathrm{d}\delta_L}{\mathrm{d}T}+s_H\frac{1}{\delta_H}\frac{\mathrm{d}\delta_H}{\mathrm{d}T} \tag{1}$$

where L and H are low and high refractive index materials respectively. The material weighting factors (S_L) and (S_H) are determined by the multilayer design. The temperature coefficient of the optical thickness relates to the temperature coefficients α_L and β_n;

$$\frac{1}{\delta}\frac{\mathrm{d}\delta}{\mathrm{d}T}=\frac{1}{nl}\frac{\mathrm{d}}{\mathrm{d}T}nl=\frac{1}{nl}\left(l\frac{\mathrm{d}n}{\mathrm{d}T}+n\frac{\mathrm{d}l}{\mathrm{d}T}\right)=\frac{1}{n}\frac{\mathrm{d}n}{\mathrm{d}T}+\frac{1}{l}\frac{\mathrm{d}l}{\mathrm{d}T}=\beta_n+\alpha_L$$

where we have recognized $\frac{1}{l}\frac{\mathrm{d}l}{\mathrm{d}T}$ as the linear thermal expansion coefficient, α_L, and $\frac{1}{n}\frac{\mathrm{d}n}{\mathrm{d}T}$ as the linear temperature dispersion coefficient β_n. Furthermore, we can now define the linear

#226657 - $15.00 USD Received 10 Nov 2014; revised 19 Dec 2014; accepted 22 Dec 2014; published 9 Jan 2015

thermo-optical expansion coefficient as $\gamma_L \equiv \frac{1}{\delta}\frac{\mathrm{d}\delta}{\mathrm{d}T} = \beta_n + \alpha_L$. Equation (1) can thus be substituted;

$$\frac{d}{dT}\frac{\lambda_0}{\lambda} = s_L\,\gamma^L + s_H\,\gamma^H = s_L\left(\beta_n^L + \alpha_L^L\right) + s_H\left(\beta_n^H + \alpha_L^H\right) \qquad (2)$$

For most conventional dielectric thin film materials, both β_n and α_L are positive values and thus λ_0 shifts toward longer wavelengths with increasing temperature. From Eq. (2) we see that in order to produce a filter with low temperature dependence, there are two different ways to proceed. One approach is to choose specific materials with minimal values of β_n and α_L. This approach is undertaken by Takashashi [17] where attention is directed to achieving bulk-like crystal properties of the thin film structure by ion-assisted deposition. A very different approach is to look for a special material having at least one negative temperature coefficient such that Eq. (2) by choice of multilayer design adds up to zero. This is the approach pursued by Seeley [8] and Li [11], as well as in this work. The enabling material is PbTe because of its negative change in refractive index ($dn/dT<0$) with increasing temperature. Li *et al* takes control of the negative coefficient by doping PbTe with Ge. Their focus is to target temperature-invariance to a specific temperature range. In this work we are not controlling temperature invariance, we are explaining and predicting how the multilayer design determines the temperature behavior of the bandpass filter. It is, however, our intention that the work presented here will contribute to gaining control over temperature invariance of optical filters in the future.

Equation (2) shows how the temperature response of the bandpass is determined by the temperature coefficients β_n and α_L of the constituent materials. The dependence on the multilayer design has been concealed in the sensitivity weighting factors, S_L and S_H which can be conveniently calculated by the help of multilayer design software. Mathematically demonstrated by Baumeister [18], the impact of a change in optical thickness of a single layer depends on the position inside the multilayer stack. The method was applied by Seeley [8] to determine; i) the cavity layer in a Fabry-Perot bandpass filter is significantly more sensitive to thickness changes than the surrounding layers, ii) a double half-wave cavity is twice as sensitive to thickness changes as a single half-wave cavity, and iii) the reflector layers adjacent to the cavity are three times more sensitive than the successive inter-cavity layers. According to these findings, the order of the filter should have major influence on the temperature response of the bandpass, as confirmed and demonstrated by the spectral measurement data presented in Section 8.

5. Optical material properties

The optical properties of thin films are well-known to deviate from the isotropic bulk material properties, often due to crystal morphology structure or film porosity resulting from reduced packing density (ρ), yet measurements of optical properties of thin films are usually made on exposed single layer films deposited on a substrate. Embedded thin films within a multilayer are likely to further possess optical properties between bulk and single film values, yet they are not easily measured and only derived by assumptions.

5.1 Linear thermal expansion coefficient (α_L)

The linear thermal expansion coefficient (α_L) is well-established for most bulk materials and can be found in reference literature handbook sources such as Klocek [19]. However, recently α_L for bulk ZnSe was measured using Fabry-Perot interferometry designed for elevated

#226657 - $15.00 USD Received 10 Nov 2014; revised 19 Dec 2014; accepted 22 Dec 2014; published 9 Jan 2015

temperatures (17-1080 °C) from which values of α_L were reported by Su *et al* [20] to be 35% below handbook values at room temperature. The authors do not comment on this deviation. Rafla-Yuan *et al* [14] measured ZnSe α_L for 1.7 μm thick single thin film by ellipsometry from which values significantly larger than bulk properties were reported, as illustrated in Fig. 2. The authors explain the large discrepancy from bulk as a result of film packing density, stress, and thermal expansion mismatch between film and substrate. As their reported values are measured on single exposed thin films, they cannot be expected to apply for the embedded thin film in an interference multilayer. In fact, the thin film values from Rafla-Yuan vary so radically with temperature that they can be instantly excluded from our study due to the corresponding center wavelength displacement being considerably larger than observed in measurements. Further, the increase with temperature would mean that the displacement rate, $\Delta\lambda_0$ /°C should increase with temperature, which is also not observed. This maintains the continued use of existing bulk ZnSe literature data.

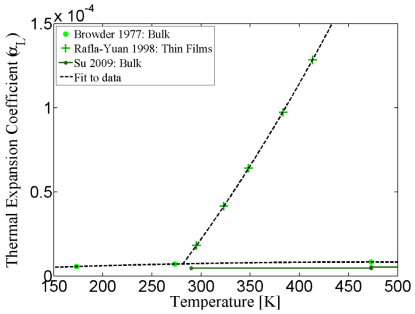

Fig. 2. Comparison of reported thermal expansion of thin film and bulk values of ZnSe

Linear thermal expansion data for thin film PbTe is not reported in the literature, but is available for bulk PbTe. Ravich *et al* [21] reports the thermal expansion coefficient across a 25-320 K temperature range, with a stable plateau value above 200 K of 2.0 x10^{-5} K^{-1} with increasing temperature. Figure 3 shows the bulk α_L values in the multilayer simulations for both ZnSe and PbTe.

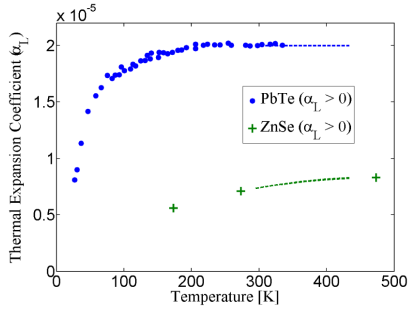

Fig. 3. Thermal expansion coefficients of bulk material for PbTe and ZnSe. (Dashed lines indicate the values deployed in the simulations).

#226657 - $15.00 USD Received 10 Nov 2014; revised 19 Dec 2014; accepted 22 Dec 2014; published 9 Jan 2015

5.2 Optical dispersion temperature coefficient (β_n)

The exact refractive index of PbTe is known to depend on the properties of evaporable material composition [22]. Zhang *et al* [14] characterized the refractive index of tellurium-enriched PbTe thin films with a dispersive shape showing similar generic properties to PbTe bulk material. The refractive index was determined for incremental temperatures between 45K and 463K across the complete inter-band transparent spectral range, (i.e. between electronic and multiphonon lattice absorption edges). The refractive index derived from spectral measurement is slightly lower than handbook bulk values [23,24] at corresponding temperatures as shown in Fig. 4.

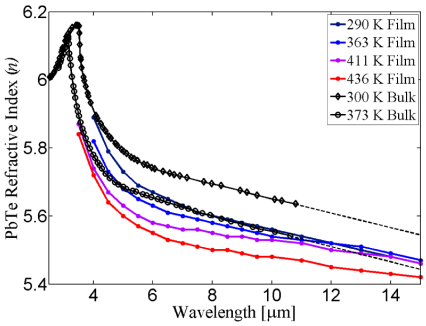

Fig. 4. Overlay of dispersion curves for bulk and thin film PbTe material (17-163K).

The temperature derivative (i.e. the temperature dispersion coefficient, $\beta_n = \frac{1}{n}\frac{\mathrm{d}n}{\mathrm{d}T}$), however shows a significant difference between thin film coating and bulk index as shown in Fig. 5. The bulk values were calculated by interpolation between the two fitted dispersion curves at 300 K and 373 K in Fig. 4. Interpolation between two values reveals no information about a possible temperature-dependence of β_n^{PbTe}. Thus a constant value is assumed and used in the simulation across the 20-160 °C temperature range. For the thin film PbTe material there are four different temperatures in our range of interest. However, the thin film data in Fig. 4 shows a very non-linear temperature behavior which is not in agreement with our measurements on manufactured filters as these generally exhibit smooth wavelength displacements with temperature. The stated uncertainty of the thin film data is 0.01 to 0.05 which may contribute significantly to the apparent nonlinear behavior. Instead we have chosen to use only the data sets at 290 K and 436 K which are separated by values greater than the uncertainty. As in the bulk case, two points per wavelength remain from which we derive a temperature independent value for thin film β_n^{PbTe}. This value is significantly smaller than the corresponding bulk value and leads to a very different prediction of the center wavelength shift. Figure 5 further shows a mean value between bulk and thin film as this turns out to be in best agreement with the measured spectral data, which we shall discuss in Section 8.

#226657 - $15.00 USD Received 10 Nov 2014; revised 19 Dec 2014; accepted 22 Dec 2014; published 9 Jan 2015

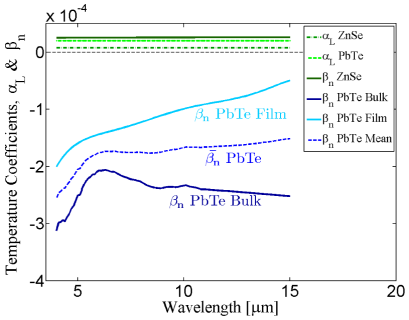

Fig. 5. Dispersion temperature coefficient ($\boldsymbol{\beta_n}$) and linear thermal expansion coefficient ($\boldsymbol{\alpha_L}$) of PbTe and ZnSe.

For ZnSe material we were unable to find any published data on thin film properties so also here it was necessary to use bulk properties. Feldman *et al* [25] measured *dn*/*dT* for a number of bulk infrared materials, including ZnSe, for a range of temperatures and a few different wavelengths. The values found for ZnSe in this work are 15% larger than corresponding measurements reported by Harris *et al* [26] earlier in the same year. This deviation made the authors repeat the measurement using a different method from which they obtained comparable results to their first measurements. Furthermore, Feldman *et al* generally found good agreement with other studies for their measurements of other materials. Based on this we choose to use the Feldman results from [25] for β_n^{ZnSe}, from which it is noted that the wavelength-dependence of the ZnSe temperature dispersion coefficient is very small compared with PbTe.

The results in Fig. 5 summarizes our review of the optical properties for PbTe and ZnSe, from which constants are presented in Table 1. For α_L^{ZnSe}, α_L^{PbTe}, and β_n^{ZnSe} we have not located any useful reference data in thin film form, thus have applied bulk properties to the model. Conversely, for β_n^{PbTe} we have acquired both thin film and bulk data. From the results illustrated in Fig. 5 together with interpretation of Eq. (2), it is evident that owing to the magnitude of β_n^{PbTe}, this temperature coefficient contributes the largest impact on center wavelength displacement.

Table 1. Results of review of mid-infrared optical properties of ZnSe and PbTe (20 - 160 °C)

Coefficient	Bulk	Thin film	Data Origin
α_L^{ZnSe}	+ 0.77 x 10^{-5} K^{-1}	-	[20]
α_L^{PbTe}	+ 2.0 x 10^{-5} K^{-1}	-	[22]
β_n^{ZnSe}	+ 2.6 x 10^{-5} K^{-1}	-	[26]
β_n^{PbTe} (at 10 μm)	- 23 x 10^{-5} K^{-1} *	–9.9x10^{-5} K^{-1} *	[24] [15]

6. Bandpass simulations

Using the derived temperature coefficients described above, calculations to simulate the influence of elevated temperature on various bandpass designs, wavelengths, and cavity thicknesses were performed through conventional multilayer calculation theory. Example of simulation results for a generic multilayer design with different cavity thicknesses are shown in Fig. 6. This common multilayer bandpass design located at 4 and 10 μm comprises

#226657 - $15.00 USD Received 10 Nov 2014; revised 19 Dec 2014; accepted 22 Dec 2014; published 9 Jan 2015

incremental half-wave thickness for the three cavities. The simulations shown are performed using bulk properties for α_L^{ZnSe}, β_n^{ZnSe} & α_L^{PbTe} and with a mean coefficient between bulk and thin film properties for β_n^{PbTe}.

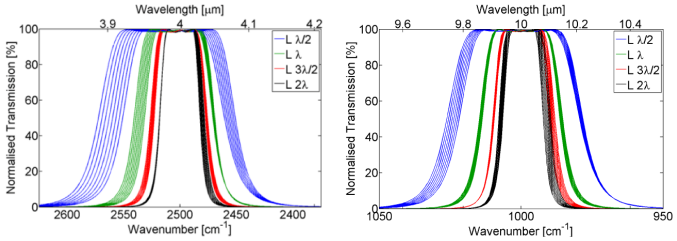

Fig. 6. Simulated temperature response of four different thickness-order L-cavity ZnSe/PbTe bandpass filters at 4 and 10 µm. Each color covers the range 20-160°C in steps of 20°C

The bandpass simulations in Fig. 6 reveal an asymmetry of edge positions with temperature wavelength shift. This asymmetric displacement is the result of bandwidth broadening that occurs simultaneously with opposing index coefficients. As the bandwidth is determined by the index contrast between the paired layer materials (n_H/n_L), the opposing temperature coefficients maintain wavelength stability, however the reduced index contrast broadens the bandwidth ($\Delta\lambda/\lambda_0$). As a result, the opposing edges are displaced differently. For the purpose of discriminating between absorption lines, the edges are actually of greater interest than the center wavelength displacement. From the perspective of center wavelength displacement the 3λ/2 cavity thickness is very good, but in mid-infrared spectroscopy the 2λ or even λ-cavity filters might be preferred because of the stable edges on the short-wave and long-wave side, respectively. However, for the purpose of this paper we will continue to discuss center wavelength displacement to comply with existing literature on temperature invariance. Yet, since edge-wavelength shift is of equal importance, this information together with center wavelength shifts obtained from the repository of manufactured bandpass filters is included in the summarized results in Table 3. For each design wavelength and cavity order, the center wavelength shift with temperature is determined. The resulting values are illustrated as circles in Fig. 7 along with the calculations from Eq. (2) using the weighting factors given in Table 2. Evidently, using Eq. (2), the optical properties, and the design dependent weighting factors, temperature-invariance can be predicted without need of performing any multilayer calculations.

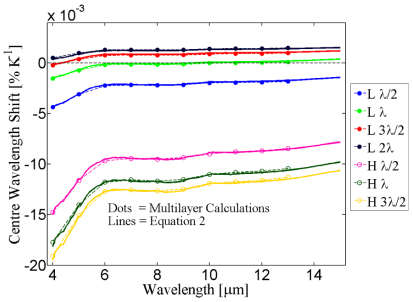

Fig. 7. Overlay of simulated center wavelength displacement (circles), and displacement predicted from Eq. (2).

#226657 - $15.00 USD Received 10 Nov 2014; revised 19 Dec 2014; accepted 22 Dec 2014; published 9 Jan 2015

Table 2. Weight factors for Eq. (2).

Sensitivity factors	L –Cavity λ/2	L –Cavity λ	L –Cavity 3λ/2	L –Cavity 2λ	H –Cavity λ/2	H –Cavity λ	H – Cavity 3λ/2
S_L [%]	71	82	87	89	32	20	15
S_H [%]	29	18	13	11	68	80	85

Results from Fig. 7 indicate that achievement of wavelength invariance at elevated temperature across the 6-13 μm range using ZnSe and PbTe materials, is best performed with a cavity thickness of λ. This however subsequently infers compromise between optimal temperature-invariance and desired bandwidth. At wavelengths below 6 μm higher orders are necessary to achieve wavelength-invariance.

7. Substrate temperature influence

Thin film dielectric multilayers deposited on germanium are perhaps the most extensively used material combination in the context of cooled mid-infrared filtering applications. It exhibits low absorption across the 2-12 μm wavelength range with a bandgap of ~0.67 eV at ambient temperature. At elevated temperatures however, standard optical grade material is known to be subject to substantial absorption losses throughout the infrared waveband due to the increased number of thermally generated free carrier holes. Germanium is hence generally not suited as a substrate for high temperature applications. The temperature-dependent refractive index of germanium has been reported by Icenogle *et al* [27] and Frey *et al* [28] for operation in cooled temperature environments. Spectral measurements of many infrared substrate materials at elevated temperatures are however sparse. Thornton [29] measured Ge transmission in increments up to 150 °C for two differing resistivity samples across the 7-15 μm range. The II-VI dielectrics, however, remain transparent for temperatures up to at least 200 °C. Figure 8 shows temperature measurements of uncoated optical windows of ZnSe, ZnS and Ge for temperatures between 20 – 200 °C.

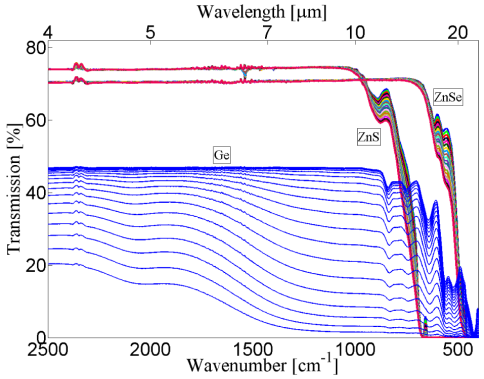

Fig. 8. Measured transmission of 4 mm thick ZnS, ZnSe and Ge uncoated substrate materials at temperatures from 20 °C to 200 °C at 20 °C increments.

A substantial number of the spectral measurements presented in this paper are deposited on germanium, particularly as the filters were designed for cryogenic operation. This, however, does not compromise the validity of the elevated temperature-invariance comparison. We have compared filters of similar multilayer design deposited on different substrates, as shown in Fig. 9, from which the substrate material is observed to influence wavelength shift to a lesser degree than the variations stemming from uncertainties in

#226657 - $15.00 USD Received 10 Nov 2014; revised 19 Dec 2014; accepted 22 Dec 2014; published 9 Jan 2015

manufacture. The two filters at 4 μm were further fabricated within the same deposition, which meant that one of the filters had to suffer from poor optical matching, distorting the bandpass shape, but showing no influence to the temperature behavior. From this we conclude that both substrate material as well as optical matching is inconsequential to the temperature variations of the bandpass filter. This is in agreement with theoretical findings in [30].Whilst we consider this a significant and important conclusion, it might not be transferable to other material arrangements and wavelengths, since in [31] thermal expansion of the substrate is found to have great influence on the center wavelength temperature stability of TiO_2/SiO_2 bandpass filters. In Section 9 we further investigate the influence of layer thickness errors which show that this also is without significant impact on the temperature-dependence.

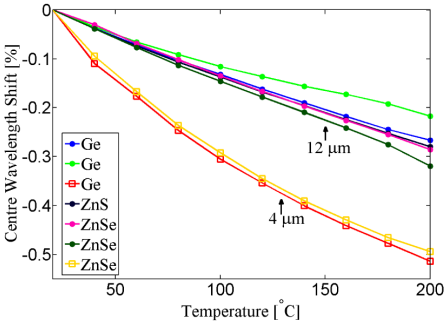

Fig. 9. Center wavelength shift for several filters of similar bandpass design deposited on differing substrate materials at wavelengths of 4 μm and 12 μm.

8. Comparison with manufactured filters

In order to validate the accuracy of predicted results from the temperature-invariance model presented in Fig. 7, spectral measurements at incremental temperature were performed on a historic repository of narrow bandpass filters originating from Earth observing spaceflight radiometer instruments. This library of filters represents a wide cross-section of generic multilayer bandpass design types and wavelengths, comprising both L- and H-spaced integral thickness cavities, differing cavity thickness orders, operating temperature requirements and center wavelength positioning.

Narrow bandpass filters from two missions; the NASA Aura mission High Resolution Dynamics Limb Sounder (HIRDLS) [1] and Indian Space Research Organization (ISRO) INSAT-3D [32] atmospheric sounder instruments comprised a wide range of differing bandpass designs containing 3-cavity triple half-wave (THW) low-index (L) cavity layers with differing thickness orders using alternate ZnSe and PbTe layers deposited on Germanium (Ge) optical substrates. The HIRDLS instrument bandpass filters were deployed in the focal plane detector array of this limb-viewing infrared radiometer which was designed for high resolution monitoring of global stratospheric and mesospheric temperatures and chemical species in the atmosphere at wavelengths between 6 and 18 μm. These filters were designed for high precision of spectral placement (typically, $\Delta\lambda_0 = \pm 1$ cm^{-1}), and located at an intermediate focus of the instrument, thermostatically controlled at 301K to provide the waveband definition through a low converging (*f*/5.5-*f*/7) conical illumination.

Bandpass filters manufactured for the INSAT-3D sounder instrument were developed for high resolution monitoring of temperature and trace species in the atmospheric region between the troposphere and stratosphere over the Bay of Bengal and Arabian Sea. These filters comprised precision L-cavity narrow bandpass designs between 1% and 6% full width half max (FWHM) to isolate wavelengths over the long-wave (LWIR 12-15 μm) and mid-

#226657 - $15.00 USD Received 10 Nov 2014; revised 19 Dec 2014; accepted 22 Dec 2014; published 9 Jan 2015

wave (MWIR 6.5-11 μm) spectral regions. These filters were designed to operate at a temperature of 210K in a collimated *f*/10 parallel beam. Similar wavebands of the INSAT-3D sounder are also deployed on the NOAA GOES geostationary satellite [33].

A third mission, comprising the Sea and Land Surface Temperature Radiometer (SLSTR) [34] is an instrument designed to provide climate data of global sea and land temperatures within the framework of the ESA Copernicus programme for the European polar orbiting Sentinel-3 satellite mission. The design of mid-IR narrow bandpass filters at 10.85 and 12.0 μm in this case employed high-index (H) cavity layer material to minimize wavelength shifts due to conical illumination (*f*/1.46) at the focal plane of the instrument. As one of the highest known refractive index materials, the use of PbTe cavity material provides a high effective index (n^*) to reduce sensitivity to non-parallel illumination ($d\lambda/d\theta$), however PbTe also possesses a large temperature coefficient ($d\lambda/dT$) when deployed in cavities, negating any temperature-invariant properties. This filter set provides a suitable cross-reference of an alternative generic bandpass design type to validate the wavelength displacement properties of the presented invariance model.

Further L-cavity narrow bandpass filters with temperature-invariant properties were manufactured at wavelengths of 4.3, 7.7, 10.3 and 12.1 μm deposited on CVD Zinc Sulphide (Multispectral ZnS, Cleartran®), Zinc Selenide (ZnSe) and Germanium (Ge) optical substrate materials. These items were manufactured with center wavelengths and spectral properties for industrial gas monitoring.

Table 3. Analysis of mean temperature shift from a repository of manufactured bandpass filters (20–120 °C) (Deposited on Ge, ZnSe and ZnS optical substrates).

Generic 3-Cavity Design	Bandpass Center at 20 °C (λ_0, μm)	Bandwidth (FWHM,%)	SW Edge Thermal Shift ($10^{-3\%}$ K^{-1})	Center λ_0 Thermal Shift ($10^{-3\%}$ K^{-1})	σ* for Center λ_0 Thermal Shift ($10^{-3\%}$ K^{-1})	LW Edge Thermal Shift ($10^{-3\%}$ K^{-1})
H - 2:2:2	10.47	10.49	–10.51	–8.87	-	–7.04
H - 2:2:2	11.77	8.42	–9.55	–8.35	-	–7.05
L - 2:2:2	4.3	3.8	–4.6	–3.2	0.5	–1.7
L - 2:2:2	11.4	4.5	–3.0	–1.9	-	–0.6
L - 2:2:2	12.1	4.4	–2.3	–1.6	0.2	–0.9
L - 2:2:2	15.8	4.3	–2.7	–1.8	0.0	–0.8
L - 2:2:2	17.5	3.9	–2.5	–1.7	-	–0.8
L - 2:4:2	7.3	3.2	–1.4	–0.4	0.6	0.7
L - 4:2:2	6.9	3.9	–2.2	–1.3	0.2	–0.3
L - 4:4:4	4.3	2.6	–1.8	–0.9	0.2	0.1
L - 4:4:4	7.6	2.8	–0.8	–0.1	0.2	0.5
L - 4:4:4	10.3	2.6	–0.5	–0.0	0.1	0.5
L - 4:4:4	12.1	2.8	–0.8	–0.5	0.6	–0.1
L - 4:4:4	16.4	2.9	–0.3	0.3	-	0.8
L - 4:6:4	13.6	2.3	0.4	0.8	0.1	1.2
L - 4:6:6	14.7	2.2	0.5	1.0	-	1.4
L - 6:4:6	9.7	2.4	0.0	0.6	-	1.2
L – 6:6:6	4.2	1.9	–0.6	0.1	0.1	0.8
L – 6:6:6	12.0	2.0	0.5	0.9	0.0	1.3
L – 6:6:6	14.2	2.0	0.8	1.1	0.3	1.5
L - 6:8:8	8.3	1.7	1.1	1.5	-	2.0

*Sample Standard deviation. Range of sample quantities are between 2 and 5 filter elements.

A total of 45 manufactured narrow bandpass 3-cavity filters with ZnSe and PbTe layer materials were systematically measured across a range of elevated temperatures between 20 and 200 °C at 20 °C intervals. Figure 10 shows a representative center wavelength displacement with temperature at 4 and 12 μm. The shift is observed to deviate from linearity

#226657 - $15.00 USD Received 10 Nov 2014; revised 19 Dec 2014; accepted 22 Dec 2014; published 9 Jan 2015

with a tendency to reduce at the higher temperatures. The effects of non-linear wavelength shift at the higher temperatures has implied an irregular material property from which our data analysis was constrained to a 100 °C range between 20 °C and 120 °C. By comparison, simulations predict a linear shift with temperature as there is no temperature-dependence in the coefficients. Based on this truncated measurement data, we determined the center wavelength and 50% FWHM edge shifts for all the filters measured. The obtained shift values are given in Table 3 and shown in Fig. 10 as a function of cavity order, viz. the one property with the most significant effect on temperature invariance. Spectral measurements and visual inspection from the elevated temperature excursions showed no evidence of either residual thermal hysteresis or mechanical damage, with exception of a single filter which experienced environmental deterioration at 200 °C. All filters showed a linear or slowly declining displacement with temperature up to 120 °C.

The influence of deposition temperature has not been specifically evaluated in this work, but is further known to affect both the sticking coefficient [35] and environmental properties due to the influence on packing density and microstructural morphology of the condensed films [36].

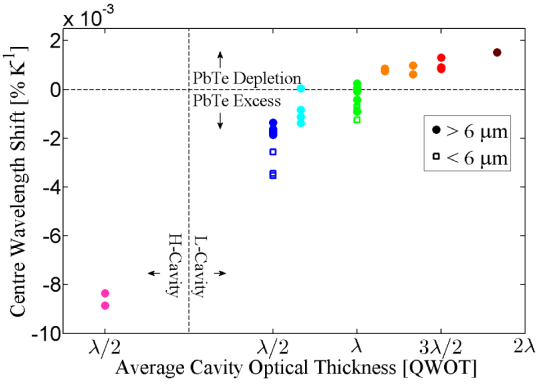

Fig. 10. Center wavelength shift of manufactured filters with cavity thickness and temperature (20-120 °C).

In Fig. 10 there is a clear relationship between cavity order and center wavelength displacement. The positive wavelength shift of high L-cavity orders represents a deficiency of PbTe material. Reducing the order, and associated increasing filter bandwidth, reduces the relative amount of ZnSe in the multilayer and the positive wavelength shift is decreased accordingly, continuing until the balance is opposed from which the filters begin to shift to shorter wavelengths with increasing temperature. For an H-cavity filter, the excess of PbTe leads to a negative center wavelength displacement worse than the typical positive center wavelength displacement of 0.005 [% K^{-1}] described in reference literature sources [16]. With the appropriate material balance several infrared filters with center wavelength displacements below 0.00015 [% K^{-1}] were realized over a wide wavelength range. Some examples of these are shown in Fig. 11, where the measured transmission profiles are illustrated for filter temperatures between 20 and 200 °C in steps of 20 °C.

#226657 - $15.00 USD Received 10 Nov 2014; revised 19 Dec 2014; accepted 22 Dec 2014; published 9 Jan 2015

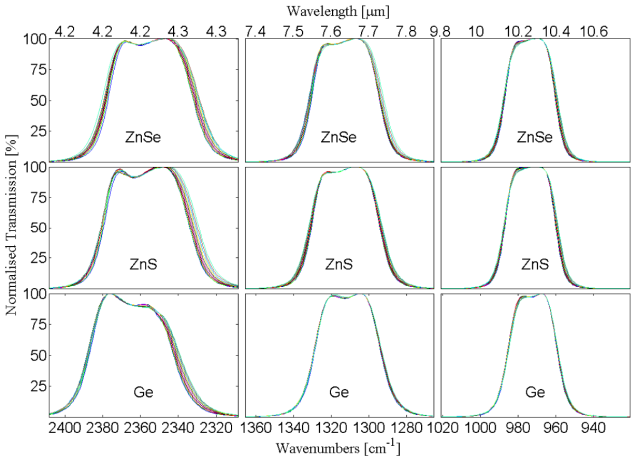

Fig. 11. Example normalized transmission measurements of 3-cavity bandpass filters at 4.2 μm, 7.6 and 10.3 μm showing temperature invariance in the range 20 - 200 °C.

In Fig. 12 the measured bandpass center shifts for all 45 filters are shown as a function of wavelength, together with the theoretically predicted temperature response based on bulk values of α_L and β_n for ZnSe, and for PbTe using bulk values of α_L and an average between bulk and thin film values for β_n. Whilst the true value for the embedded films are expected to be somewhere between the values of single thin film and bulk, there is no reason to assume that the value is exactly the average. However, the simple average leads to a remarkably good correspondence with experimental data. Using either thin film data or bulk data for PbTe (β_n) demonstrated, on the contrary, very poor agreement with the measured shifts (not shown). Figure 12 shows that within the confines of paired PbTe/ZnSe 3-cavity narrow bandpass filter materials, an optimal temperature-invariance can be achieved, but is restricted to a specific bandwidth. To gain more degrees of freedom and enabling temperature-invariant bandpass behavior at intermediate bandwidths, a third material might be included.

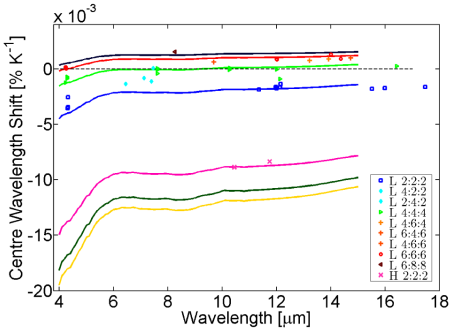

Fig. 12. Predicted center wavelength shift (lines) compared with measured wavelength shifts (symbols).

#226657 - $15.00 USD Received 10 Nov 2014; revised 19 Dec 2014; accepted 22 Dec 2014; published 9 Jan 2015

9. Layer thickness errors

Thickness errors of thin film layers are of key concern to the bandpass manufacture, particularly for matched accuracy of the cavities, as they compromise perfection of band shape, bandwidth and wavelength positioning. The fabricated filters to which we compare our simulations, inevitably all contain some degree of thickness error. We have investigated the degree to which such errors affect the wavelength displacement with temperature. Figure 13 shows simulated temperature variations of the bandpass transmission profile of a PbTe/ZnSe bandpass filter without thickness error, together with the same multilayer design but containing thickness errors introduced to the center cavity, particularly as this is known to be a dominating layer which is most sensitive to deviations [8]. No consequence was found of thickness errors on the wavelength displacement with temperature, even for gross thickness errors added to the most sensitive cavity layers. It should be noted, that introducing errors to adjacent cavities or inter-cavity reflector layers lead to the same conclusion. This analysis verifies that our simulations may be compared with fabricated filters without concerns regarding the influence of thickness errors. In fact, the results further allow us to make the general conclusion that thickness perfection plays no role in influencing temperature-invariance.

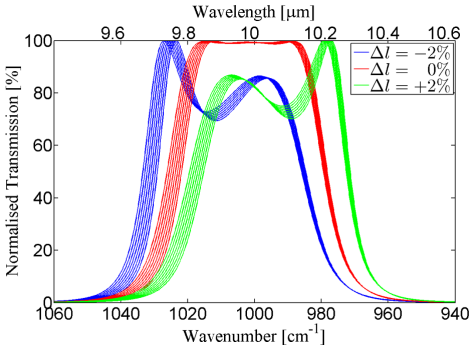

Fig. 13. Temperature variations of a multilayer design without thickness errors, and with gross thickness error applied to the center cavity of ± 2%.

10. Conclusions

A systematic investigation into the interdependence between multilayer bandpass design, optical materials, and wavelength properties of narrow bandpass filters has been presented. It has been shown that the temperature coefficients of bulk material are insufficient in predicting temperature wavelength dependence of narrow PbTe/ZnSe based bandpass filters. A set of material temperature properties that are able to describe the temperature wavelength behavior of PbTe/ZnSe narrow bandpass filters in good agreement with a historic repository of narrow bandpass filters were given for the temperature range 20-120 °C and the wavelength range 4-15 μm. It was shown experimentally that the cavity order determines the temperature wavelength behavior, implying that temperature invariance for a two-material filter is restricted to certain bandwidths. Mixed cavity orders can be used to tune the wavelength displacement to a desired value. Temperature measurements of different substrate temperature behavior at elevated temperature has been presented and it was shown that substrate material had insignificant influence on temperature invariance of these specific narrow band filters, even with increasing substrate absorption and optically mismatched thin film design. Finally,

#226657 - $15.00 USD Received 10 Nov 2014; revised 19 Dec 2014; accepted 22 Dec 2014; published 9 Jan 2015

it was shown that layer thickness errors neither contribute nor compromise the temperature-invariance sensitivity of the narrow bandpass filter design.

Acknowledgments

The authors thank colleagues at Schlumberger Cambridge Research for discussions and grateful support under contract reference QU-RDU-01274-C, together with the loan of a spectrometer accessory for high-temperature measurements. Thomine Stolberg-Rohr is a visiting industrial PhD student from Danfoss IXA A/S and her work is supported by the Danish Agency of Science, Technology and Innovation (DASTI). Thanks also to Richard Sherwood and Karim Djotni at the University of Reading for their assistance with spectral measurements and thin film depositions, which is gratefully acknowledged.

#226657 - $15.00 USD Received 10 Nov 2014; revised 19 Dec 2014; accepted 22 Dec 2014; published 9 Jan 2015

APPENDIX C

Paper 3: Determination of the embedded thermo-optical expansion coefficients of PbTe and ZnSe thin film infrared multilayers

Determination of the embedded thermo-optical expansion coefficients of PbTe and ZnSe thin film infrared multilayers

Gary J. Hawkins[1,*] and Thomine Stolberg-Rohr[2]

[1]*The University of Reading, Infrared Multilayer Laboratory, School of System Engineering, Whiteknights, Reading, Berkshire, RG6 6AY England, UK*

[2]*Technical University of Denmark (DTU), DTU Chemical Engineering, Søltofts Plads 229, 2800 Kgs. Lyngby, Denmark*

[*]*g.j.hawkins@reading.ac.uk*

Abstract: This paper reports the first derived thermo-optical properties for vacuum deposited infrared thin films embedded in multilayers. These properties were extracted from the temperature-dependence of manufactured narrow bandpass filters across the 4-17 μm mid-infrared wavelength region. Using a repository of spaceflight multi-cavity bandpass filters, the thermo-optical expansion coefficients of PbTe and ZnSe were determined across an elevated temperature range 20-160 °C. Embedded ZnSe films showed thermo-optical properties similar to reported bulk values, whilst the embedded PbTe films of lower optical density, deviate from reference literature sources. Detailed knowledge of derived coefficients is essential to the multilayer design of temperature-invariant narrow bandpass filters for use in non-cooled infrared detection systems. We further present manufacture of the first reported temperature-invariant multi-cavity narrow bandpass filter utilizing PbS chalcogenide layer material.

OCIS codes: (350.2460) Filters, interference; (300.6340) Spectroscopy, infrared; (310.0310) Thin films; (310.4165) Multilayer design; (310.6188) Spectral properties; (310.6860) Thin films, optical properties.

References and links

1. J. S. Seeley, R. Hunneman, and A. Whatley, "Far infrared filters for the Galileo-Jupiter and other missions," Appl. Opt. **20**(1), 31–39 (1981).
2. J. S. Seeley, R. Hunneman, and A. Whatley, "Temperature-invariant and other narrow band IR filters containing PbTe, 4-20 um," Proc. SPIE **246**, 83–94 (1980).
3. G. J. Hawkins, J. S. Seeley, and R. Hunneman, "Spectral characterization of cooled filters for remote sensing," Proc. SPIE **915**, 71–78 (1988).
4. B. Li, S. Zhang, J. Jiang, D. Q. Liu, and F. Zhang, "Recent progress in improving low-temperature stability of infrared thin-film interference filters," Opt. Express **13**(17), 6376–6380 (2005).
5. T. Stolberg-Rohr and G. J. Hawkins, "Spectral design of temperature-invariant narrow bandpass filters for the mid-infrared," Opt. Express **23**(1), 580–596 (2015).
6. T. Stolberg-Rohr, R. Buchner, S. Clausen, J. M. Jensen, A. Skouboe, G. Hawkins, and R. S. Hansen, "In optics humidity compensation in NDIR exhaust gas measurements of NO2," in Advanced Photonics Conference, OSA Technical Digest (online) (Optical Society of America, 2014), paper SeTh1C.3.
7. M. N. Polyanskiy, "Refractive index database," http://refractiveindex.info (accessed Feb. 29 2015)
8. E. Palik, *Handbook of Optical Constants of Solids* (Academic Press, Inc. 1985).
9. K. Zhang, J. Seeley, R. Hunneman, and G. Hawkins, "Optical and semiconductor properties of lead telluride coatings," Proc. SPIE **1125**, 45–52 (1989).
10. J. N. Zemel, J. D. Jensen, and R. B. Schoolar, "Electrical and optical properties of epitaxial films of PbS, PbSe, PbTe, and SnTe," Phys. Rev. **140**(1A), A330–A342 (1965).
11. Yu. I. Ravich, B. A. Efimova, and I. A. Smirnov, *Semiconducting Lead Chalcogenides* (Plenum Press, 1970).
12. R. A. Feldman, D. Horowitz, and R. M. Waxler, "Refractive properties of infrared window materials" *in Proceedings of Laser induced damage in optical materials*, (SPIE, 1977).

#240040 - $15.00 USD Received 29 Apr 2015; revised 5 Jun 2015; accepted 8 Jun 2015; published 11 Jun 2015

13. C.-H. Su, S. Feth, and S. L. Lehoczky, "Thermal expansioncoefficient of ZnSe crystal between 17 and 1080 °C by interferometry," Mater. Lett. **63**(17), 1475–1477 (2009).
14. G. J. Hawkins, R. Hunneman, R. Sherwood, and B. M. Barrett, "Infrared filters and coatings for the High Resolution Dynamics Limb Sounder (6-18 μm)," Appl. Opt. **39**(28), 5221–5230 (2000).
15. G. J. Hawkins, R. E. Sherwood, B. M. Barrett, M. Wallace, H. J. B. Orr, K. Matthews, and S. Bisht, "High-performance infrared narrow-bandpass filters for the Indian National Satellite System meteorological instrument (INSAT-3D)," Appl. Opt. **47**(13), 2346–2356 (2008).
16. G. Hawkins, R. Sherwood, K. Djotni, P. Coppo, H. Höhnemann, and F. Belli, "Cooled infrared filters and dichroics for the Sea and Land Surface Temperature Radiometer," Appl. Opt. **52**(10), 2125–2135 (2013).
17. C. S. Evans, R. Hunneman, and J. S. Seeley, "Optical thickness changes in freshly deposited layers of lead telluride," J. Phys. D Appl. Phys. **9**(2), 321–328 (1976).
18. P. Klocek, *Handbook of Infrared Materials* (Marcel Dekker, inc., 1991).
19. J. G. N. Braithwaite, "Infra-red filters using evaporated layers of lead sulphide, lead selenide and lead telluride," J. Sci. Instrum. **32**(1), 10–11 (1955).
20. R. Dalvern, "A review of the semiconductor properties of PbTe, PbSe, PbS and PbO," Infrared Phys. **9**, 1740–1744 (1996).
21. H. Takashashi, "Temperature stability of thin-film narrow-bandpass filters produced by ion-assisted deposition," Appl. Opt. **34**(4), 667–675 (1995).

1. Introduction

The optical and semiconductor properties of group IV-VI Lead chalcogenide compounds has been a subject of thin film research for several decades [1]. Lead Telluride (PbTe) has been deployed in multilayers extensively over this period as a mid-infrared interference material, being particularly valuable in the coating design due to its high refractive index ($n \approx 5.5$) and long-wave spectral location of its electronic absorption edge. It is also distinctive amongst other transparent infrared materials because of its negative refractive index temperature coefficient which enables the unique construction of temperature-invariant narrow bandpass filters [2–4] across both cooled and elevated operating temperatures.

We previously conducted a systematic investigation into the design of temperature-invariant narrow bandpass filters, from which we demonstrated the thermo-optical properties of PbTe films accessible from literature sources were insufficient to accurately predict the temperature-induced wavelength shift of PbTe/ZnSe multi-cavity narrow bandpass filters across an elevated temperature range 20-200 °C [5]. Thus, an improved and refined understanding of thin film thermo-optical properties is essential to simulate, and gain control of the behavior of bandpass temperature-invariance demanded by non-cooled infrared optical systems [6]. We further introduced a thermo-optical expansion coefficient term (γ), which denotes the expansion in optical thickness (δ) with increasing temperature. The optical thickness, being the product of the physical thickness (l) and the refractive index (n) $\delta = nl2\pi/\lambda$, whilst the temperature derivative of δ is the sum of the temperature derivatives of l and n;

$$\gamma = \frac{1}{\delta}\frac{d\delta}{dT} = \frac{1}{l}\frac{dl}{dT} + \frac{1}{\delta}\frac{dn}{dT}$$

The thermo-optical expansion coefficient (γ) is a crucial term, as it is primarily this material property that is responsible for the wavelength shift with temperature exhibited by any optical thin film multilayer. In a binary material narrow bandpass filter, we showed in [5] that the center wavelength shift with temperature obeys the linear relation in Eq. (1).

$$\frac{1}{\lambda_C}\frac{d\lambda_C}{dT} = s_L \gamma^L + s_H \gamma^H \tag{1}$$

Where γ^L and γ^H are the thermo-optical expansion coefficients of the low and high index layers respectively, and S_L and S_H are sensitivity factors describing the proportional weighting of the two materials ($S_L + S_H = 1$) which are determined as a function of the multilayer design. However, wavelength-dependence is not a direct function of material

#240040 - $15.00 USD Received 29 Apr 2015; revised 5 Jun 2015; accepted 8 Jun 2015; published 11 Jun 2015

quantity; cavity layers dominate sensitivity, whilst the influence of reflector layer count reduces sensitivity in proportion with distance between cavities, as described by [2]. Equation (1) shows that temperature-invariance naturally requires one of the materials to exhibit negative optical expansion ($\gamma < 0$). This property is however known only to exist in thin film materials with a lead (Pb) based composition, i.e., PbTe and other lead chalcogenides, which strongly motivates improved understanding for these thermo-optical properties.

In this paper we utilize the elevated temperature measurements from a comprehensive repository of historic spaceflight bandpass filters, previously described in [5] to derive a new, realistic and practical data set of thermal-optical properties (γ) for embedded polycrystalline thin films of PbTe and ZnSe within a multilayer. We further consider the application of other alternative Pb-salts (PbSe, PbS) to broaden the range of temperature-invariance towards shorter wavelengths, and present the first reported thin film SWIR bandpass filter at 3.0 μm exhibiting temperature-invariance and utilizing the negative thermo-optical expansion of lead sulphide (PbS).

2. Thermo-optical source data

In [5] we conducted a literature survey to determine the existing sources of thermo-optical properties for PbTe and ZnSe in both bulk and thin film form with a particular focus on elevated temperatures across the 20-200 °C range. Our investigation concluded that the optical data available for these materials is exceptionally scarce. Where temperature measurements currently exist, this data is very coarse, or unsuitable for the desired wavelength regions. Valuable reference databases exist [7], which aim to create easy access to reported refractive index properties of various optical materials, however its temperature-dependence (*dn*/*dT*) property is rarely specified. A further challenge of incorporating thermo-optical properties in thin film simulations remains the non-specific physical condition from reported measurements which will differ to layers embedded within a multilayer assembly. Many reported thin film measurements are performed on single films exposed to ambient environments [8, 9] which are likely to deviate in their stress condition from embedded films in the multilayer structure. Other thin films are epitaxial single-crystalline films, which in [10] were found to resemble bulk properties, whilst the thin films deposited by physical vapor deposition are typically of a polycrystalline columnar structure, as is the case for our selection of manufactured bandpass filters. In addition to this, variations in deposition conditions affect stoichiometry, crystal morphology, and packing density all of which influence the opto-mechanical properties of the deposited films.

For evaporated PbTe layer material, refractive index temperature measurements were reported for exposed polycrystalline [9] and single-crystalline films [10], and, as anticipated, omission of any data for embedded polycrystalline films. Data on thermal expansion was expectedly only found in bulk form [11]. For ZnSe we found no reported thin film measurements of the refractive index temperature coefficient, however bulk refractive index coefficient data is available from Feldman [12]. The thermal expansion coefficient was measured for exposed thin films in [13] however the experimental coefficients were of such high magnitude that they were dismissed as unrealistic in proportion to embedded thin film properties and behavior.

3. Experimental data and simulation method

To acquire the embedded thermo-optical data properties for thin film simulations, we characterized and correlated the thermal behavior from a historic repository [14–16] of PbTe/ZnSe narrow bandpass filters, manufactured over a course of two decades, and covering a wide range of wavelengths, bandwidths, and multilayer design types. These filters were manufactured by thermal evaporation using a modified Balzers BA510 deposition chamber. This deposition system is especially fitted with a tooling arrangement of rotating evaporation

#240040 - $15.00 USD Received 29 Apr 2015; revised 5 Jun 2015; accepted 8 Jun 2015; published 11 Jun 2015

sources and stationary substrates. This static substrate arrangement is particularly important for the deposition of precision thin-film multilayers, as the need for accurate elevated temperature control is essential to maintain good opto-mechanical properties of the materials, particularly as the stoichiometry and sticking coefficient of chalcogenides are highly temperature dependent. The selection of bandpass filters used in this study were deposited with substrate temperatures between 185 and 210 °C. Further deposition details are discussed in the papers where the filters were first published [14–16]. The filters were all newly characterized by extraction from high temperature FTIR spectral measurements across the range of 20-200 °C, where the observed wavelength displacements were correlated with multilayer design properties in [5]. The wavelength shift with temperature was accurately modelled using Eq. (1).

In order to determine the thermo-optical expansion coefficient for the embedded thin films of both PbTe and ZnSe layer materials, only a minimum of two filters is required with common center wavelength, but of significantly different multilayer design. This establishes two or more simultaneous equations to solve with respect to the two unknown optical properties. This requirement was achieved at three different wavelengths; 4.3 μm, 10.4 μm, and 12.1 μm. The sensitivity factors were determined from the multilayer properties, and presented in [5] for the relevant designs. In Fig. 1, the measured center wavelength shift with temperature is shown for three center wavelengths as a function of the low-index sensitivity weighting factor S_L. Equation (1) contains only one independent variable, since the high- and low-index sensitivity weighting factors adds up to unity ($S_L + S_H = 1$). Thus, the equation can be written and solved as a linear function of either variable, e.g., $\frac{1}{\lambda_c}\frac{d\lambda_c}{dT} = \left(\gamma^L - \gamma^H\right)S_L + \gamma^H$. Hence in Fig. 1, the intersection with the y-axis ($S_L = 0$) shows γ^H, whilst the slope gives $\gamma^L - \gamma^H$. As we have more than two filters at each of the three wavelengths, comprising; 11 filters at 4.3 μm, 4 filters at 10.4 μm, and 10 filters at 12.0 μm, we performed a multivariate least squares fit to obtain the desired material properties of γ^{PbTe} and γ^{ZnSe} at the selected wavelengths. The shift in center wavelength on the y-axis is the mean shift across the 20-160 °C temperature range. The upper limit was chosen to avoid non-linear behavior which was exhibited by some filters at temperatures greater than 160 °C. Filters in the 4 μm region showed a temperature displacement with a tendency to reduce when approaching the higher temperatures, even within this range. This was primarily due to the reduced influence of electronic absorption in the PbTe material, shifting to shorter wavelengths on heating. The value fitted at the 4.3 μm wavelength is thus an average value over the temperature range, and will be slightly higher at room temperature.

#240040 - $15.00 USD Received 29 Apr 2015; revised 5 Jun 2015; accepted 8 Jun 2015; published 11 Jun 2015

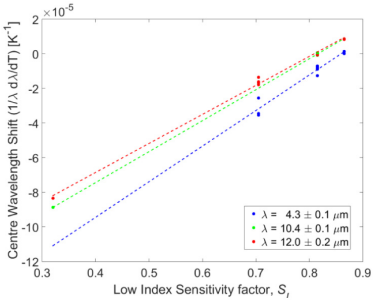

Fig. 1. Measured center wavelength shift with temperature as a function of multilayer design specified by the low index sensitivity factor (dots) shown together with the results of multivariate least square fits (lines).

4. Results

Applying the measured wavelength shift properties with temperature, a thermo-optical expansion coefficient for the embedded thin films was derived for both PbTe and ZnSe at three different mid-infrared wavelengths. The resulting coefficients are given in Table 1, and shown in Fig. 2 together with corresponding literature data.

Table 1. Thermo-optical expansion coefficients derived for embedded PbTe and ZnSe films.

λ [μm]	γ^{PbTe} [10^{-5} K^{-1}]	γ^{ZnSe} [10^{-5} K^{-1}]
4.3	−17.7 ± 2.3	2.9 ± 0.8
10.4	−14.6 ± 0.7	3.3 ± 0.2
12.0	−13.6 ± 1.1	3.2 ± 0.6

To each extracted coefficient we have given a variance which was generated by fixing one coefficient in Eq. (1) at a time and calculating the resulting sample standard deviation for the temperature coefficient of the alternate material. The stated variances in Table 1 represent twice the sample standard deviation (± 2σ) and is further included in Fig. 2 as vertical error bars. Whilst these variations may appear large in value, they are small compared to the discrepancies within the currently existing knowledge of thin film PbTe properties.

#240040 - $15.00 USD Received 29 Apr 2015; revised 5 Jun 2015; accepted 8 Jun 2015; published 11 Jun 2015

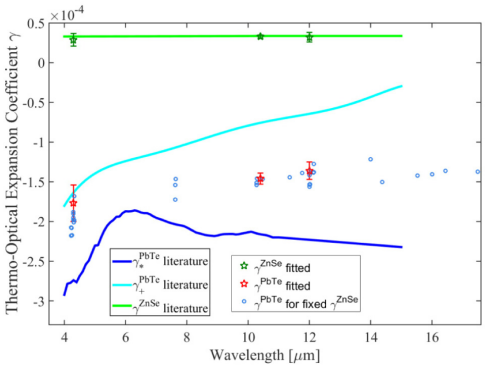

Fig. 2. Thermo-optical expansion coefficients of embedded PbTe and ZnSe determined by multivariate least square fit to Eq. (1) shown together with literature data, the origin of which are listed in Table 2. Additionally, a value for $\boldsymbol{\gamma}^{\mathbf{PbTe}}$ was extracted from each bandpass filters based on a fixed $\boldsymbol{\gamma}^{\mathbf{ZnSe}}$ value.

Reference literature values for ZnSe offers a near wavelength-independent value of γ based on bulk samples; $\gamma^{\mathrm{ZnSe}} = 3.4 \cdot 10^{-5}\ \mathrm{K}^{-1}$. This value is in very good agreement with our findings of $3.25 \cdot 10^{-5}\ \mathrm{K}^{-1}$ in the long wavelength region. At 4.3 µm, we extract a slightly lower value of $2.9 \cdot 10^{-5}\ \mathrm{K}^{-1}$. Although still within the experimental variation, we consider that the low value is a consequence of the electronic absorption edge influence of PbTe receding from the bandpass filter as the temperature increases and skewing the measurement of $d\lambda / dT$. In total, it appears that embedded polycrystalline thin films of ZnSe exhibit optical properties similar to those of bulk ZnSe, whilst in contrast for PbTe, we obtain values that are significantly different from the literature data. This can be understood in terms of a lower optical density of deposited PbTe film [17], compared to single-crystal material which is the origin of the γ_*^{PbTe} data [10]. In contrast, the polycrystalline γ_+^{PbTe} data was obtained from exposed PbTe film [9], which is not subject to the similar mechanical stresses experienced by the embedded films. It is therefore reasonable to conclude the embedded thin film values lies between these two extrema.

Table 2. Origin of reference α and β literature data

$\gamma = \alpha + \beta$	$\alpha = \frac{1}{l}\frac{dl}{dT}$	$\beta = \frac{1}{n}\frac{dn}{dT}$
γ_*^{PbTe} $-21 \cdot 10^{-5}\ \mathrm{K}^{-1}$	*bulk* [11] $2.0 \cdot 10^{-5}\ \mathrm{K}^{-1}$	*Single-crystal, exposed film* [10] $-23 \cdot 10^{-5}\ \mathrm{K}^{-1}$ (at 10 µm)
γ_+^{PbTe} $-7.9 \cdot 10^{-5}\ \mathrm{K}^{-1}$		*Polycrystalline, exposed film* [9] $-9.9 \cdot 10^{-5}\ \mathrm{K}^{-1}$ (at 10 µm)
γ^{ZnSe} $3.4 \cdot 10^{-5}\ \mathrm{K}^{-1}$	*bulk* [18] $0.77 \cdot 10^{-5}\ \mathrm{K}^{-1}$	*Bulk* [12] $2.6 \cdot 10^{-5}\ \mathrm{K}^{-1}$

At wavelengths where bandpass filters with two distinct multilayer designs were not available to permit a multivariate fit, we applied the method of fixing γ^{ZnSe} to literature values. This is justified by the good agreement obtained with literature γ^{ZnSe} established

using the multivariate fits. In this manner we obtained a value for γ^{PbTe} for each bandpass filter by the solution of Eq. (1);

$$\gamma^{H} = \left(\frac{1}{\lambda_c} \frac{d\lambda_c}{dT} - s_L \gamma^{L} \right) \Big/ s_H \tag{2}$$

The resulting extracted coefficients are shown in Fig. 2 along with the multivariate fit results, which offer an indication of the experimental variations together with additional information about wavelength-dependence.

5. PbS temperature-invariant narrow bandpass filter

Whilst the concept of temperature-invariance has been governed by the opposing negative temperature coefficients of PbTe and complementary dielectric layer pair, extending the application of invariant narrow bandpass filters towards the shorter infrared wavelength region (SWIR) requires the use of a lighter molecular mass lead chalcogenide salt. The deployment of Galena, lead (II) sulphide (PbS) multilayer was first suggested as a material by Braithwaite [19] in 1954, from which attempts to manufacture interference layers were unsuccessful at that time due to unexpectedly high absorption, induced by poor stoichiometry decomposition during deposition. PbS has subsequently remained an unutilized layer material that has been extensively reported for its semiconductor properties in opto-electronic quantum dot infrared photodetectors and photovoltaic devices, but as a transparent infrared layer material has been scarcely reported in literature sources for over 60 years. Here we present the manufacture of the first fully-transparent temperature-invariant narrow bandpass filter comprising a PbS/ZnSe 3-cavity multilayer of 8% FWHM bandwidth at 3.0 μm. The PbS/ZnSe bandpass is deposited on a Sapphire substrate and similarly exhibits invariant wavelength behavior throughout the 20-200 °C temperature range (Fig. 3).

Manufacture of the filter was performed by conventional thermal deposition using the same experimental conditions as PbTe, however avoiding the differential stoichiometric loss and free carrier absorption were compensated by the introduction of a partial pressure of oxygen into the chamber during PbS layer deposition. This was best performed at a pressure of $4x10^{-5}$ Torr, from which transparency becomes fully restored. The lower absorption properties of PbS in comparison with PbTe subsequently offers transparency across the SWIR wavelength region down as far as 2.3 μm ($\alpha<1x10^4$ cm^{-1}) [20]. Simulations of refractive index matching, based on the bandpass FWHM and bandwidth broadening with temperature (0.1 nm K^{-1}), suggests a deposited PbS thin film refractive index of 4.0 at 20 °C decreasing to 3.82 at 200 °C. The center wavelength stability is better than 0.02 nm K^{-1}. The thermo-optical expansion coefficient for bulk PbS is close to PbTe at long wavelengths ~2.3 K^{-1} (8-10 μm) with a rapid decrease towards the absorption edge at 2.3 μm [10,11]. The experimental data available for PbS is still too scarce to extract a reliable experimental value, but preliminary results indicate that thin film temperature coefficient (as for PbTe) is significantly less negative than the bulk value. Further determination of γ^{PbS} is of ongoing research.

Environmental durability of this deposited PbS/ZnSe multilayer was assessed by subjecting 1-inch diameter witness samples to the general provisions of military specification MIL-F-48616. This testing included a visual surface quality assessment, adhesion testing, moderate abrasion, humidity testing at 50 °C for 24 hours in >95% relative humidity, together with additional cryogenic to high temperature thermal cycling (20–473 K) and liquid nitrogen thermal shock testing. Further extreme testing included dicing by diamond saw in deionized water lubricant, all of which passed with satisfactory compliance.

#240040 - $15.00 USD Received 29 Apr 2015; revised 5 Jun 2015; accepted 8 Jun 2015; published 11 Jun 2015

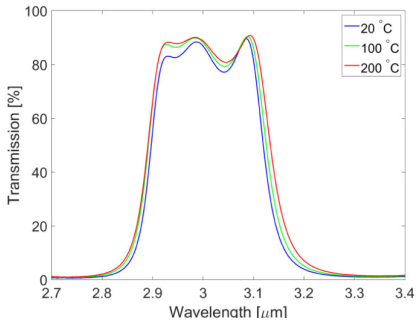

Fig. 3. Temperature-invariant PbS/ZnSe 8% FWHM narrow bandpass filter at 3.0 μm on Sapphire (Single-side coating inclusive of rear surface reflection losses)

6. Discussion

The narrow bandpass filter set from which the presented data was extracted, are all double-side coated complete manufactured optical filters, that contain continuous out-of-band wavelength blocking and antireflection matching layers. The passband ripples of these subsidiary blocking stacks may exert some influence to modulate the final shape and center wavelength positioning of the bandpass profile. However, in [5] we showed that random layer thickness errors have negligible influence on the temperature-invariance transmission profile, as this is dominated by the design and materials interdependence. The substrate has previously been reported to influence temperature dependence of narrow bandpass filters [21] but in [5] the choice of substrate, or substrate thickness did not appear to affect the temperature behavior of the bandpass filter profile. Further, although all of the filters studied were of triple half-wave (3-cavity) multilayers, we can consider the extracted thermo-optical values to be representative also for embedded thin films in other multilayer structures, particularly as variations in cavity order and number of inter-cavity layers did not appear to affect the thermo-optical behavior. However, the precise deposition conditions may conceal further opto-mechanical stress dependence of the extracted thermo-optical properties.

7. Conclusions

In this investigation we have derived the thermo-optical expansion coefficients for embedded thin films of polycrystalline PbTe and ZnSe. Embedded thin film ZnSe was found to exhibit bulk thermo-optical properties, whilst embedded thin film PbTe deviated significantly from reported literature values. This was attributed to the lower density of deposited PbTe film compared to single-crystal material. A thin film bandpass filter based on thermally deposited PbS material was demonstrated, extending the range of temperature-invariant behavior to shorter wavelengths and a wider range of bandwidths.

Acknowledgments

The authors thank colleagues at Schlumberger Cambridge Research for discussions and grateful support under contract reference QU-RDU-01274-C, Thomine is an industrial PhD student at Danfoss IXA A/S and her work is supported by the Danish Agency of Science, Technology and Innovation (DASTI). Thanks also to Richard Sherwood and Karim Djotni at the University of Reading for their assistance with spectral measurements and thin film depositions, which is gratefully acknowledged.

APPENDIX $\mathfrak{D}$

Paper 4: High Temperature and High Pressure Gas Cell for Quantitative Spectroscopic Measurements

Journal of Quantitative Spectroscopy & Radiative Transfer 169 (2016) 96–103

Contents lists available at ScienceDirect

Journal of Quantitative Spectroscopy & Radiative Transfer

journal homepage: www.elsevier.com/locate/jqsrt

High temperature and high pressure gas cell for quantitative spectroscopic measurements

Caspar Christiansen [a], Thomine Stolberg-Rohr [a,b,*], Alexander Fateev [a], Sønnik Clausen [a]

[a] Department of Chemical Engineering, Technical University of Denmark, Frederiksborgvej 399, Building 313, DK-4000 Roskilde, Denmark
[b] Danfoss IXA A/S, Ulvehavevej 61, DK-7100 Vejle, Denmark

ARTICLE INFO

Article history:
Received 10 June 2015
Received in revised form
12 October 2015
Accepted 13 October 2015
Available online 20 October 2015

Keywords:
CO_2
Gas cell
Infrared
Temperature
Pressure
Combustion

ABSTRACT

A high temperature and high pressure gas cell (HTPGC) has been manufactured for quantitative spectroscopic measurements in the pressure range 1–200 bar and temperature range 300–1300 K. In the present work the cell was employed at up to 100 bar and 1000 K, and measured absorption coefficients of a CO_2–N_2 mixture at 100 bar and 1000 K are revealed for the first time, exceeding the high temperature and pressure combinations previously reported. This paper discusses the design considerations involved in the construction of the cell and presents validation measurements compared against simulated spectra, as well as published experimental data.

1. Introduction

The interest in high temperature and high pressure CO_2 data emerges from two very different fields of research; the scientific study of the atmosphere of Mars and Venus [1] and the industrially motivated research in combustion engines for which high temperature and pressure absorption spectra are required for proper modeling of the heat transfer processes [2]. This work is motivated by the latter, and has formed part of a larger project named Radiade [3], which focusses on the improvement of radiant heat transfer models at high pressure and temperature for modeling of combustion, fluid flow, and radiation heat transfer phenomena as well as their mutual interactions [4]. However, the experimental results presented in this paper are expected be of equal interest to the first mentioned research area as the most recent release notes of the HITRAN (2012) database states; "*High-quality reference spectroscopic data for the carbon dioxide molecule remains one of the top priorities for the HITRAN database, due in part to its importance for the environmental satellite missions, including OCO-2 and GOSAT and its importance to the studies of the atmospheres of Mars and Venus*" [5].

A number of gas cells have already been constructed and utilized to acquire spectroscopic measurements of CO_2 at elevated temperatures and pressures [6–8]. Common to the gas cells is that they are built of metal, a material which is easy to machine and exhibits good thermal conductivity, assuring uniform temperature distribution. However, metal loses its strength at high temperature. In recent work by Stefani et al. [8] a commercial gas cell was employed which was designed for temperatures up to 650 K and pressures up to 200 bar. In terms of pressure this is sufficient to cover the peak pressures inside two-stroke ship engines, however, combustion temperatures are much higher. Thus for combustion heat transfer modeling, experimental data at even higher temperatures is required. The present gas cell cover the pressure levels

* Corresponding author. Tel.: +45 74888570; fax: +45 7488 8708.
E-mail address: thomine@danfoss.com (T. Stolberg-Rohr).

http://dx.doi.org/10.1016/j.jqsrt.2015.10.006
0022-4073/

typical for combustion engines, and raises the temperature to as high as 1300 K. Whilst this offers a great step into unexplored territory, it remains a demand for future gas cells to reach temperatures above 2400 K at high pressures to cover all engine conditions.

The present paper discusses the design of HTPGC including the choices and trade-offs involved. The cell is validated against previously published experiments as well simulations based on the HITRAN2012 database [5]. Finally, a recently recorded spectrum of 5% CO_2 in N_2 at 101 bar and 1000 K is presented, well outside the parametric space of previous experimental gas cell studies of infrared CO_2 absorption.

2. Design of the high temperature and high pressure gas cell

The design of a high temperature and high pressure gas cell involves a number of choices and trade-offs, including cell material, window material, sealing method, dimensioning and safety. A sketch of HTPGC is shown in Fig. 1. A 3-D drawing of the cell is shown at the top and a cross-section including dimensions is shown at the bottom of the figure. The outer and inner tubes of the cell are made of a high grade ceramic (aluminum oxide, 99.5%) that exhibits great strength even at high temperatures where metal capitulates. Ceramics are fragile and difficult to machine but, in return, exhibit low thermal expansion and are less troubled by undesired surface reactions. The ceramic tubes are concentrically aligned as shown in the figure and fixed by two water cooled brass flanges in the ends. The brass flanges are bonded to the ceramic by means of a high temperature epoxy (J–B Weld). Holes located at the center of each flange allow for a straight line of sight through the inner tubes.

Slightly tilted 3.0 mm thick ½″ sapphire windows are glass bonded to each end of the inner tubes in order to obtain a gas tight high temperature seal. The use of sapphire windows restricts the wavelength range that can be studied with this gas cell since sapphire blocks radiation above ~6 μm, depending on window thickness and temperature. On the other hand, sapphire is extremely robust and has a thermal expansion that is well matched to the ceramics in the target temperature range. The latter is crucial in order to reduce thermal stresses. The volume confined by the two sapphire windows and the outer tube is the optically accessible measurement volume with a path length of 30.3 mm ± 0.1 mm. The choice of a relatively short path length is advantageous at high gas densities. The low thermal expansion coefficient implies that the temperature dependence of the path length is very small, e.g. at 1000 K a pathlength increase of 0.02 mm is estimated compared to room temperature. Three separate heating coils protected by ceramic beads are wound around the outer ceramic tube (not shown in the figure). One heating coil is covering the central zone around the measurement volume and the two other heating coils are placed symmetrically at each side next to the central zone. At each zone a thermocouple is placed and temperature control is applied to each zone independently, assuring high temperature uniformity over the measurement path and compensation for additional heat loss at the windows. In addition to the three thermocouples used for controlling the heat zones, a total of six very thin ceramic tubes are running parallel with the center axis in the cavity between the outer and inner ceramic tubes. These tiny tubes are exactly thick enough for a 0.5 mm type N thermocouple to be inserted from the outside, and under steady temperature conditions, the thermocouple reflects the gas temperature. A calibrated thermocouple can be cautiously slided inside the ceramic tube to map the internal temperature field over the measurement path. Although the thermocouple is calibrated to a specified accuracy of 0.4 K at 300 K and 0.8 K at 1000 K, the uncertainty of the measured gas temperature is larger because it is dominated by temperature distributions, which is discussed in Section 3.1.

The heating zones are thermally insulated in order to reduce energy losses. A picture of the insulated gas cell is shown in Fig. 2. One of the end flanges can be seen to the left along with a small piece of the outer ceramic tube.

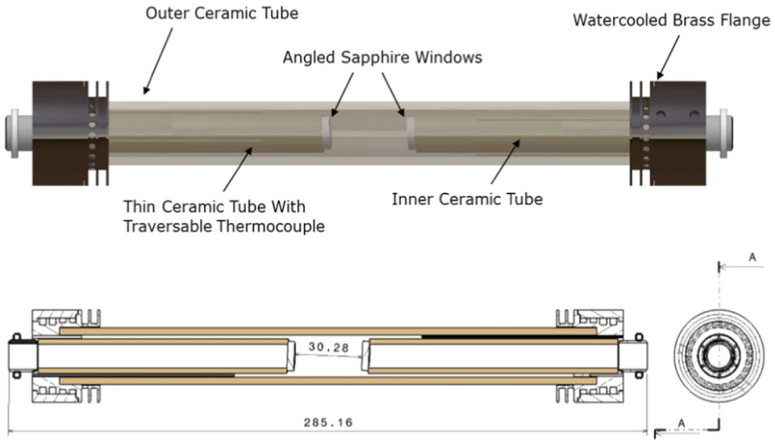

Fig. 1. Top: 3-D drawing of HTPGC. Bottom: cross-section sketch of HPTGC including dimensions in mm. The ends of the inner ceramic tubes at the flanges are open.

Coiled tubes (gas inlets and outlets), water cooling inlet and outlet, heat coil terminals, and thermocouple wires can also be seen in the picture.

Two gas inlets or outlet tubes are located at each flange and are connected to a flow control gas mixing system specified for pressures up to 200 bar. The gas enters the cell in the vacancy between the two ceramic tubes which serves to preheat the gas, which is important if the cell is to be operated in flow mode. In this work, however, the gas cell is used in static mode. The pressure is measured at the outlet tube by a Kistler pizoresistive pressure sensor, which for the presented measurements was calibrated in the 0–100 bar with an accuracy of ± 0.25 bar. For measurements at atmospheric pressure, the pressure was instead measured by an external Rosemount pressure sensor with accuracy ± 0.005 bar. HTPGC is designed to handle pressures up to 200 bar and temperatures up to 1300 K but in the measurements presented for this paper measurements were limited to 100 bar and 1000 K which is in itself well outside previously studied conditions, intending to gather as much useful knowledge as possible about gas absorption before stepping further into the unexplored territory with the potential risk of permanently damaging the cell.

3. Validation of the high temperature and high pressure gas cell

To validate the strength and the tightness of the gas cell and particularly the epoxy sealing, a dummy cell in the same design was filled with nitrogen at a pressure of 200 bar. Subsequently, without water cooling of the end flanges, the cell was slowly heated until the sealing collapsed. This happened at 90 °C which agrees with the epoxy specification. During measurements at elevated temperatures, the end flanges were water cooled and maintained below 30 °C and thus the cell stays tight when heated. However, to avoid accidents during measurements a steel shield was built around the cell. The pressure level in the static cell reveals whether the cell including supply tubes is tight during measurements. At room temperature and 80 bar the cell leaks 25 ml_n/min but at higher temperatures the leakage is strongly reduced. At both 627 K and 1000 K the leakage is 5 ml_n/min at 100 bar. The leakage implies a need to add target gas continuously to maintain the pressure. This does not compromise the measurement results if the target gas does not leak into the inactive optical path. In this work, however, a post-examination of the setup eventually revealed that the gas did in fact leak into the inactive path. Since this causes potential errors, the gas cell design is currently being improved. However, the inactive path is continuously flushed with nitrogen which removes and high spectral resolution measurements, which are able to identify gas at low pressures, have shown that the effect on the presented measurements is small.

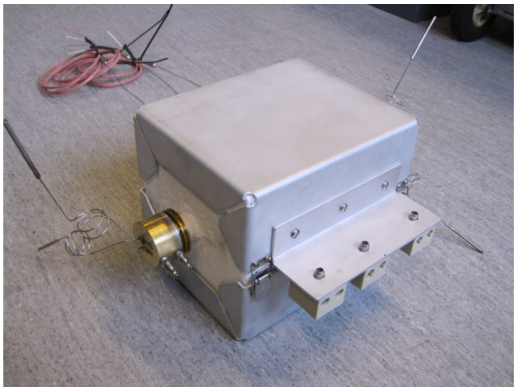

Fig. 2. HTPGC with insulation box. One of the brass flanges is visible to the left along with a small part of the outer ceramic tube. The coiled stainless steel tubes are the gas inlets and outlets, whilst the small stainless steel pipes forms part of the water cooling system. Three terminals, one for each heat zone, are seen at the front of the box. The pink wires at the back are the three thermocouples used by the temperature controller. (For interpretation of the references to color in this figure, the reader is referred to the web version of this article.)

3.1. Temperature uniformity

Fig. 3 shows measurements of the temperature uniformity obtained at different temperatures. The temperature uniformity over the length of the measurement path ranges from ± 2 K at 445 K ($\pm 0.5\%$) to ± 1 K at 1000 K ($\pm 0.1\%$) which means that the contribution to the overall measurement uncertainty is low.

4. Experimental setup for spectroscopic measurements

In order to obtain spectroscopic measurement with HTPGC an experimental setup was build and sketched in Fig. 4. The source is a temperature-controlled water cooled blackbody cavity source at 800 °C. For background measurement it has an electronically activated mirror flip redirecting the field of view into a room temperature beam dump cavity. On the spectrometer side a Nicolet 5700 FTIR spectrometer was used, with highest nominal spectral resolution 0.125 cm^{-1} and equipped with a liquid nitrogen-cooled InSb detector. All optical path, apart from the measurement volume, was continuously purged with dry, CO_2-free air from a purge air generator. A gas mixing system in stainless steel handling both inlet and outlet pressures up to 200 bar allows a continuous range of gas concentrations to be studied. However, in this paper, all measurements were carried out with high grade pure or premixed gases to eliminate any uncertainties from the gas mixing. A vacuum pump was used to flush the measurement chamber as well as gas lines and other dead volumes.

5. Measurement and calculation procedure

The procedure for exchanging the gas cell volume is first to empty the gas cell by a vacuum pump for a few seconds, until the pressure is below 0.2 bar, and refilling the cell with the new sample gas. The pumping is done 5 times resulting in a purity of the new gas of $>99.9\%$.

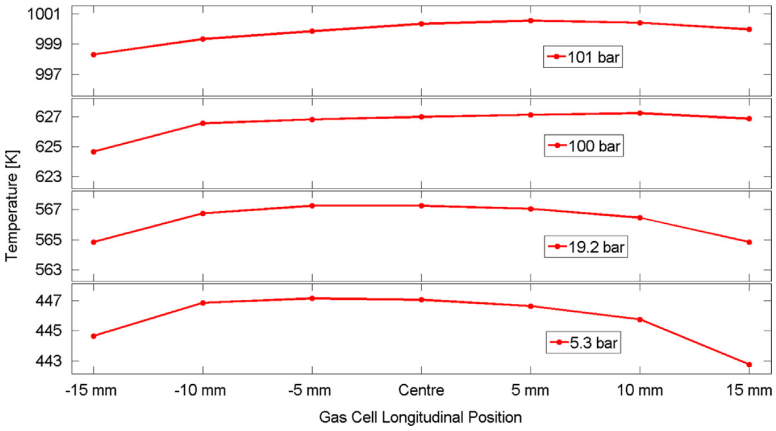

Fig. 3. Temperature distribution over the length of HTPGC at 446 K, 566 K, 627 K, and 1000 K.

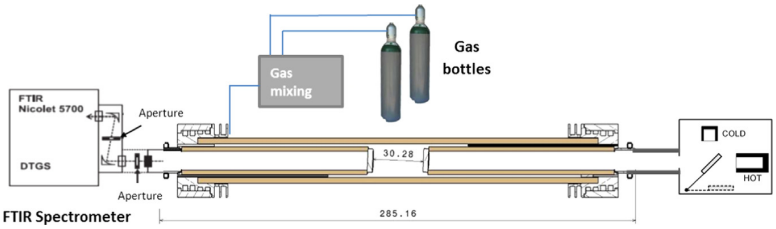

Fig. 4. Measurement setup. The experimental setup comprises gas bottles, gas mixing, flow controllers, HTPGC, a black body source with build-in flip mirror, and a spectrometer. Dimensions are in mm.

The desired physical quantity to be determined is the transmission through the gas which is governed by Beer–Lamberts law; $\tau_{gas}(\lambda) = \exp(-\sigma_\lambda NL)$, where σ_λ is the gas specific absorption cross-section, N is the number concentration and L is the pathlength.

Since the source intensity is not modulated in the setup used, the background radiation must be recorded in separate measurements and subtracted from the sample and reference spectra. Thus a total of 4 spectra are required to determine the transmission;

S:The sample spectrum; the gas cell is filled with the target gas.

I^S_{BG}: Background radiation spectrum; measured immediately after S whilst blocking the source radiation.

R:Reference spectrum; the gas cell is filled with the infrared inactive gas N_2. The source temperature and the optical setup must be stable between the recording of S and R.

I^R_{BG}: Background radiation spectrum corresponding to the reference spectrum; recorded immediately after R with the source blocked.

The first spectrum, S, gives us a source spectrum multiplied by the gas transmission added with the background radiation, $I^S_{BG}(\lambda)$ emitted from all surfaces, including the optical windows in the gas cell. The complete spectrum being convoluted by the instrument function of the FTIR, $\Gamma(\lambda)$;

$$S = \int d\lambda' \left(\Gamma(\lambda - \lambda') I_0(\lambda) \tau_{\mathrm{gas}}(\lambda)\right) + I^S_{BG}(\lambda)$$

I_0 is the source intensity which includes all losses through the optical system not related to gas absorption in the measurement volume.

In the presented measurements $I_0$and I^S_{BG} are approximately constant over the width of the instrument function and S simplifies to

$$S = I_0(\lambda) \int d\lambda' \Gamma(\lambda - \lambda')(\exp(-\sigma_\lambda NL)) + I^S_{BG}(\lambda)$$

A reference measurement is essential to determine the source intensity as well losses through the optical system. This is recorded under identical conditions but with the target gas exchanged by the infrared inactive gas N_2. With similar assumptions, R can be described as

$$R = I_0(\lambda) + I^R_{BG}(\lambda)$$

$I^S_{BG}(\lambda)$ and $I^R_{BG}(\lambda)$ are measured immediately after S and R, respectively by blocking the source with a mirrow pointing towards a cold beam dump to minimize a contribution to the background radiation from this surface.

With these 4 spectra acquired, the *apparent* transmission, $\tau^*(\lambda)$, can be calculated, which is the physical gas transmission convoluted with the instrument response

function;

$$\tau^*(\lambda) = \frac{S - I_{BG}^S}{R - I_{BG}^R} = \int d\lambda' \Gamma(\lambda - \lambda')(\exp(-\sigma_\lambda NL)) \quad (1)$$

At atmospheric pressures, gas absorption lines are spectrally narrow and cannot be properly resolved by the high resolution spectrometer of 0.125 cm^{-1}. However, as the pressure increases, the absorption lines are subject to pressure broadening. This is illustrated in Fig. 5 showing a CO spectrum measured at 26 °C with spectrometer resolution 0.125 cm^{-1} at 1 bar, 14.5 bar, and 40.5 bar. At 40.5 bar the high resolution is clearly unnecessary and can be significantly reduced in return for a better signal to noise ratio. Simulated transmission spectra are shown for 14.5 bar and 40.5 bar and illustrates how the discrepancy between the Voigt-based simulation and the measurement grows with increasing pressure. The simulated spectra are obtained using the HITRAN2012 database and the line-by-line calculation software spectralcalc.com [9], which employs the LinePak algorithms [10].

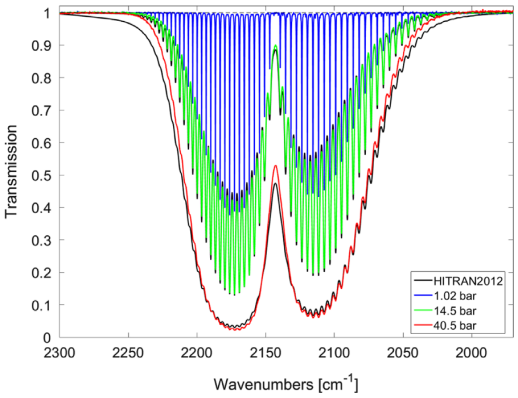

Fig. 5. Transmission of 1% CO in N_2 at increasing pressure measured with 0.125 cm^{-1} resolution. Simulated (Voigt line shape) transmission spectra are shown for 14.5 and 40.5 bar and 299 K (black curves).

As the spectral broadening of σ_λ surpasses the width of the instrument function by a factor of 5 [11], Γ, the calculated transmission T^* approaches the actual gas transmission, $T = \exp(-\sigma_\lambda NL)$;

$$\tau^*(\lambda) = \frac{S - I_{BG}^S}{R - I_{BG}^R} = \exp(-\sigma_\lambda NL) \quad (2)$$

And the absorption coefficient k can be directly extracted.

$$k = N\sigma_\lambda = -\ln(\tau^*(\lambda))/L$$

In conditions where the physical broadening is narrower than 5 times the instrument function, the measured transmission is denoted *apparent* transmission. The instrument function distributes the intensity over an interval but does not affect the integrated band absorption, which can therefore be compared against databases or other measurements recorded with similar *kL*.

All measurements presented in the remaining of this paper were recorded with a resolution of 2 cm^{-1} and using Blackmann–Harris as apodization function, which is also the choice in [8] to which HTPGC measurements are compared.

6. Validation of spectroscopic measurement performance

In this section the HTPGC measurements are validated. First, CO_2 measurements at ambient temperature and pressure are compared with simulations based on the database HITRAN2012 [5] and performed by SpectralCalc.com [9]. Secondly, the performance of HTPGC at high temperature and pressure is compared with previously reported high temperature and high pressure measurements. The ambient conditions (22 °C and 1.0 bar) serve to validate the basic setup under well-defined conditions. In

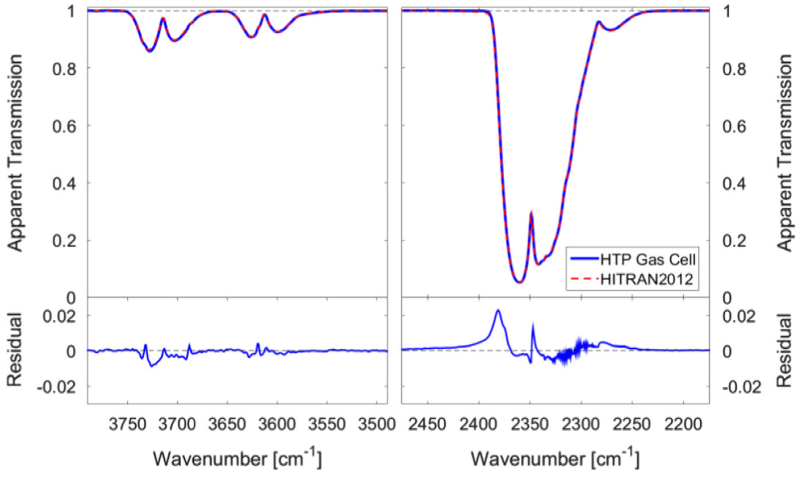

Fig. 6. Apparent transmission of 5% CO_2 in N_2 measured at ambient conditions (blue) and calculations based on the HITRAN2012 database (red). $P = 1.017$ bar and $T = 299.2$ K. (For interpretation of the references to color in this figure, the reader is referred to the web version of this article.)

Fig. 6, the measured two major CO_2 absorption bands, located around 2300 cm^{-1} and 3700 cm^{-1} are compared with simulations for 5% CO_2 in N_2. Both measurements as well as simulations use a resolution of 2 cm^{-1}. Differences in instrument function and the theoretical broadening may cause differences in band shape, particularly in the strong band. However, the integrated band absorption at a given value of *NL* is unaffected by resolution and can be compared.

The strong band shows good correspondence between measured and simulated integrated band absorption over the range 2200–2450 cm^{-1}, although in the simulation the absorption is slightly distributed towards the band tails. The measured integrated band absorption is 65.3 cm^{-1} which is 0.8% below the simulated result. For the weaker and less saturated band integrated over the range 3525–3775 cm^{-1}, the integrated band absorption is measured to 9.09 cm^{-1} which is 2.6% above the simulated band absorption. The estimated measurement uncertainty is dominated by the uncertainty of the premixed gas which is certified to $\pm 2\%$ of target concentration. Adding the uncertainties of the temperature and pressure measurement, pathlength, as well as base line stability (no baseline correction was made to the presented data), a total uncertainty of 2.5% for the 3525–3775 range is estimated. With the database itself also being subject to uncertainties, this deviation is considered acceptable. Nevertheless, attempts of reducing the deviation were undertaken, including careful verification of the accuracy of the pressure and temperature measurement, whilst a simplified model version of the gas cell was built to verify the pathlength. The investigations did not change the measured band absorption value or the accuracy estimate. Instead, it is noted that the deviation is not uniformly distributed over the absorption band. The integrated absorption over the CO_2 sub-branch at 3655–3775 cm^{-1} deviates from simulations by 3.4% with a peak deviation as high as 4.8% whilst for the sub-branch at 3525–3655 cm^{-1}, the discrepancy is just 1.4% between measurement and simulations. It is further noted that the maximum deviation is coinciding with the double frequency of the sapphire cutoff position. It thus appears that our measurements uncertainty at this position is affected by a double modulation in the interferometer. In principle, the sapphire edge should not be visible after subtracting the background radiation spectrum. However, if there is a temperature difference of the sapphire windows between the background measurement and the actual measurement, which could be a result of the source heating up the nearest window, then the sapphire absorption edge shifts in wavelength between the two recorded spectra. No optical filters were inserted to avoid the double modulation because a wide spectral range was desired; however for future work with the cell this will be considered. The error contribution from this measurement artifact diminishes with increasing absorption, as in the case of elevated pressure.

In order to validate the gas cell at elevated temperature and pressure, measurements from two previous works [6,8] were repeated. 26 years ago, in 1989, Hartmann and Perrin presented measurements of the far wing ν_3 band head (above 2400 cm^{-1}) of CO_2 at elevated temperature and pressure utilizing a grating spectrometer with 2 cm^{-1} resolution [6]. Fig. 7 shows the transmission reported in [6] for 100% CO_2 at 627 K and 31.9 bar over a pathlength of 4.4 cm together with the transmission measured with HTPGC filled with 100% CO_2 at 627 K and 31.9 bar. For the purpose of comparison the HTPGC measurement has been converted to a path length of 4.40 cm by raising the measured transmission to the power of (4.40/3.03). This is valid since the spectral line broadening is well resolved by the spectrometer, and the measured transmission is described by Eq. (2).

The agreement with the far wing ν_3 band head is impressive, and this band edge is the specific focus of Hartmann and Perrin. The other band edge shows a less perfect match, which is possibly related to the temperature dependence of the cut-off edge of sapphire windows employed both in HTPGC as well as in [6], which deteriorates the baseline performance below 2200 cm^{-1}.

Recent work on high temperature and pressure CO_2 absorption by Stefani et al. [8] was attributed to the study of the atmosphere of Venus. In their work, four weak absorption bands of CO_2 were studied, two of which lie outside the sensitivity range of our detector, whilst two are in the vicinity of our measurement region (2000–5200 cm^{-1}). We have repeated their measurement of 100% CO_2 at 19.3 bar and 566 K and the resulting absorption coefficients $k = -\ln(\tau)/L = \sigma_\lambda N$, are compared in Figs. 8 and 9. Also shown is a Voigt-based simulated transmission spectrum using the HITRAN2012 database.

In accordance with Stefani et al., we measure significantly stronger band absorption compared to the simulated spectrum. However, the absorption measured with the HTPGC is significantly weaker than measured by Stefani et al. The estimated uncertainty of the HTPGC measurements is 2.0% at the peak values, which is dominated by the pressure measurement uncertainty as well as the baseline drift which is affected by the spectral location near the edges of our measurement range. In comparison, the difference to the simulated peak values is around 10% for both bands. The large deviation from [8] can possibly

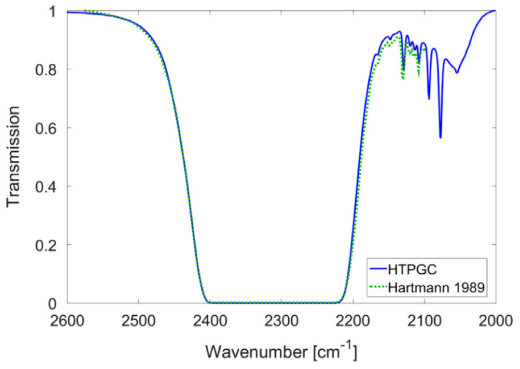

Fig. 7. Transmission of 100% CO_2 at 31.9 bar, 627 K, and $L = 4.40$ cm measured by Hartmann and Perrin and with HTPGC. The HTPGC transmission has been raised to the power of 4.40/3.03 to account for the pathlength difference.

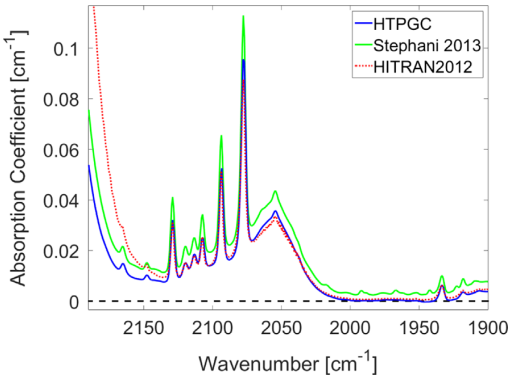

Fig. 8. Absorption coefficient for 100% CO_2 in N_2 at 19.3 bar and 566 K reported by Stefani et al. and measured with HTPGC. A simulated spectrum based on the HITRAN2012 database and Voigt line shapes is also shown.

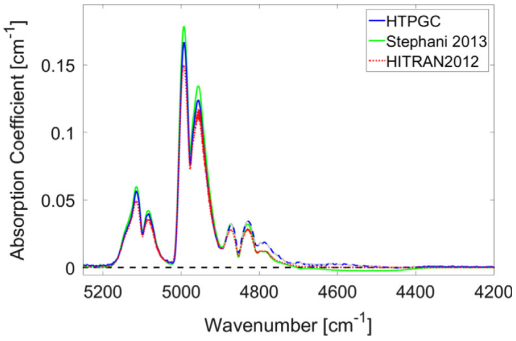

Fig. 9. Absorption coefficient for 100% CO_2 in N_2 at 19.3 bar and 566 K reported by Stefani et al. and measured with HTPGC. A simulated spectrum is shown based on the HITRAN2012 database and Voigt line shapes. The stippled part of the blue line indicates that the HTPGC measurement is affected by the appearance of the first harmonics of the strong ν_3-band. (For interpretation of the references to color in this figure, the reader is referred to the web version of this article.)

be ascribed to a baseline drift in their transmission measurements.

7. Results

The gas cell was filled with 5% CO_2 in nitrogen to a pressure of 101 bar at 1000 K. The resulting absorption coefficient is shown in Fig. 10 and 11. Under this high pressure the ν_3 band in Fig. 10 is strongly saturated, but the tail is very important for accurate modeling of the gas emissivity and radiative transfer in combustion processes. The red curve shows a simulation based on HITEMP2010 [12] and Voigt line shapes. The result is a significant deviation from the measurement with an overestimation of the integrated band absorption of 20% at 101 bar, 1000 K, and $L=3.03$ cm. The measured integrated band absorption is 226 cm^{-1} evaluated in the range 2050–2550 cm^{-1}.

The weaker combination band around 3700 cm^{-1} is not saturated although strongly absorbing, and thus it is possible to extract the absorption coefficient for the complete band, see Fig. 11.

For this band a similar tendency is observed; the measurement reveals slightly sharper features than the Voigt simulation which overestimates the band tail. However, in this case the simulated integrated band absorption is in agreement within 2.5% of the measurement, because the overestimation of the tail is counterbalanced by the weaker peak absorption. The measured integrated band absorption is 201 cm^{-1} in the range 3300–3800 cm^{-1} with an uncertainty estimated to 3.0%.

Although extensively used, the Voigt line shape is well known to be inadequate to model CO_2 absorption at elevated pressures and empirical corrections have been implemented [13–17] up to 60 bar. However, the integrated band comparison with the Voigt simulation is interesting as it may be sufficiently accurate for purpose of modeling radiative transfer, or at least give an impression

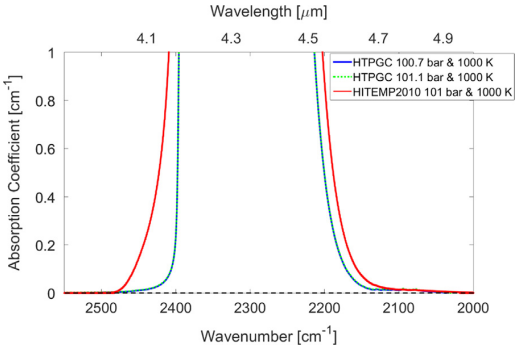

Fig. 10. Measurement with HTPGC of 5% CO_2 in nitrogen at 101 bar and 1000 K. Shown together with a simulation based on HITEMP2010 and the Voigt formalism. (For interpretation of the references to color in this figure legend, the reader is referred to the web version of this article.)

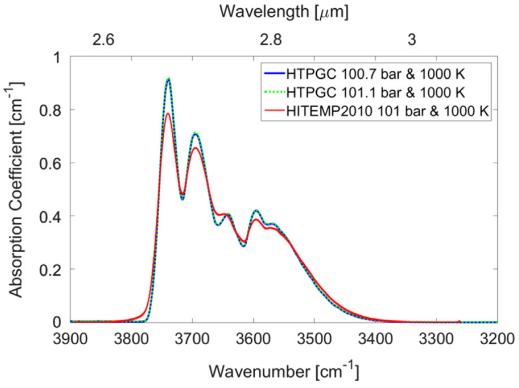

Fig. 11. Measurement with HTPGC of 5% CO_2 in nitrogen at 101 bar and 1000 K. Shown together with a simulation based on HITEMP2010 and the Voigt formalism. The instrument resolution was 2 cm^{-1}.

of the consequences of employing the simple Voigt formalism in such modeling.

In contrast to the comparison of integrated band absorption, the derived absorption coefficient is in less quantitative correspondence with the simulation with the three larger peaks between 13% and 18% stronger in the measurement compared to simulation. As discussed in Section 6, this band is affected by a measurement artifact which is estimated to be able to account for up to 5% of the strongest peak. The background radiation in the measurement contributed with about half the measured intensity around 2300 cm^{-1} in the absence of CO_2 and about 10% of the intensity at 3700 cm^{-1}.

The present work provides spectral data that can be used for experimental verification of these models beyond previously reported temperature and pressure combinations.

8. Discussion

In this paper a peak deviation of up to 5% was assigned to a measurement artifact related to a double modulation signal appearing around 3750 cm^{-1}. The feature appears to be replicating the raw spectrum at the double frequency; however, attempts of determining and correcting for the contribution of this artifact were unsuccessful. Instead, the measurement result was given without correction but with an estimate of the additional uncertainty around this wavelength. Obtaining more accurate results at this wavelength might require the use of a different window material but this must be weighed against the advantages of sapphire. The 1000 K measurement, which is found in supplementary materials, reveals small levels of methane inside the cell. This is attributed to the glue and increases with the time the gas spends in the cell. Therefore the setup is being reworked to reduce this time prior to measurements at higher temperatures.

9. Conclusion

A high temperature and pressure gas cell for quantitative spectroscopic measurements designed for higher temperature and pressure combinations than previously reported has been realized and presented. Measurements have been compared with simulations based on HITEMP2010 using the Voigt line shape. A significant deviation from the measurement with an overestimation of the integrated ν_3-band absorption of 20% at 101 bar and 1000 K, whereas only a minor deviation of 2.5% is seen for the weaker CO_2 band located around 3700 cm^{-1}. Thus, a simple HITEMP2010 simulation might be used as a tool to estimate gas absorption at engine conditions if errors are acceptable. In future work the gas cell will be utilized for systematic investigations of the absorption of CO_2 and H_2O at temperatures up to 1273 K and 200 bar pressure.

Acknowledgment

The present work was funded by the project RADIADE under contract no. 10-093974 financed by The Danish Council for Strategic Research. Thomine is an industrial PhD student at Danfoss IXA A/S and her work is supported by the Danish Agency of Science, Technology and Innovation (DASTI) (Project number 11-117567).

References

[1] Baines Kevin H, Atreya Sushil, Carlson Robert W, Crisp David, Drossart Pierre, Formisano Vittorio, Limaye Sanjay S, Markiewicz Wojciech J, Piccioni Giuseppe. To the depths of Venus: exploring the deep atmosphere and surface of our sister world with Venus Express. Planet Space Sci 2006;54:1263–78.
[2] Rivière Philippe, Soufiani Anouar. Updated band model parameters for H_2O, CO_2, CH_4 and CO radiation at high temperature. Int J Heat Mass Transf 2012;55:3349–58.
[3] Schramm J. Technical University of Denmark, ⟨http://www.radiade.mek.dtu.dk/⟩; 2014 [Accessed April 2015].
[4] Skeen Scott, Manin Julien, Pickett Lyle, Dalen Kristine, Ivarsson Anders. Quantitative spatially resolved measurements of total radiation in high-pressure spray flames, SAE International; 2014.
[5] Rothman LS, Gordon IE, Babikov Y, Barbe A, Chris Benner D, Bernath PF, et al. The HITRAN 2012 molecular spectroscopic database. J Quant Spectrosc Radiat Transf 2013;130:4–50.
[6] Perrin Marie-Yvonne, Hartmann Jean-Michel. Measurements of pure CO_2 absorption beyond the v_3 bandhead at high temperature. Appl Opt 1989;28(13):2550–3.
[7] Farroq A, Jeffries JB, Hanson RK. Measurements of CO_2 concentration and temperature at high pressures using 1f-normalised wavelength modulation spectroscopy with second order harmonic detection near 2.7 um. Appl Opt. 2009;48(35):6740–53.
[8] Stefani Stefania, Piccioni Guiseppe, Snels Marcel, Grassi Davide. Experimental CO_2 absorption coefficients at high pressure and high temperature. J Quant Spectrosc Radiat Transf 2013;117:21–8.
[9] SpectralCalc.com High-resolution spectral modeling, GATS, Inc, Available at: ⟨http://www.spectralcalc.com/info/about.php⟩; 2015 [Accessed 07.05.15].
[10] Gordley Larry L, Marshall Benjamin T, Chu D Allen. LINEPAK: algorithms for modeling spectral transmittance and radiance. J Quant Spectrosc Radiat Transf 1994;52(5):563–80.
[11] Mellqvist Johan, Rosén Arne. DOAS for flue gas monitoring-II. Deviations from the Beer–Lambert law for the U.V./visible absorption spectra of NO, NO, SO_2 and NH_3. J Quant Spectrosc Radiat Transf 1996;56:209–24.
[12] Rothman LS, Gordon IE, Barber RJ, Dothe H, Gamache RR, Goldman A, et al. HITEMP, the high-temperature molecular spectroscopic database. J Quant Spectrosc Radiat Transf 2010;111:2139–50.
[13] Filippov Nikolai N, Asfin RE, Sinyakova TN, Grigoriev IM, Petrova TM, Solodov AM, et al. Experimental and theoretical studies of CO_2 spectra for planetary atmosphere modelling: region 600–9650 cm^{-1} and pressures up to 60 atm. Phys Chem Chem Phys 2013;15:13826.
[14] Perrin MY, Hartmann JM. Temperature-dependent measuremnets and modeling of absorption by CO_2–N_2 mixtures in the far line-wings of the 4.3 μm CO_2 band. J Quant Spectrosc Radiat Transf 1989;42:311–7.
[15] Tran H, Boulet C, Stefani S, Snels M, Piccioni G. Modeling of high pressure pure CO_2 spectra from 750 to 8500 cm^{-1}. I-central and wing regions of the allowed vibrational bands. J Quant Spectrosc Radiat Transf 2011;112:925–36.
[16] Alberti Michael, Weber Roman, Mancini Marco. Re-creating Hottel's emissivity charts for carbon dioxide and extending them to 40 bar pressure using HITEMP-2010 data base. Combust Flame 2014;162:597–612.
[17] Lamouroux J, Régalia L, Thomas X, Vander Auwera J, Gamache RR, Hartmann J-M. CO_2 line-mixing database and software update and its tests in the 2.1 μm and 4.3 μm regions. J Quant Spectrosc Radiat Transf 2015;151:89–96.

List of Acronyms

ECA Emission Control Areas

EGR exhaust gas recirculation

FTIR Fourier transform infrared

FWHM full width at half maximum

HC hydrocarbon

HTF Danish high technology foundation

IML Infrared Multilayer Laboratory

IMO International Maritime Organisation

NBP narrow bandpass

NDIR non-dispersive infrared

SCR selective catalytic reduction

VMR volume mixing ratio

WBP wide bandpass

Bibliography

[1] Thomine Stolberg-Rohr et al. In optics humidity compensation in NDIR exhaust gas measurements of NO_2. *Proceedings of Advanced Photonics Congress, Sensors*, 2015.

[2] Thomine Stolberg-Rohr and Gary J. Hawkins. Spectral design of temperature-invariant narrow bandpass filters for the mid-infrared. *Optics Express*, 23(1):580–596, 2015.

[3] Daniel Poitras. Spotlight on optics. https://www.osapublishing.org/spotlight/summary.cfm?id=307633, March 2015.

[4] Gary J. Hawkins and Thomine Stolberg-Rohr. Determination of the embedded thermo-optical expansion coefficients of PbTe and ZnSe thin film infrared multilayers. *Optics Express*, 23(12):16348–16355, 2015.

[5] Kåre Press-Kristensen and Christian Ege. *Renere skibsfart*. Det Økologiske Råd, 1st ed. edition, 2011.

[6] Jørgen Brandt et al. Assessment of health-cost externalities of air pollution at the national level using the EVA model system. Technical report, Aarhus University, National Environmental Research Institute, Department of Atmospheric Environment, March 2011.

[7] Maritime Cyprus International News Blog. 10 reasons why ship operators should be nervous about the 2015 ECA regulations. In *Maritime Regulations and Conventions*, November 19 2014.

[8] International Maritime Organization. Pollution prevention. http://www.imo.org/en/OurWork/Environment/PollutionPrevention/Pages/Default.aspx, 2015.

[9] International Maritime Organization. *Revised MARPOL Annex VI*. Resolution mepc.176(58) edition, 2008.

[10] C. S. Brookman. Exhaust gas monitoring. *IMAS 96 - Shipping and the environment: is compromise inevitable? PT I*, 108(5):31–36, 1996.

[11] S. Brynolf, M. Magnusson, E. Fridell, and K. Andersson. Compliance possibilities for the future ECA regulations through the use of abatement technologies or change of fuels. *Transportation Research Part D: Transport and Environment*, 28:6 – 18, 2014.

[12] W. Addy Majewsky and Magdi K. Khair. *Diesel Emissions and Their Control*. SAE International, 2006.

[13] Kati Lehtoranta, Hannu Vesala, Paivi Koponen, and Satu Korhonen. Selective catalytic reduction operation with heavy fuel oil: NOx NH_3, and particle emissions. *Environmental Science and Technology*, 49(7):4735–4741, 2015.

[14] Jakob Mahler Hansen. *Exhaust gas recirculation control for diesel engines*. PhD thesis, 2013.

[15] Gwang-jung Kim, Byungchul Choi, and Inchul Choi. Real-time co_2 sensor for the optimal control of electronic EGR system. volume 9044, pages 90440C–90440C–7, 2013.

[16] Jussi Lyyränen, Jorma Jokiniemi, Esko I. Kauppinen, and Jorma Joutsensaari. Aerosol characterisation in medium-speed diesel engines operating with heavy fuel oils. *Journal of Aerosol Science*, 30(6):771 – 784, 1999.

[17] HFO Handbook. Notes on heavy fuel oil. *American Bureau of Shipping, ABS, publication*, 31, 1984.

[18] Germanisher Lloyd SE, editor. *Rules for Clasification and Construction*, chapter VI Additional Rules and Guidelines. Germanisher Lloyd SE, Hamburg, 2012.

[19] MAN B&W Diesel A/S. Emission control MAN B&W two-stroke diesel engines. Copenhagen, Denmark, 2004.

[20] MAN B&W Diesel A/S. L32/40 project guide - marine four-stroke genset compliant with imo tier ii, November 2013.

[21] International Maritime Organization. *NO_textX technical code 2008*. Resolution mepc.177(58) edition, 2008.

[22] J. O. W. Norris. Appendix 1 Technologies available for measuring NOx. In *An In-Service Emissions Test for Spark Ignition (SI) Petrol Engines*. EMStec Ltd, December 2002.

[23] Bo Svensson. Direct emissions measurement. *Diesel & Gas Turbine Worldwide*, November 2014.

[24] John E. Orban et al. Long-term aging of NOx sensors in heavy-duty engine exhaust. *Sae Technical Papers, Sae Techni. Paper*, 2005.

[25] M. Ioannou, G. Papalambrou, N. P. Kyrtatos, H. Dumele, and M. Diessner. Evaluation of emission sensors for four-stroke marine diesel engines. *Journal of marine engineering and technology*, 12(3):20–29, 2013.

[26] J.-Y. Zhang and I. W. Boyd. Lifetime investigation of excimer uv sources. *Applied Surface Science*, 168(1-4):296–299, 2000.

[27] Jacob Y. Wong and Roy L. Anderson. *Non-dispersive Infrared Gas Measurement*. International Frequency Sensor Associaton Publishing, 2012.

[28] Ross Stanley. Plasmonics in the mid-infrared. *Nature Photonics*, 6(7):409–411, 2012.

[29] T. Wijaya, T. Tjahjowidodo, and P Thepsithar. Real time ship exhaust gas monitoring for compliance to SO_x and NO_x regulation and CO_2 footprint. *Sun Above the Horizon: Meteoric Rise of the Solar Industry*, 5:201, 2014.

[30] A. J. de Castro, J. Meneses, S. Briz, and F. López. Nondispersive infrared monitoring of NO emissions in exhaust gases of vehicles. *Review of Scientific Instruments*, 70(7):3156–3159, 1999.

[31] Louise Helen Crawley. Application of non-dispersive infrared (NDIR) spectroscopy to the measurement of atmospheric trace gases. Master's thesis, University of Canterbury, Christchurch, New Zealand, 2008.

[32] You-Wen et al. Sun. Water vapor interference correction in a non dispersive infrared multi-gas analyzer. *Chinese Physics Letters*, 28(7):073302, 2011.

[33] You-Wen et al. Sun. Cross-interference correction and simultaneous multi-gas analysis based on infrared absorption. *Chinese physics B*, 21(9), 2012.

[34] M. Diem. *Introduction to Modern Vibrational Spectroscopy*. Wiley, 1993.

[35] GATS. Spectral calculator. http://www.spectralcalc.com.

[36] A. D. H. Clague, J. B. Donnet, T. K. Wang, and J. C. M. Peng. A comparison of diesel engine soot with carbon black. *Carbon*, 37(10):1553–1565, 1999.

[37] Y. Kimura, T. Sato, and C. Kaito. Production and structural characterization of carbon soot with narrow UV absorption feature. *Carbon*, 42(1):33–38, 2004.

[38] JanaMoldanova et al. Characterisation of particulate matter and gaseous emissions from a large ship diesel engine. *Atmospheric Environment*, 43(16):2632–2641, 2009.

[39] René Bergmann, Aliaksandra Ivinskaya, J Kafka, Fridolin Okkels, and Mogens H Jakobsen. From modeling to fabrication of double side microstructured silicon windows for infrared gas sensing in harsh environments. In *Advanced Electromagnetic Materials in Microwaves and Optics (Metamaterials)*, pages 58–60. IEEE, 2014.

[40] Chandler Downs and Thomas E. Vandervelde. Progress in infrared photodetectors since 2000. *Sensors*, 13(4):5054–5098, 2013.

[41] Koichiro Ueno, Edson Gomes Camargo, Takashi Katsumata, Hiromasa Goto, Naohiro Kuze, Yoshihiro Kangawa, and Koichi Kakimoto. InSb mid-infrared photon detector for room-temperature operation. *Japanese Journal of Applied Physics*, 52(9), 2013.

[42] L.S. Rothman et al. The HITRAN 2008 molecular spectroscopic database. *Journal of Quantitative Spectroscopy and Radiative Transfer*, 110:533–572, 2009.

[43] Johan Sjoholm et al. Simultaneous visualization of OH, CH, CH_2O and toluene PLIF in a methane jet flame with varying degrees of turbulence. *Proceedings of The Combustion Institute*, 34(1):1475–1482, 2013.

[44] Fred G. Rounds Martin A. Elliott, Gerge J. Nebel. The composition of exhaust gases from diesel, gasoline and propane powered motor coaches. *Journal of the Air Pollution Control Association*, 5(2):103–108, 1955.

[45] Frank L. Pedrotti, Leno Matthew. Pedrotti, and Leno S. Pedrotti. *Introduction to optics*. Pearson Prentice Hall, 2007.

[46] H. A. Macleod. *Thin-film optical filters*. CRC Press, 2010.

[47] G. J. Hawkins. *Spectral characterisation of infrared optical materials and filters*. PhD thesis, The University of Reading, 1998. #R7935.

[48] O. S. Heavens. Optical properties of thin films. *Reports on progress in physics*, 23:2–65, 1960.

[49] Jeppe Seidelin Dam, Peter Tidemand-Lichtenberg, and Christian Pedersen. Room temperature mid-ir single photon spectral imaging. *Nature Photonics*, 6:788–793, 2012.

[50] Antoni. Rogalski. *Infrared detectors*. CRC Press, 2011.

[51] A. Rogalski. Novel uncooled infrared detectors. *Opto-Electronics Review*, 18(4):478–492, 2010.

[52] C. S. Evans, R. Hunneman, J. S. Seeley, and A. Whatley. Filters for $\nu 2$ band of CO_2: monitoring and control of layer deposition [atmospheric temperature sounding applications]. *Applied Optics*, 15(11):2736–2745, 1976.

[53] B. Li, S. Y. Zhang, J. C. Jiang, D. Q. Liu, and F. S. Zhang. Recent progress in improving low-temperature stability of infrared thin-film interference filters. *Optics Express*, 13(17):6376–6380, 2005.

[54] L. S. Rothman et al. Hitemp, the high-temperature molecular spectroscopic database. *Journal of Quantitative Spectroscopy and Radiative Transfer*, 111(15):2139–2150, 2010.

[55] Det Strategiske Forskningsråd. RADIADE - Modellering og verificering af stråling i marine dieselmotorer. http://www.strategiskforskning.dk/projects/radiade-modellering-og-verificering-af-straaling-i-marine-dieselmotorer, 2011-2015.

Department of Chemical and Biochemical Engineering
Technical University of Denmark
Building 229
DK – 2800 Kgs. Lyngby
Denmark

Phone: +45 4525 2800
Web: www.chec.kt.dtu.dk